From defectant theory to nanoscale transformations in steels

M. Herbig, J. Millan, D. Ponge, S. Sandlöbes, S. Goto, Y. Li, P. Choi, S. Zaefferer,
A. Nematollahi, R. Kirchheim, C. Borchers, G. Inden, J. Neugebauer, D. Raabe

Max-Planck-Institut für Eisenforschung GmbH
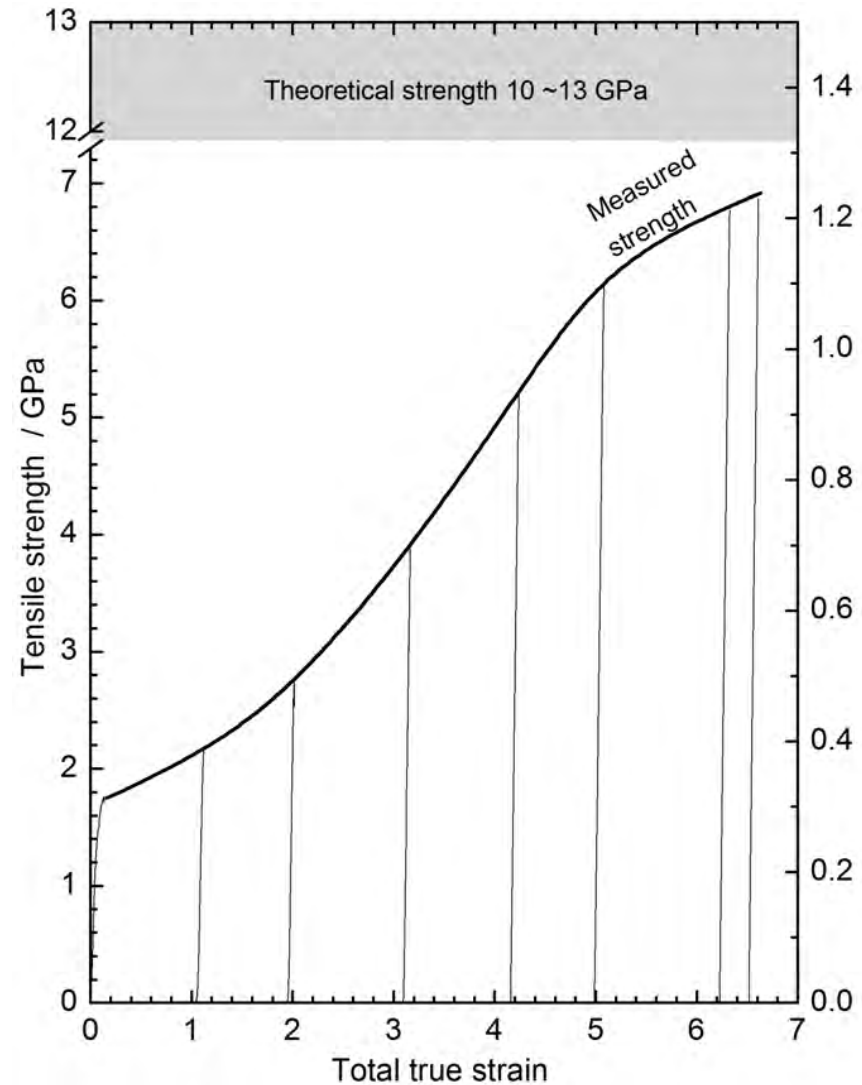
Düsseldorf, Germany
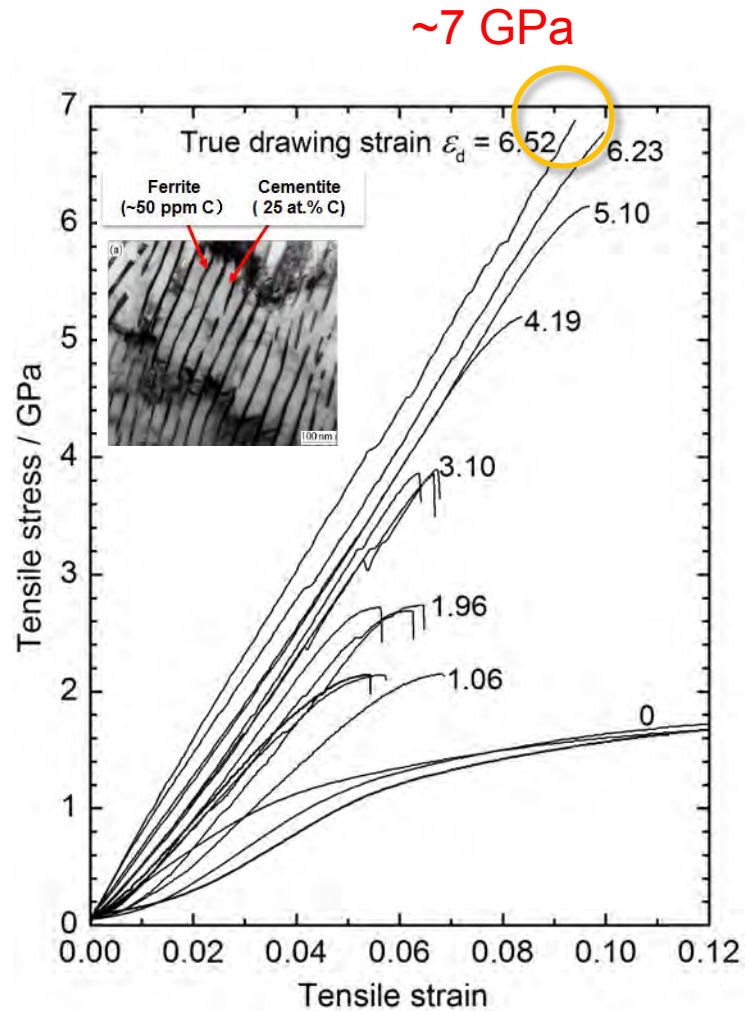
WWW.MPIE.DE
d.raabe@mpie.de

short version

Pearlite: the limits of strength
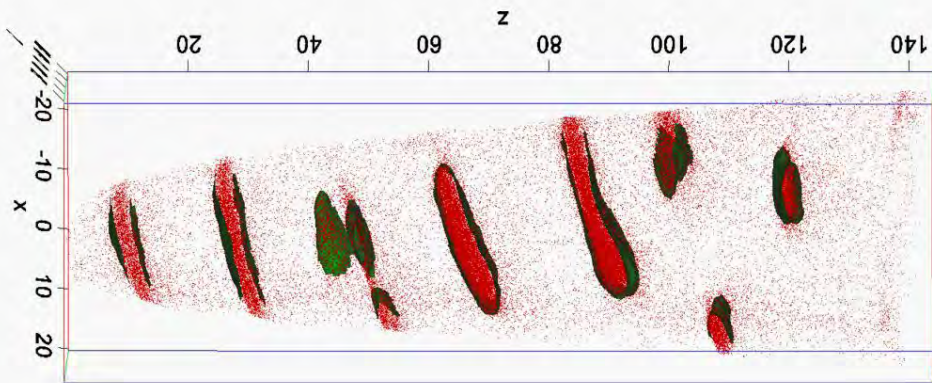
Nano-austenite reversion

~7 GPa

Ferrite
(~50 ppm C）
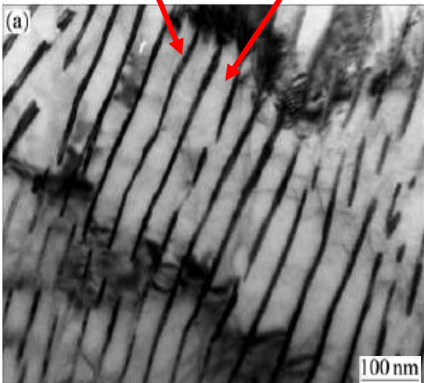
Cementite
(25 at.% C)

$(\varepsilon = 2)$

Scale: nm

R ~ 50 nm
T ~ 20÷100 K

V_{DC}

$(\varepsilon = 6.5)$
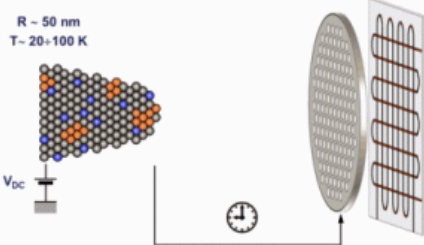
C iso-
concentration
(7 at.%)

• C
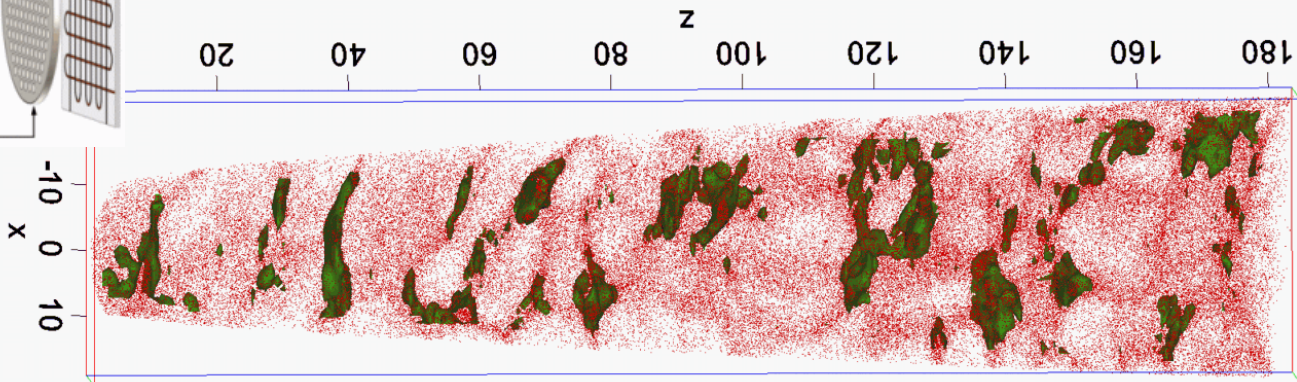
- Why does carbide dissolve?

- Where is the C?

- How stable is C in ferrite?

- What does that mean for the flow stress and strain hardening ?

- • **Why does carbide dissolve?**
- • Where is the C?
- • How stable is C in ferrite?
- • What does that mean for the flow stress and strain hardening ?

Wire axis • v

~ 5 nm

$15 \times 15 \times 50 \times nm^3$

wire axis

• Carbon

$9 \times 9 \times 38 \ nm^3$

$8.8 \times 8.8 \times 8 \ nm^3$

Xavier Sauvage

- Hypereutectoid pearlite (Fe-098C-0.31Mn-0.20Si-0.20Cr (wt%))
- cold-drawn to ε=6.02 true strain, annealed for 2 min at 400ºC, ~ 6 GPa UTS

- Why does carbide dissolve?
- Where is the C?
- How stable is C in ferrite?
- What does that mean for the flow stress and strain hardening ?

100 nm

BF-STEM image of pearlitic atom probe tip, view along axis of columnar grains

- C

→ experiment by Michael Herbig

Grain boundary plane normals analyzed from STEM images

Grain orientations measured by nano beam diffraction
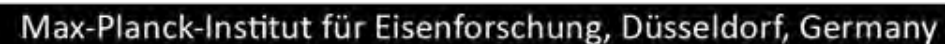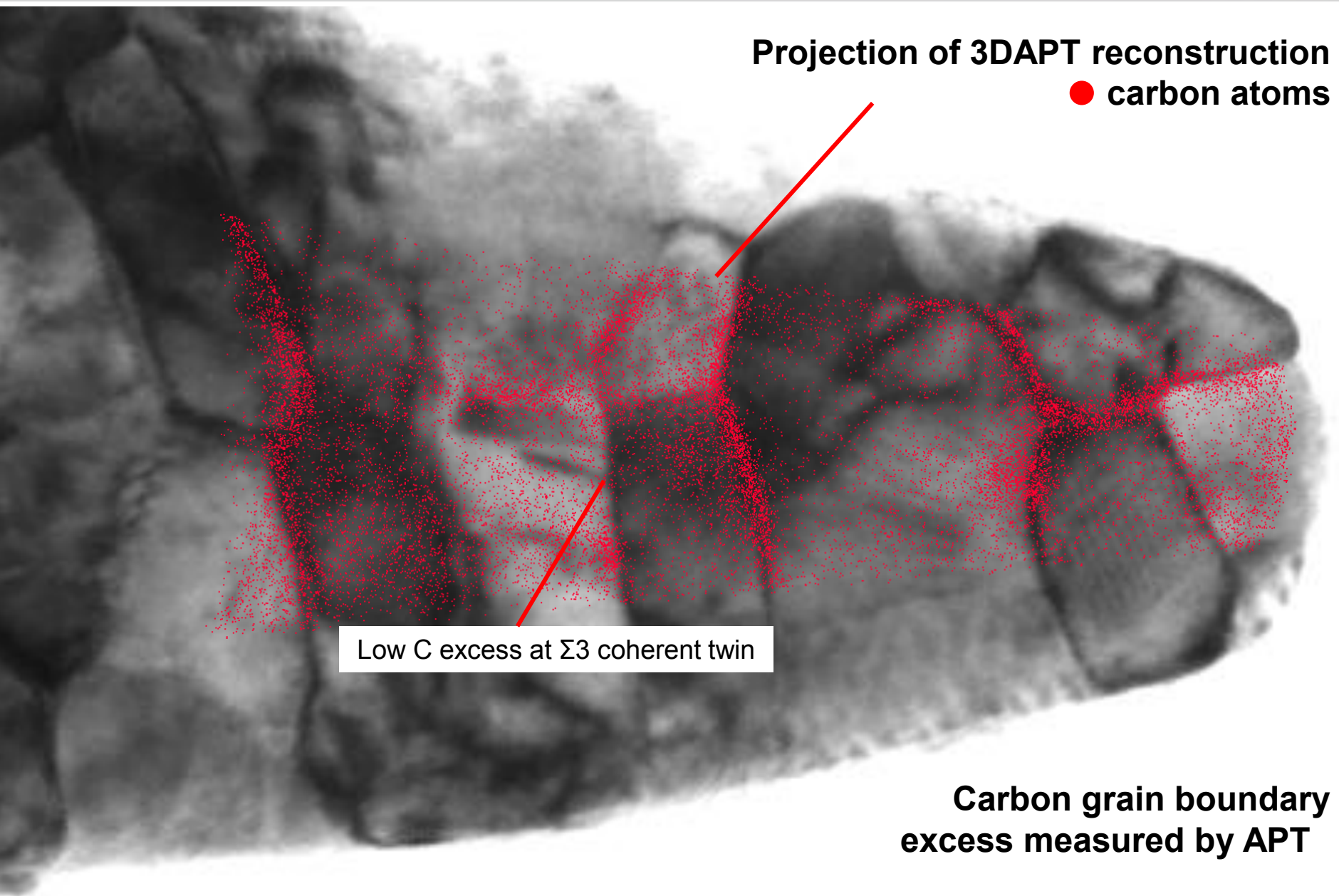
Projection of 3DAPT reconstruction
● carbon atoms

Low C excess at Σ3 coherent twin
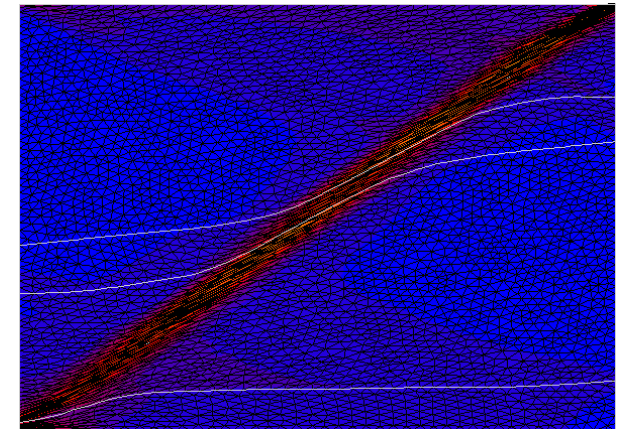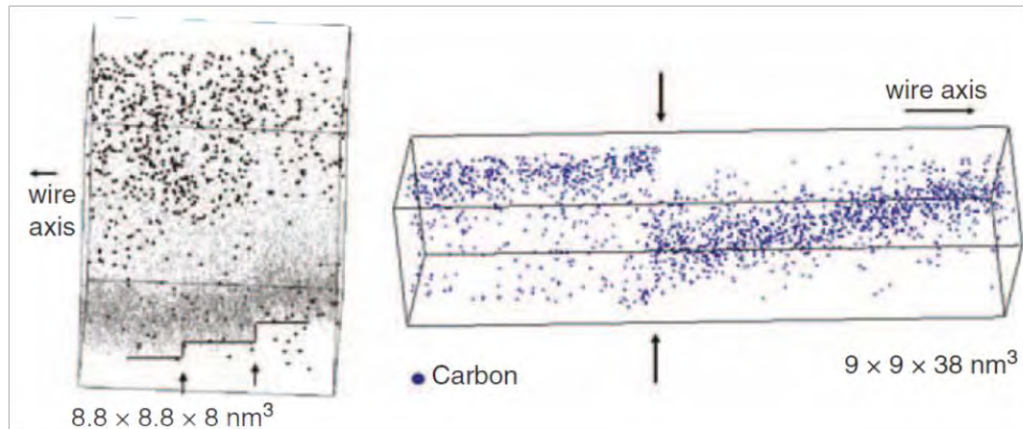
Carbon grain boundary
excess measured by APT

- Why does carbide dissolve?
- Where is the C?
- How stable is C in ferrite?
- What does that mean for the flow stress and strain hardening ?

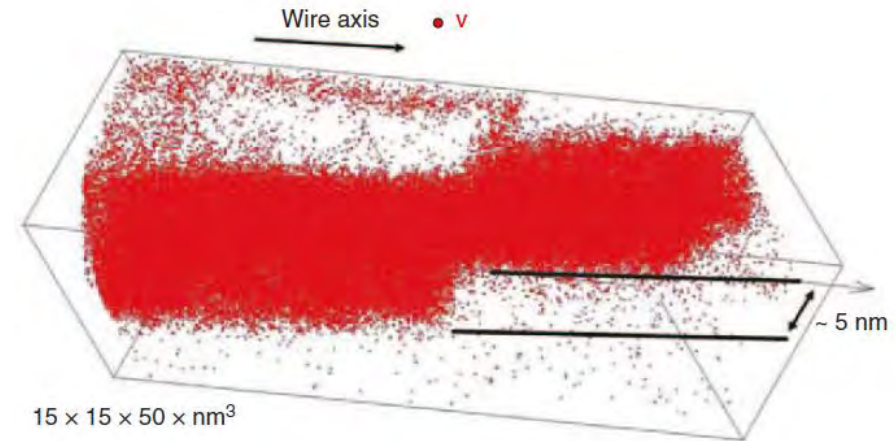C solubility in Fe under stresses

C solubility in Fe under stresses

- Why does carbide dissolve?
- Where is the C?
- How stable is C in ferrite?
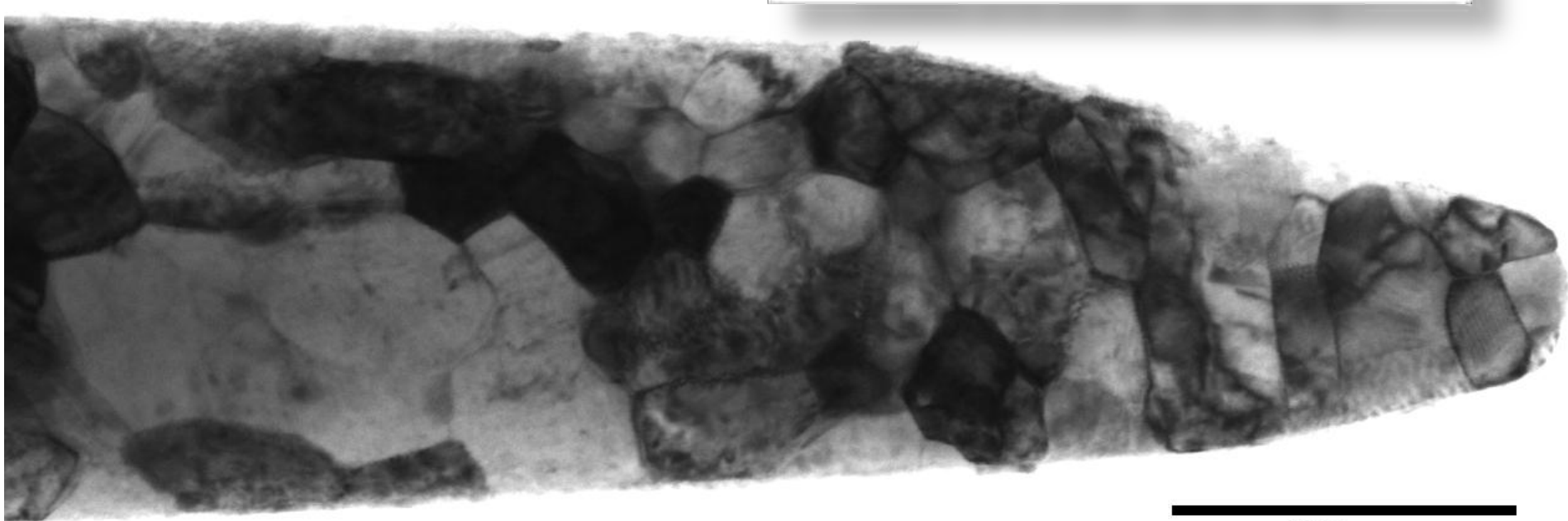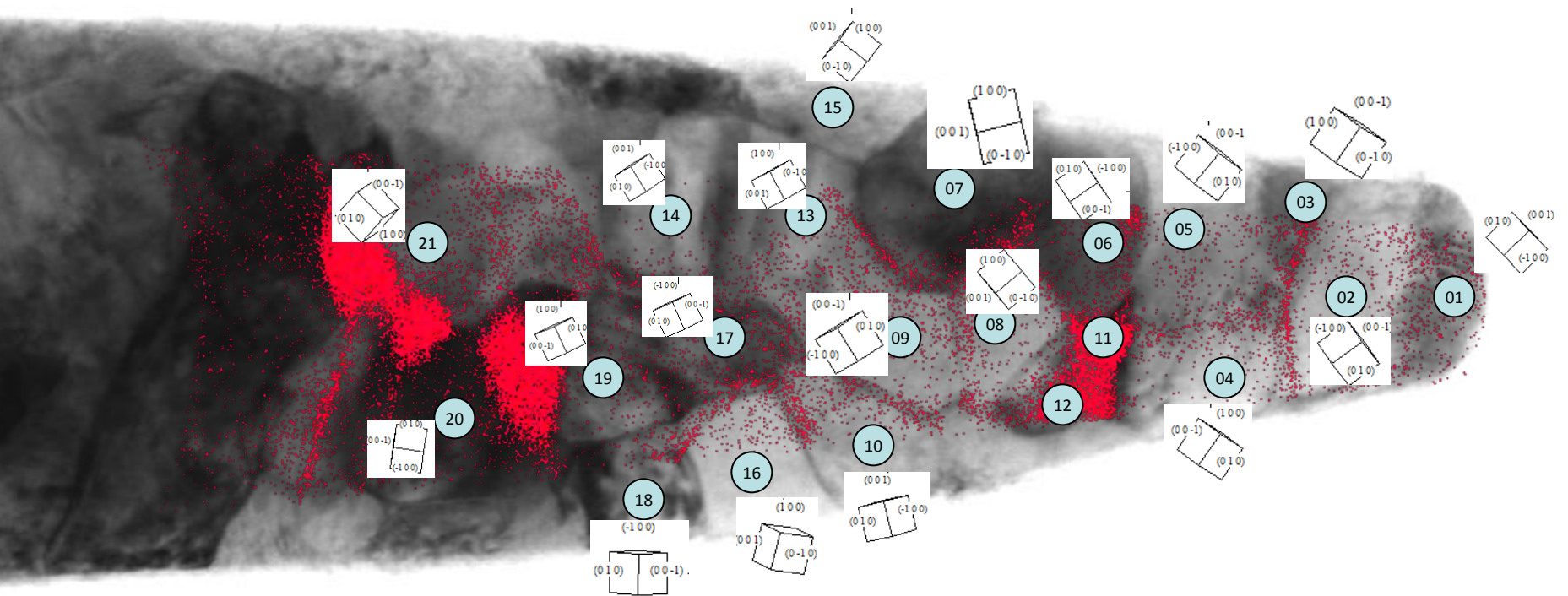- What does that mean for the flow stress and strain hardening ?

Pearlite: the limits of strength

Nano-austenite reversion
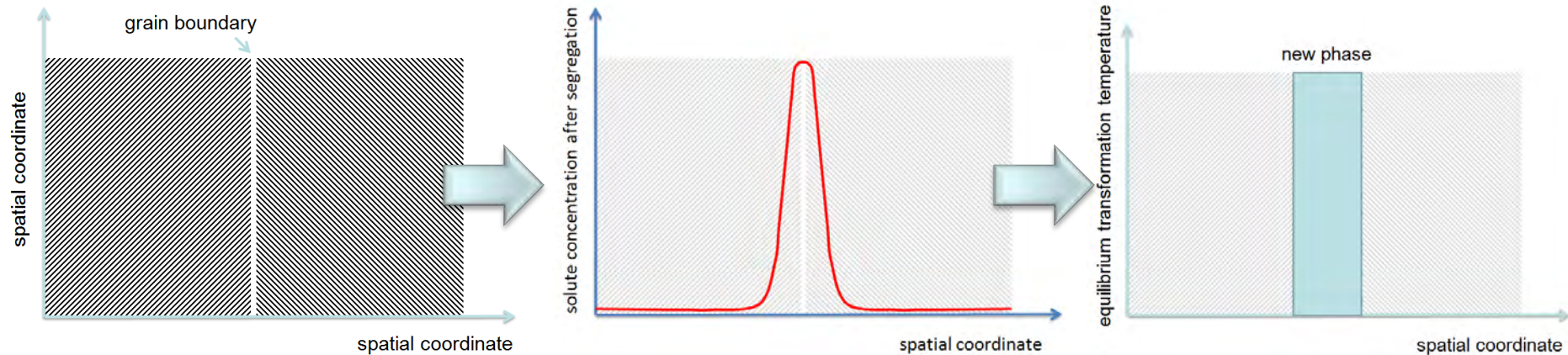
Solute segregation to martensite grain boundaries

Local phase transformation at grain boundary
(martensite-to-austenite reversion confined to GB)

grain boundary — spatial coordinate / spatial coordinate

solute concentration after segregation / spatial coordinate

equilibrium transformation temperature / new phase / spatial coordinate

Solute segregation to martensite grain boundaries

- Element with high segregation tendency
- Reduce transformation temperature (e.g. from martensite to austenite)
- Prefer segregation over bulk precipitation (e.g. carbide)

Local phase transformation at grain boundary (martensite-to-austenite reversion confined to GB)

9Mn-2Ni-0.15Al-1Ti-1Mo (wt.%)

α-Fe
IPF//ND

phase	fraction
α martensite	1.00
γ austenite	0.00
ε martensite	0.00

ND
RD

500 nm

Lath-type martensitic microstructure

Max-Planck-Institut für Eisenforschung, Düsseldorf, Germany

D. Raabe et al. Scripta Materialia 60 (2009) 1141

15

20 nm
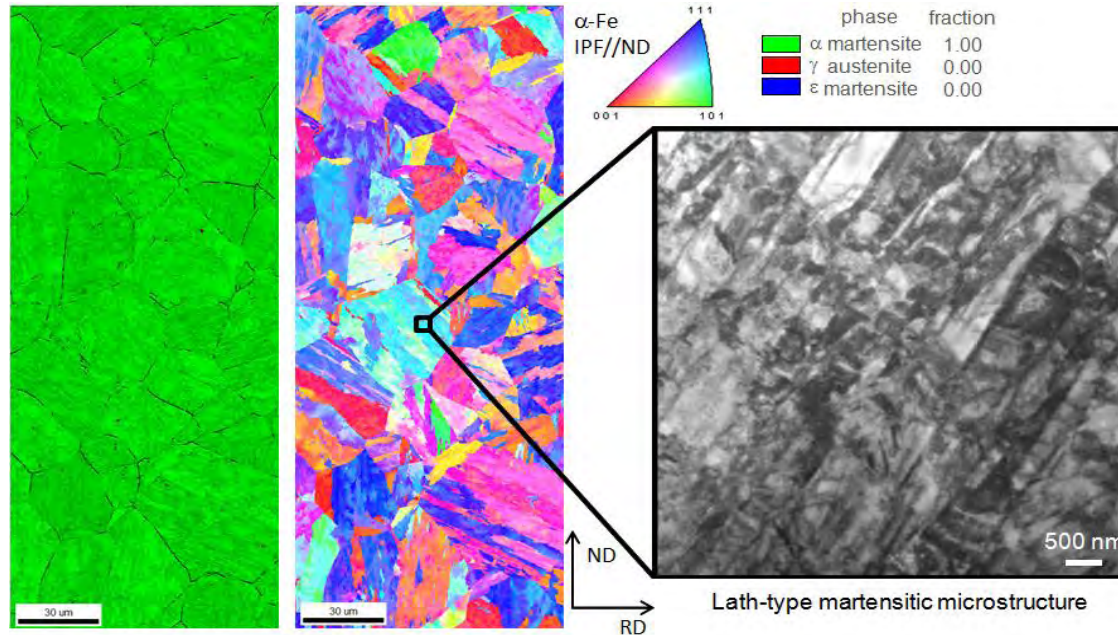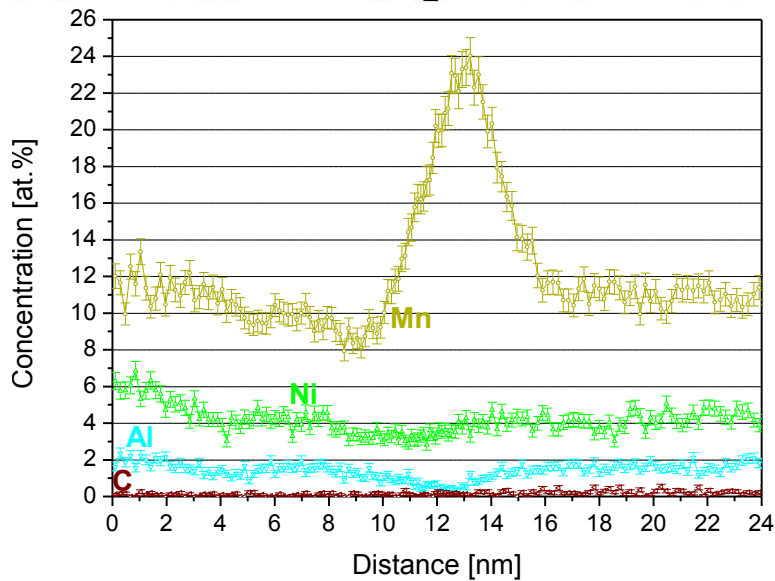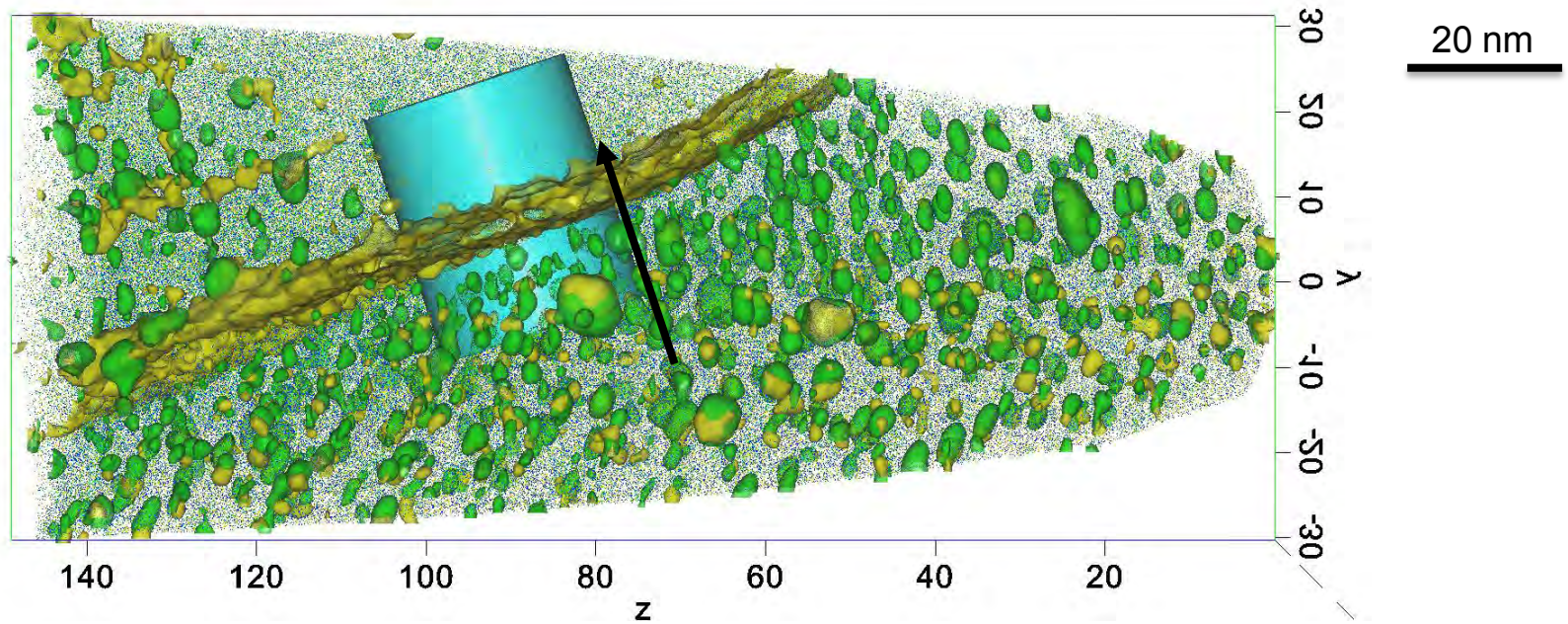
9Mn-2Ni-0.15Al-1Ti-1Mo (wt.%)

9Mn-2Ni-0.15Al-1Ti-1Mo (wt.%)
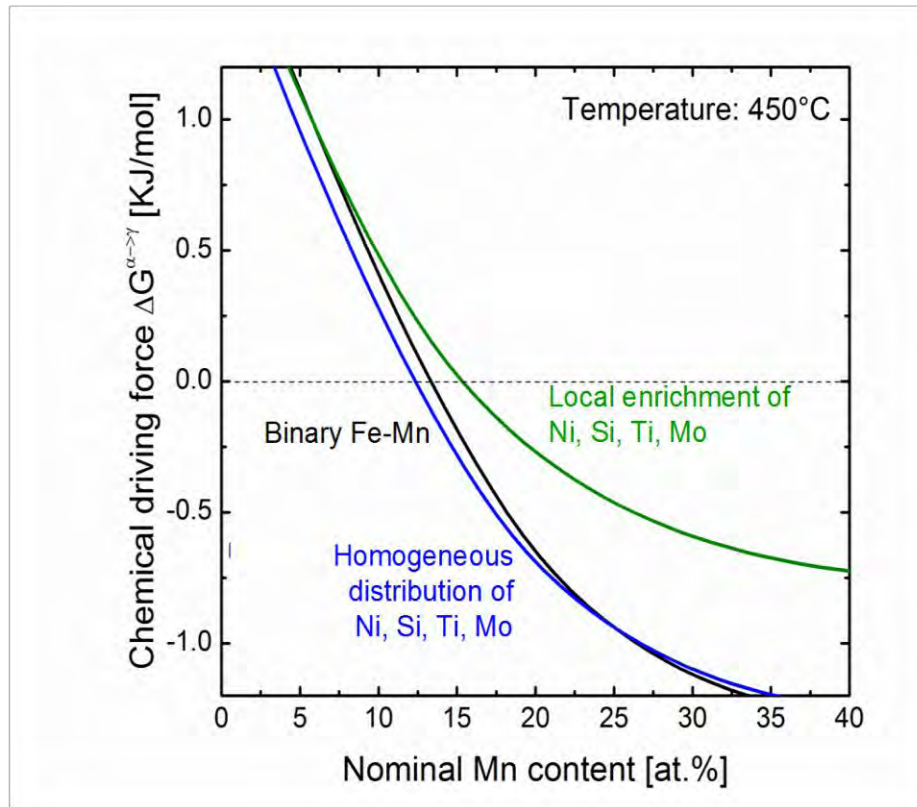
$$\Delta G*(T,x) = \frac{4(b\gamma_{M-A} - a\gamma_{M-M})^3}{27c^2(\Delta g_{chem}(T,x) + \Delta g_{elast})^2}$$

9Mn-2Ni-0.15Al-1Ti-1Mo (wt.%), aged 450°C/65h

20 nm

Iso-conc. **10 at.%Ni** **18 at.%Mn**

Mn **Ni** **Al** **C**

Particle decorated martensite (bcc)

Interface region (fcc)

Mn in austenite
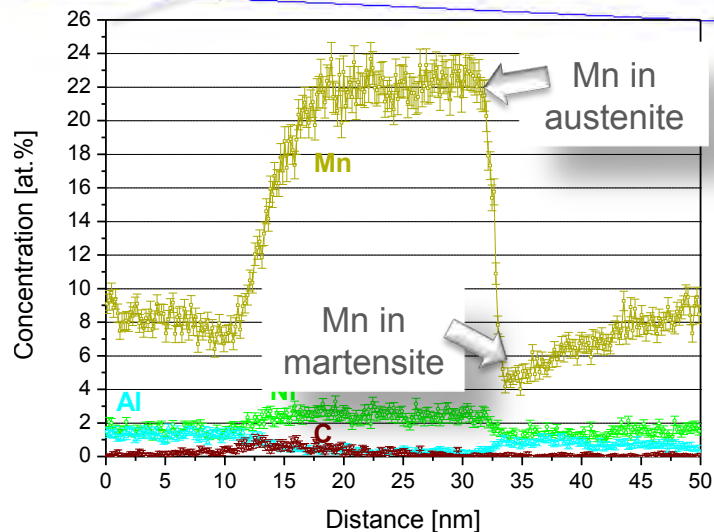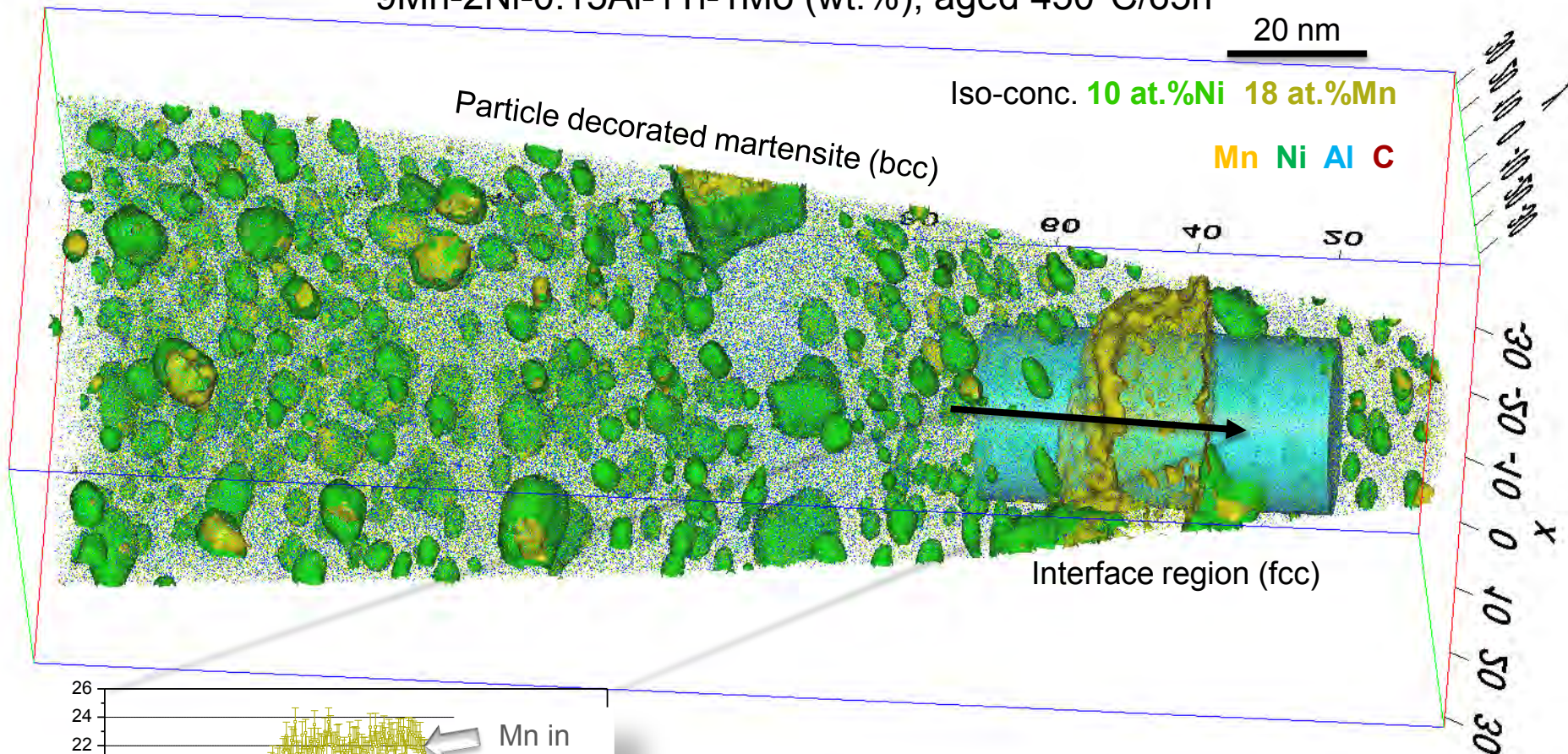
Mn in martensite

Phase formation at martensite interface
Near-equilibrium partitioning at interface
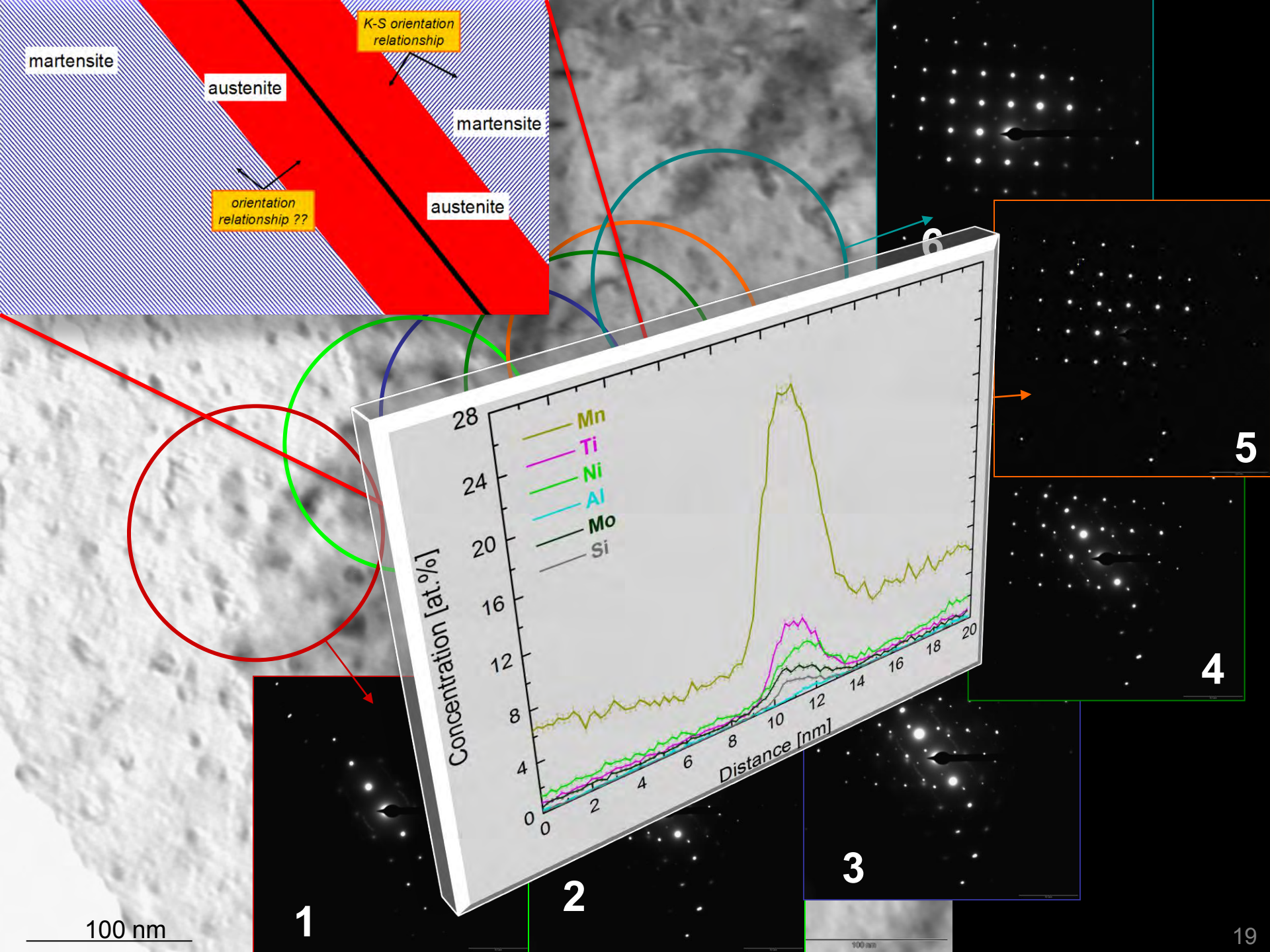
martensite

austenite

K-S orientation relationship

martensite

austenite

orientation relationship ??

Mn
Ti
Ni
Al
Mo
Si

Concentration [at.%]

Distance [nm]

100 nm

1

2

3

4

5

6

19

Ni-Maraging

(X3NiCoMoTi18-12-4)

aged (450°C/48h)

quenched

12MnPH

aged (450°C/48h)

quenched
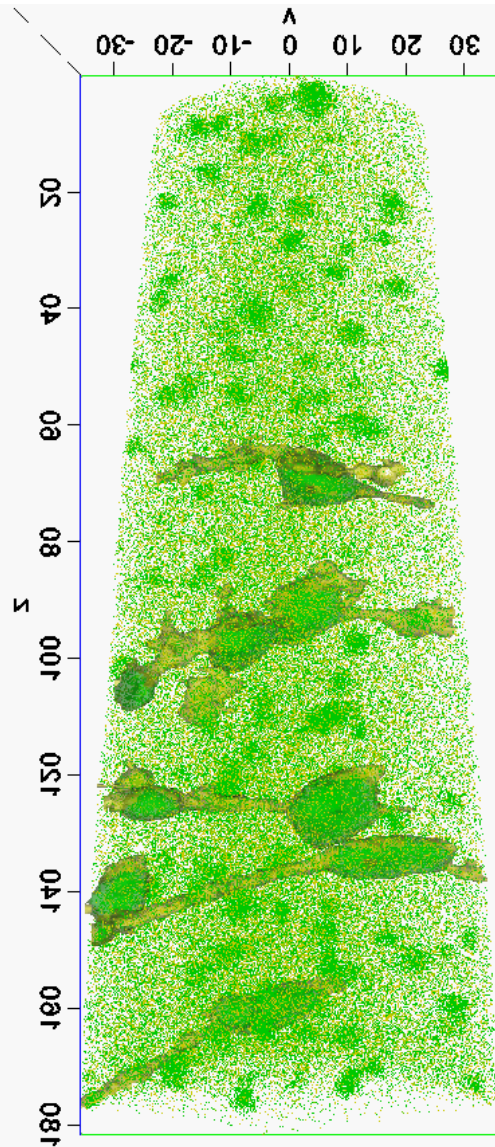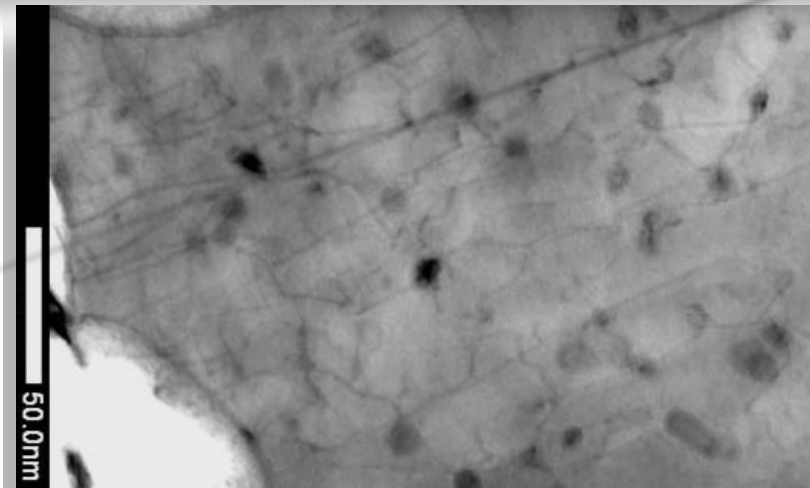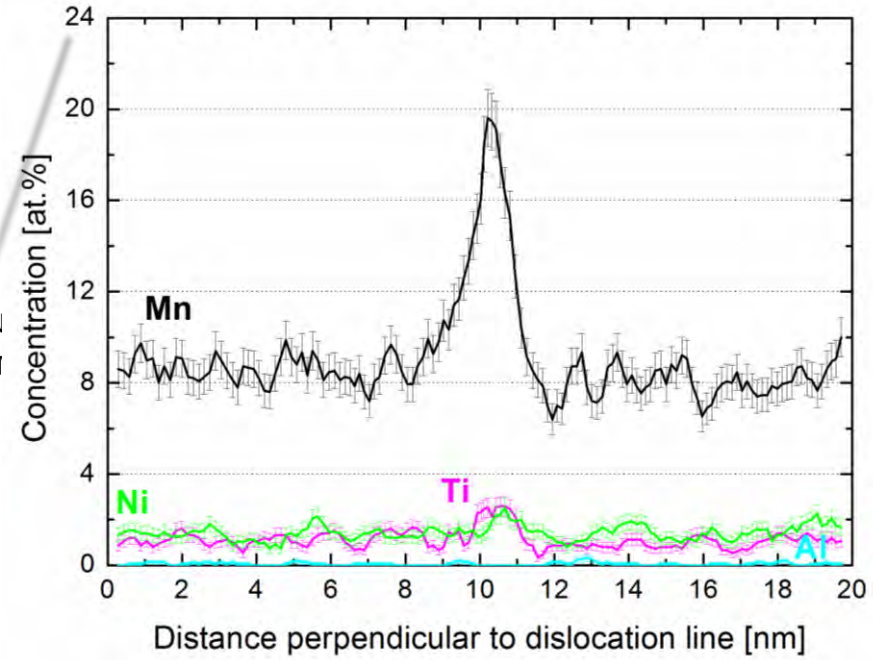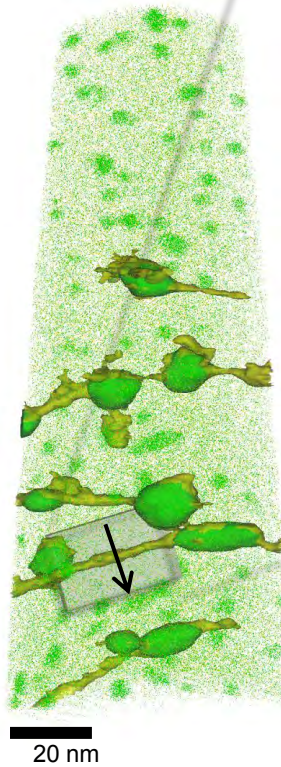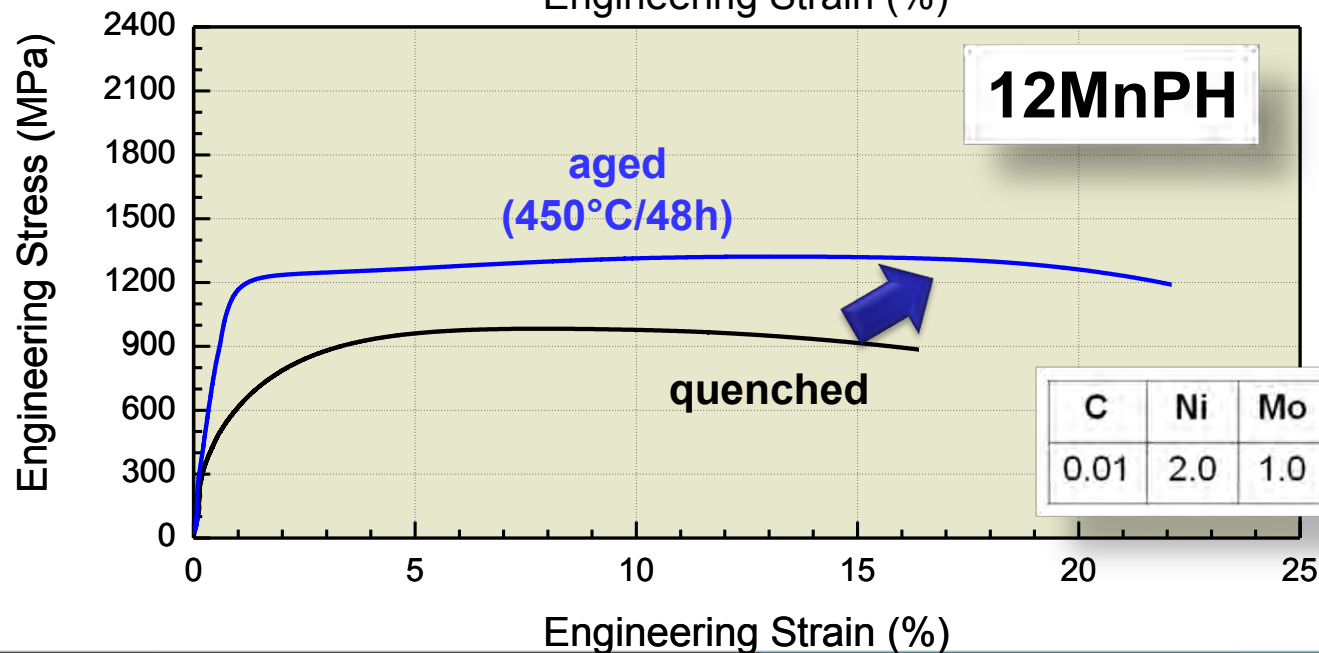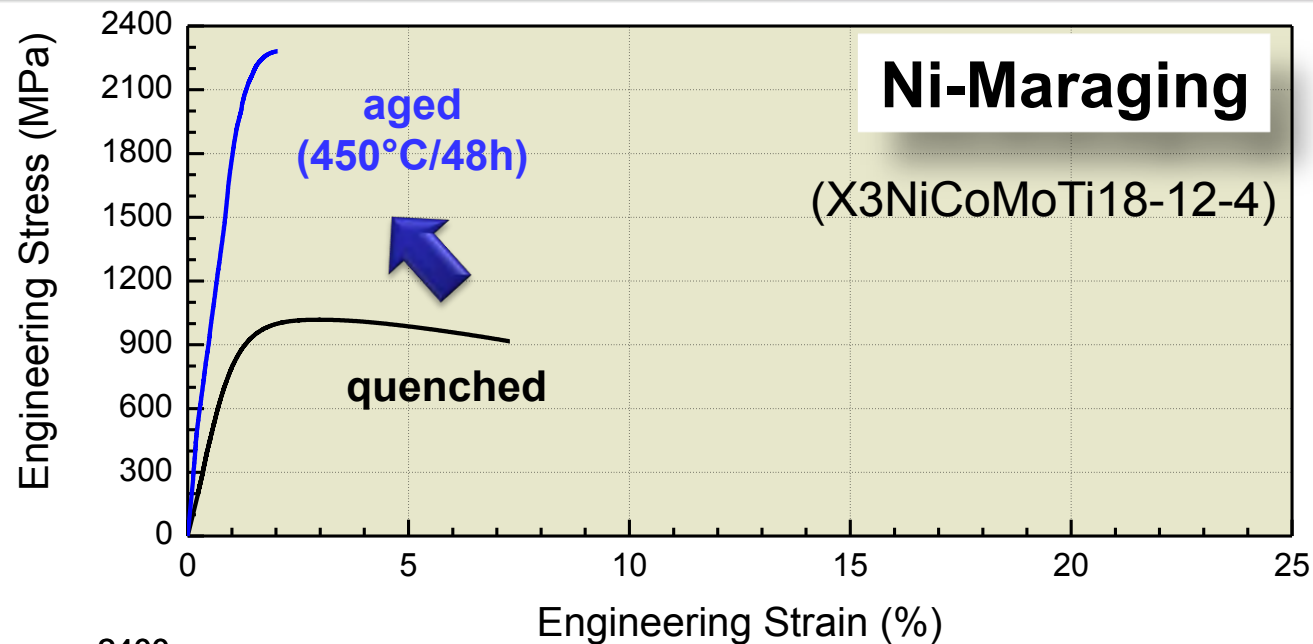
C	Ni	Mo	Ti	Al	Mn	Fe
0.01	2.0	1.0	1.0	0.15	12	bal.

Max-Planck-Institut für Eisenforschung, Düsseldorf, Germany

D. Raabe et al. Scripta Materialia 60 (2009) 1141

650 MPa to 2 GPa

Making martensite ductile
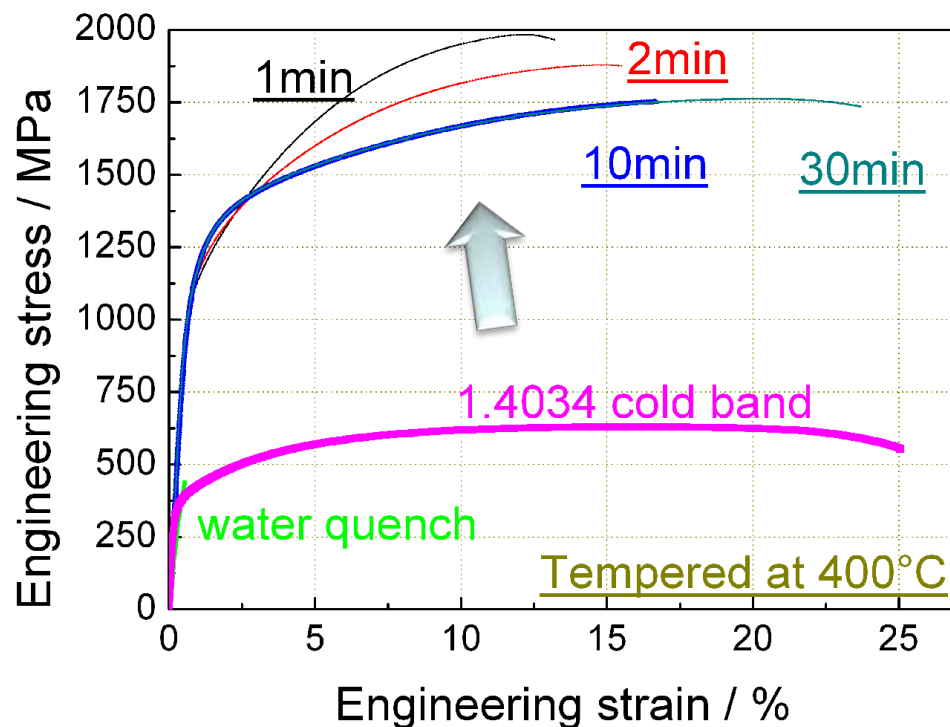
400°C aging:
precipation + <u>austenite reversion</u>

Fe-13.6Cr-0.44C (wt.%)
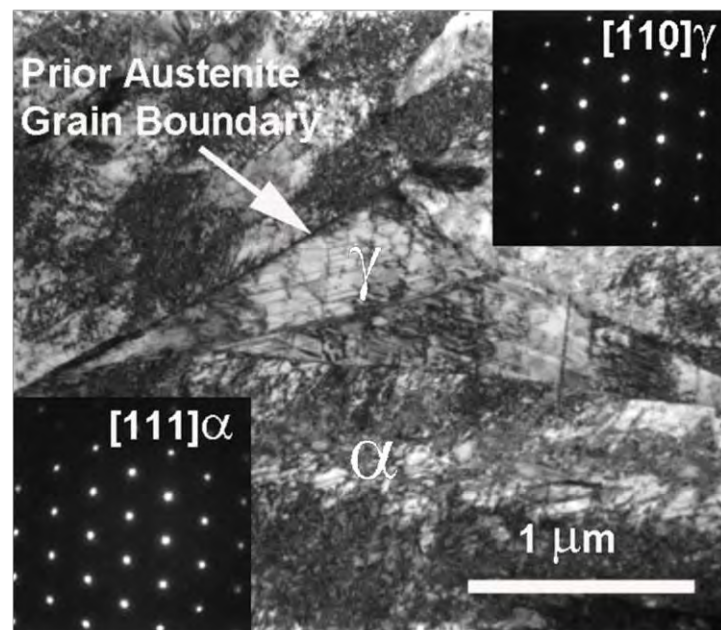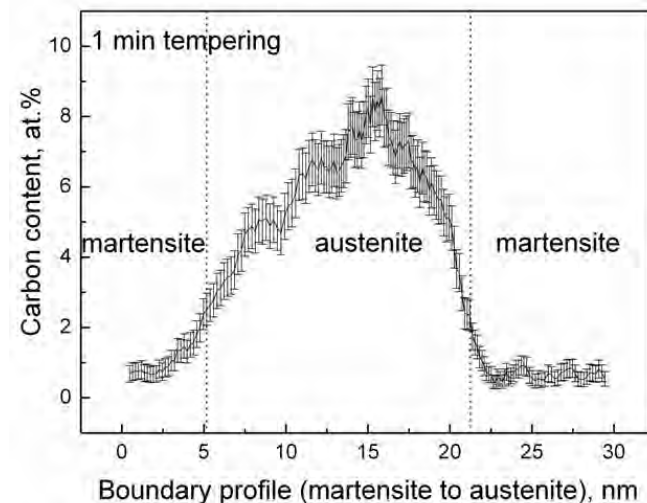
- **Design alloys by self-organized nanostructuring**

- **Segregation plus confined phase transformation at defects**

- **Works for dislocations too?**

- **Deformation-driven mechanical bulk alloying leads to non-equilibrium phases approaching the theoretical limits of strength**

Thank you for the attention
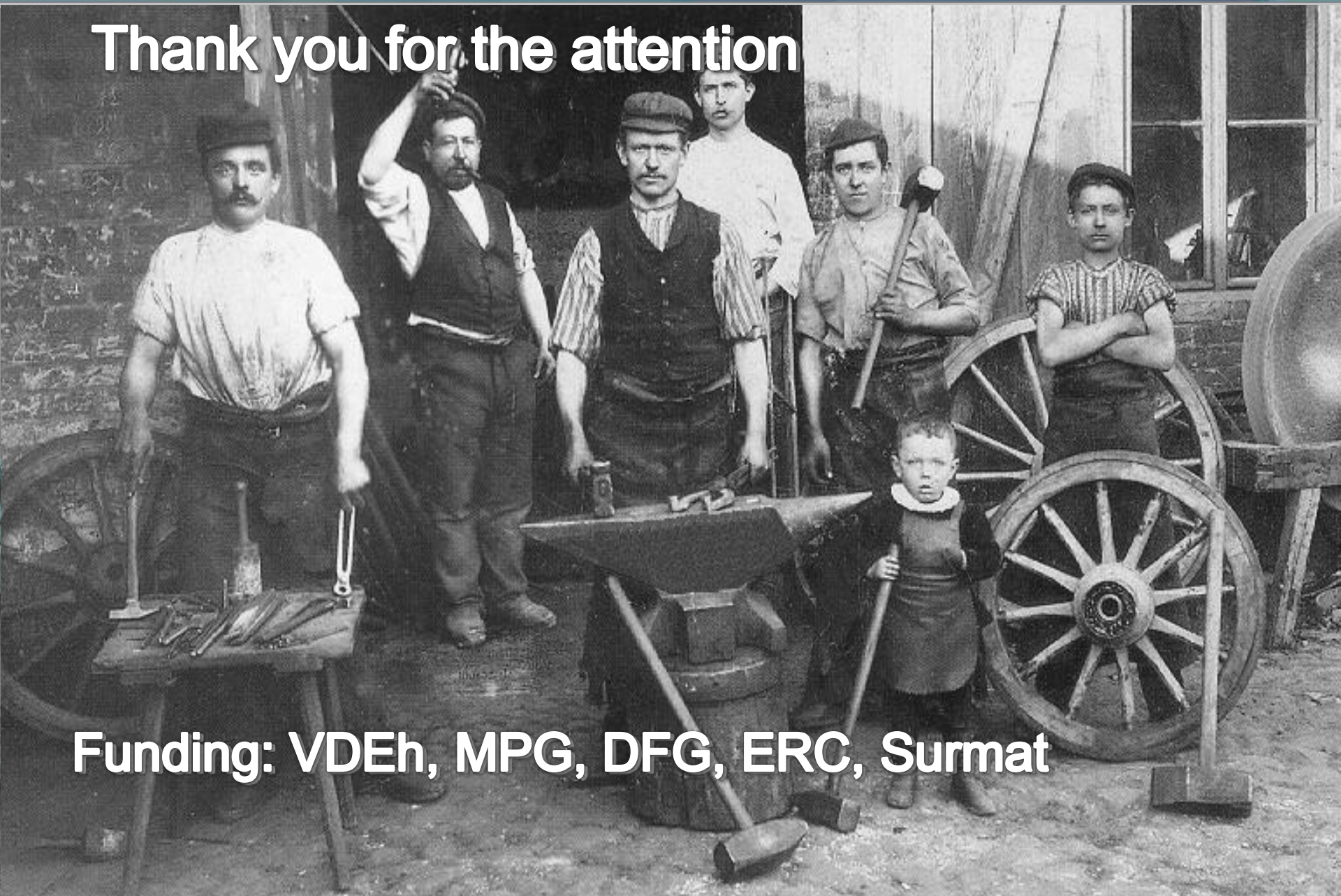
Funding: VDEh, MPG, DFG, ERC, Surmat

D. Raabe, P. P. Choi, Y.J. Li, A. Kostka, X. Sauvage, F. Lecouturier, K. Hono, R. Kirchheim, R. Pippan, D. Embury: MRS Bulletin 35 (2010) 982-991, Metallic composites processed via extreme deformation: Toward the limits of strength in bulk materials

Y.J. Li, P. Choi, C. Borchers, Y. Z. Chen, S. Goto, D. Raabe, R. Kirchheim: Ultramicroscopy 111 (2011) 628–632, Atom probe tomography characterization of heavily cold drawn pearlitic steel wire

Y.J. Li, P. Choi, S. Goto, C. Borchers, D. Raabe, R. Kirchheim: Acta Materialia, Volume 60, Issue 9, May 2012, Pages 4005-4016, Evolution of strength and microstructure during annealing of heavily cold-drawn 6.3 GPa hypereutectoid pearlitic steel wire

Y.J. Li, P. Choi, S. Goto, C. Borchers, D. Raabe, R. Kirchheim: Acta Materialia, Volume 60, Issue 9, May 2012, Pages 4005-4016, Evolution of strength and microstructure during annealing of heavily cold-drawn 6.3 GPa hypereutectoid pearlitic steel wire

L. Yuan, D. Ponge, J. Wittig, P. Choi, J.A. Jiminez, D. Raabe: Acta Materialia 60 (2012) 2790–2804, Nanoscale austenite reversion through partitioning, segregation and kinetic freezing: Example of a ductile 2 GPa Fe–Cr–C steel

D. Raabe, D. Ponge, O. Dmitrieva, B. Sander: Scripta Materialia 60 (2009) 1141–1144, Nano-precipitate hardened 1.5 GPa steels with unexpected high ductility

O. Dmitrieva, D. Ponge, G. Inden, J. Millán, P. Choi, J. Sietsma, D. Raabe: Acta Materialia 59 (2011) 364-374, Chemical gradients across phase boundaries between martensite and austenite in steel studied by atom probe tomography and simulation

Thermodynamics of carbon solubility in ferrite and vacancy formation in cementite in strained pearlite

Gh. Ali Nematollahi *, Johann von Pezold, Jörg Neugebauer, Dierk Raabe

Max-Planck-Institut für Eisenforschung, D-40237 Düsseldorf, Germany

Abstract

In order to investigate the thermodynamic driving force for the experimentally observed accumulation of C in ferritic layers of severely plastically deformed pearlitic wires, the stabilities of C interstitials in ferrite and of C vacancies in cementite are investigated as a function of uniaxial stain, using density-functional theory. In the presence of an applied strain along [1 1 0] or [1 1 1], the C interstitial in ferrite is significantly stabilized, while the C vacancy in cementite is moderately destabilized by the corresponding strain states in cementite [1 0 0] and ([0 1 0]). The enhanced stabilization of the C interstitial gives rise to an increase in the C concentration within the ferritic layers by up to two orders of magnitude. Our results thus suggest that in addition to the generally assumed non-equilibrium, dislocation-based mechanism, there is also a strain-induced thermodynamic driving force for the experimentally observed accumulation of C in ferrite.

© 2012 Acta Materialia Inc. Published by Elsevier Ltd. All rights reserved.

Keywords: Density-functional theory; Ferrite; Cementite; Carbon interstitial; Vacancy formation energy

1. Introduction

Severely plastically deformed steels have great technological importance as high-strength materials. Among them, heavily cold drawn pearlitic steels exhibit the highest tensile strength (5–6 GPa) of any nanostructured, bulk material known to date [1,2]. Despite numerous experimental and theoretical investigations [1–9] the mechanism underlying the extraordinary strength of this material is not yet fully understood. In particular, the correlation between the microstructural properties of the material and its tensile strength has not been fully established. However, the development of novel experimental methods with atomic or near-atomic chemical and structural resolution, such as 3-D atom probe tomography and high-resolution transmission electron microscopy (HR-TEM), now provides us with an unprecedented level of insight into both the microstructural features and the local chemical composition of these materials [1,2]. This improved understanding enables us to refine our models of the extreme strengthening effect of severe plastic deformations in pearlitic wires, which may be evaluated and assessed by further experiments and or theoretical predictions. While earlier studies have focused on the effects of the evolving dislocation substructure during wire drawing and the resulting strength [3,2], chemical effects, such as the stabilization of interstitial excess C in the ferrite matrix, and its influence on strength, have not so far been investigated. In this study, we investigate the experimentally observed dissolution of the cementite lamellae in severely deformed pearlitic structures from a theoretical point of view.

Experimental evidence shows that during the wire-drawing process, the lamellar structure of pearlite is refined to a ferrite–cementite interface spacing of several nanometers and the cementite structure gradually decomposes [2,5,10–13,7,14]. While the Hall–Petch-type strengthening due to the lamellar refinement is well established [15], the mechanism underlying the decomposition of the cementite structure is more controversial [5,16]. Moreover, the effect

---

* Corresponding author. Tel.: +49 2116792446.
  E-mail address: a.nematollahi@mpie.de (Gh.A. Nematollahi).

of the dissolved C atoms in the ferrite matrix is still also under debate. These atoms can either segregate to microstructural defects, such as dislocations or grain boundaries, or dissolve in bulk-like regions of the ferritic matrix. Atom probe tomography studies reveal that, while carbon atoms do segregate to extended defects, such as grain boundaries, the bulk concentration of C in ferrite is also dramatically increased [6]. More specifically it was observed that the C concentration in bulk-like regions of ferrite can reach up to 1 at.% after wire drawing, which corresponds to an increase in the bulk C concentration by nine orders of magnitude, as compared to its equilibrium solubility at room temperature (10^{-5} ppm). Moreover, differential scanning calorimetry (DSC)-based analyses of wire-drawn pearlitic steels exhibit a peak at relatively low temperatures (around 160 °C), which is attributed to the migration of supersaturated carbon within the ferrite matrix to dislocation cores, corresponding to the initial stage of strain ageing [17–19]. The accumulation of C in ferrite is generally attributed to the severe plastic deformation during wire-drawing experiments, which is supposed to result in a dislocation-driven transfer of C from the cementite–ferrite interface into the ferritic layers [5,1]. A strain-induced increase in the C solubility in ferrite constitutes an alternative mechanism that may also explain the observed redistribution of C. This thermodynamic driving force has not previously been considered. To estimate the importance of this mechanism we consider the stability of C in ferrite as a function of applied uniaxial strains using density-functional theory (DFT).

The dissolution of C atoms above a critical concentration of ≈0.18 wt.% at room temperature [20] is known to induce an ordering of the C solutes within a single sublattice of the ferritic matrix [21,22], resulting in the formation of the tetragonally distorted martensite phase. Microscopically this tetragonal distortion is induced by the reduced symmetry of the octahedral cage in body-centred cubic (bcc) structures. Hence, two of the Fe atoms forming the octahedral cavity (the ones along any of the three principal axes of the bcc lattice) are closer to the central C atom than the other four, which results in more pronounced relaxations along this direction. An increased C solubility is therefore anticipated if the tensile load is applied along the nearest-neighbour direction around the C atom in the octahedral cavity of the ferritic matrix. The effect of hydrostatic pressure on the C solubility in α-Fe has been investigated previously using DFT calculations, which revealed an increased solubility with increasing interstitial volume [23,24]. However, the effect of uniaxial strains, as applied in severe plastic deformation experiments, such as wire drawing, has not so far been considered. We therefore investigate the formation energy of C interstitials in α-Fe using DFT, as a function of the external loads applied during the wire-drawing experiment. Moreover, in order to establish the thermodynamic driving force for the dissolution of cementite, the formation of C vacancies in cementite is considered under corresponding strain conditions.

2. Simulation method

Although a number of orientation relationships between bcc Fe and cementite in pearlite have been reported over the years, the Bagaryatsky [25], Isaichev [26] and Pitsch–Petch [27] orientation relationships are most commonly observed:

$[100]_{cem} \| [1\bar{1}0]_{f}$	
$[010]_{cem} \| [111]_{f}$	Bagaryatsky
$(001)_{cem} \| (11\bar{2})_{f}$	
$[010]_{cem} \| [111]_{f}$	Isaichev
$(103)_{cem} \| (01\bar{1})_{f}$	
$[100]_{cem}$ 2.6° from $[\bar{3}1\bar{1}]_{f}$	
$[010]_{cem}$ 2.6° from $[131]_{f}$	Pitsch–Petch
$(001)_{cem} \| (\bar{2}\bar{1}5)_{f}$	

In the present study, we consider the Bagaryatsky orientation relationship. In this orientation relationship, the phase boundary between ferrite and cementite is formed by the $(001)_{cem}$ habit plane of cementite and the $(11\bar{2})_{f}$ habit plane of ferrite (subscripts are used to indicate the reference system—ferrite or cementite—of crystallographic data throughout this paper). Based on this orientation relationship the cell vectors of the supercells used for the description of ferrite in our DFT simulations were rotated to point along the $[1\bar{1}0]_{f}$, $[111]_{f}$ and $[11\bar{2}]_{f}$ directions.

Electron microscopy images of pearlite colonies showed that they topologically align along the wire axis [3]. Hence at a true (logarithmic) wire strain of $\varepsilon = 2$ the majority of pearlite colonies are aligned with the wire-drawing axis and a $[110]_{f}$ fibre texture is developed in ferrite [7,3,15]. As an initial assumption for our DFT calculations, the drawing direction was therefore assumed along $[110]_{f}$ in ferrite and the corresponding $[100]_{cem}$ direction in cementite. In addition, strains along $[111]_{f}$ and the corresponding $[010]_{cem}$ were also considered.

While in bulk ferrite all octahedral (Oh) sites are equivalent, the application of an external load induces a non-degeneracy of the interstitial sites. In the case of an applied load along $[110]_{f}$, the two Oh sublattices with nearest-neighbour Fe atoms along the $[100]_{f}$ and $[010]_{f}$ directions remain degenerate, while the third Oh sublattice with the nearest-neighbour Fe atoms along the $[001]_{f}$ direction is different, as the applied load has no force component along that direction. In order to investigate the effect of an applied strain along $[110]_{f}$ on the equilibrium C-concentration in ferrite, two sets of Oh interstitial sites have therefore been considered, involving nearest-neighbour Fe atoms along the $[100]_{f}$ and $[001]_{f}$ directions, respectively.

The orthorhombic unit cell of cementite contains contains 12 Fe atoms and four C atoms. Its 12 Fe atoms are located in two distinct lattice sites: the special Fe2 sites (Wyckoff position 4c) and the general Fe1 site (Wyckoff position 8d). The nearest-neighbour atoms around C are two Fe1 and four Fe2 atoms [28]. These six Fe atoms form

a trigonal prism in the centre of which the C atom is located (see Fig. 1). As shown in Fig. 1, two different orientations of these prisms exist within the cementite structure, which may respond differently to an applied load. For the determination of the C-vacancy formation energy as a function of applied strain, we therefore considered both environments.

Spin-polarized DFT calculations [29,30] were performed using the projector-augmented wave method [31] and a plane-wave basis set, as implemented in the Vienna Ab-initio Simulation Package (VASP) [32]. The electronic exchange and correlation interactions were approximated by the generalized-gradient-approximation (GGA), as parametrized by Perdew, Burke and Ernzerhof (PBE) [33].

The **k**-point meshes for the Brillouin zone integration were constructed using the Monkhorst–Pack scheme [34]. Based on a careful convergence test of the structural parameters and energetics, 11,000 **k**-points × atoms were found to be required to accurately describe – ferrite both in the absence and in the presence of C, while for cementite ≈20,000 **k**-points × atoms – and for diamond ≈1500 **k**-points × atoms were needed. The above mentioned **k**-point densities were used for all calculations of each corresponding phase in this work. A plane-wave energy cut-off of 450 eV was found to be sufficient to converge the bulk modulus and structural parameters for bcc Fe, cementite and the dilute Fe–C system. The electronic temperature was set to 0.2 eV in conjunction with the first-order Methfessel–Paxton smearing scheme [35]. The lattice parameter, bulk modulus and local magnetic moment obtained for pure bcc Fe are 2.833, 187 GPa and $2.2\mu_B$, respectively,

in good agreement with experimental data and previous theoretical studies at 0 K (maximum deviation from experiment of 1.4%) [36,23]. The bulk modulus and lattice parameters of cementite obtained using this setup are $B = 220$ GPa, $a = 5.050$ Å, $b = 6.695$ Å and $c = 4.488$, which are again in good agreement with previous experimental and theoretical results (maximum deviation from experiment of 0.6%) [37,38]. To calculate the total energy of the different systems as a function of the strain state, both the ionic positions and the lattice dimensions normal to the applied strain were fully relaxed.

3. Results

3.1. Carbon dissolution in α-iron

In this section, we consider the stability of ferrite as a function of an external strain, both in the presence and in the absence of interstitial C atoms. As discussed above, the addition of C expands the bcc lattice in the direction of the two nearest-neighbour Fe atoms around the C interstitial. In line with our expectation, Fig. 2 shows that the ground state structure of the Fe–C system is shifted towards positive strains if the applied strain has components along the nearest-neighbour direction, while in the absence of any strain components along that direction, no energy can be gained by the application of the external strain, and the ground state structure corresponds to the $\varepsilon = 0$ configuration. In the case of an applied strain along $[1\,1\,0]_f$ (Fig. 2a) the degenerate interstitial configurations involving nearest-neighbour Fe atoms along $[1\,0\,0]_f$
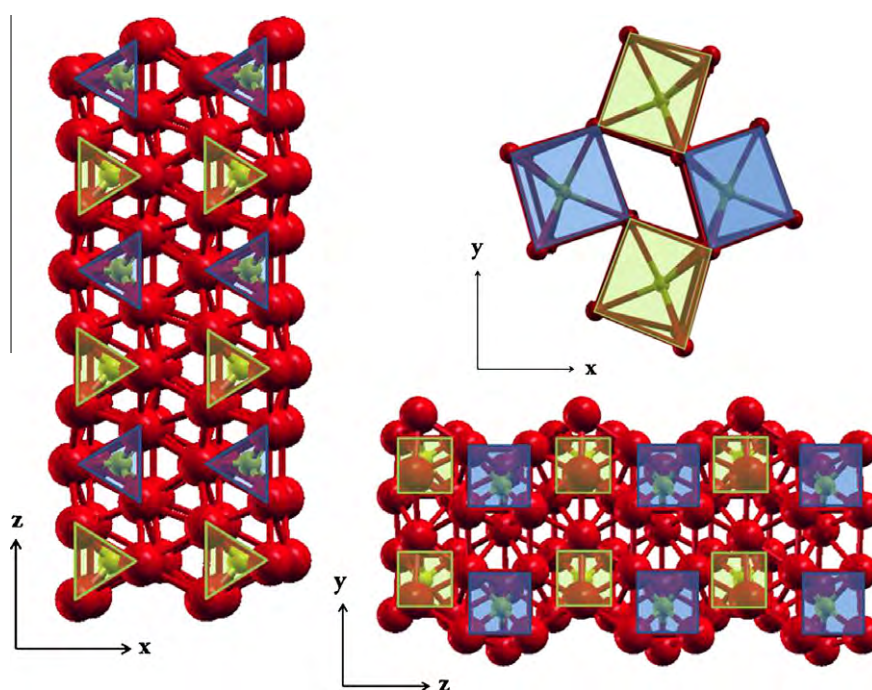
Fig. 1. Crystal structure of cementite (Fe₃C). Red and blue spheres represent Fe and C atoms, respectively. In the cementite structure, C atoms occupy the centre of the trigonal prisms in two different orientations (blue and light green shading in the figure) and Fe atoms occupy the vertices of these prisms. (For interpretation of the references to colour in this figure legend, the reader is referred to the web version of this article.)
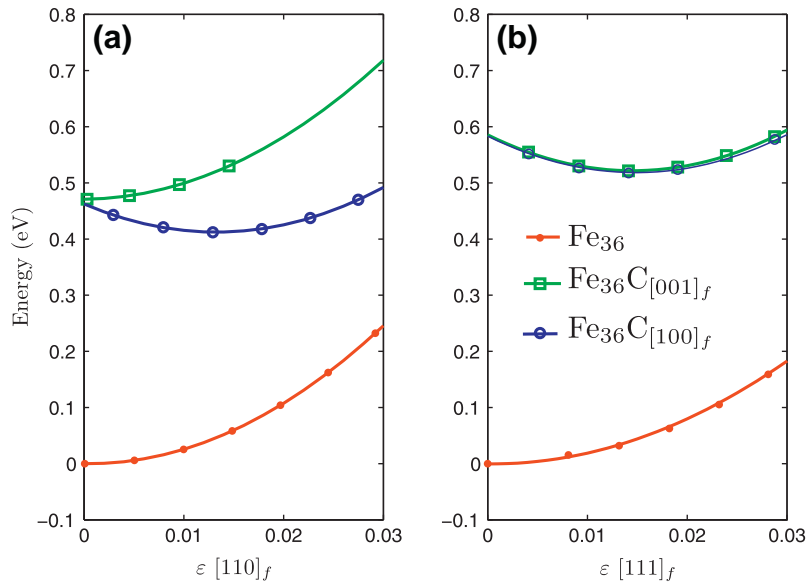
Fig. 2. Variation of the total energy of bcc Fe in the presence and in the absence of a C interstitial with respect to an applied strain along (a) $[110]_f$ and (b) $[111]_f$. $Fe_{36}C_{[001]}$ and $Fe_{36}C_{[100]}$ correspond to the energy of the systems containing 36 Fe atoms and one C interstitial in an Oh site with nearest neighbours (nnb) Fe atoms along $[001]_f$ and $[100]_f$, respectively. Strains and energies are expressed with respect to the ground state of bcc Fe. In order to ensure the same stoichiometry for all structures considered in the plots, the cohesive energy of a C atom in the diamond structure was subtracted from the total energy of the C-containing systems (Fe_{36}).

($Fe_{36}C_{[100]}$) and $[010]_f$ are stabilized (minimum energy at $\varepsilon > 1\%$), while the interstitial structure involving nearest-neighbour Fe atoms along $[001]_f$ ($Fe_{36}C_{[001]}$) is not significantly affected by the applied strain (its minimum energy configuration corresponds to the $\varepsilon = 0$ state). In the case of an applied load along $[111]_f$ all three Oh sublattices are energetically degenerate. Hence, both $Fe_{36}C_{[100]}$ and $Fe_{36}C_{[001]}$ are stabilized by the applied strain and their minimum energy states are shifted to $\varepsilon \sim 0.9\%$ (see Fig. 2b).

To quantify the effect of the applied external strains on the equilibrium carbon concentration, the formation energy (E_C^f) of a carbon interstitial in bcc Fe was calculated for the two configurations using:

$$E_{int}^f(\varepsilon) = E_{Fe-C}^{int}(\varepsilon) - E_{Fe}(\varepsilon) - \mu_C, \qquad (1)$$

where E_{Fe-C}^{int} is the total energy of bcc Fe with a C interstitial in a given strain state, ε, and E_{Fe} is the total energy of bulk iron in the same strain state. μ_C is the C chemical potential. We disregard any enthalpic contributions in our analysis of the thermodynamic stability, as the volume work is in fact done by the experimental setup, rather than by the ferrite/cementite phases themselves.

Considering diamond as the reference phase for the C chemical potential, the strain-dependent formation energy shown in Fig. 3 reveals a significant stabilization of interstitial C in bcc Fe in the presence of the different external strains considered in this study. The most significant stabilizations are found in the presence of strains along $[110]$ (≈ 0.3 eV at $\varepsilon = 0.03$), while strains along $[111]$ induce a slightly weaker stabilization of ≈ 0.2 eV at $\varepsilon = 0.03$.

To further elucidate the mechanism underlying the observed stabilization of an interstitial C atom by an applied strain along $[110]_f$, the excess energy of C was plotted as a function of the nearest-neighbour (nnb) separation of the C atom in the Oh cavity, as shown in Fig. 4, which clearly reveals a linear dependence between the nnb distance and the calculated formation energy.

3.2. Vacancy formation energy in cementite

The above results suggest that external strains applied parallel to the ferrite–cementite interface dramatically reduce the heat of solution of C in ferrite. However, in order to assess the strain-induced thermodynamic driving force for the migration of C from cementite to ferrite within the pearlite microstructure, we also need to consider the formation of C vacancies in cementite under the corresponding strains along $[100]_{cem}$ and $[010]_{cem}$, as given by the Bagaryatsky orientation relationship. Irrespective of which C site within the cementite matrix is considered, the C vacancy is found to be destabilized by strains along either direction, as shown in Fig. 5. The destabilization of the C vacancy can be understood by the reduced equilibrium volume of the cementite matrix in the presence of a C vacancy. Hence, irrespective of the direction of the applied strain and the nature of the C site, the minimum-energy configuration of the cementite vacancy system is found to be shifted towards negative strain states, which is why the external tensile load considered here induces a destabilization.

In order to quantify this destabilization, the vacancy formation energy within cementite was calculated in analogy to the formation energy of the C interstitial in ferrite, using:

$$E_{vac}^f(\varepsilon) = E_{Fe_3C}^{vac}(\varepsilon) - E_{Fe_3C}(\varepsilon) + \mu_C, \qquad (2)$$
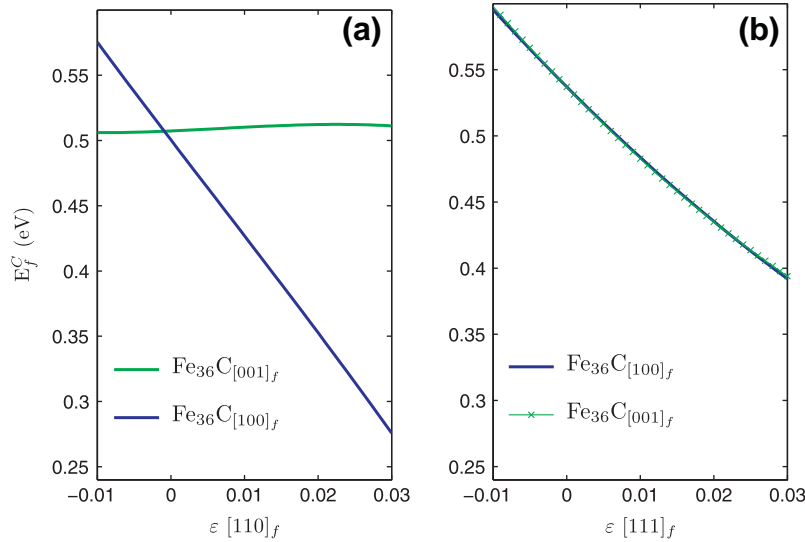
Fig. 3. Dependence of the formation energy of a C interstitial in bcc Fe on the strain along (a) $[1\,1\,0]_f$ and (b) $[1\,1\,1]_f$. $Fe_{36}C_{[100]}$ and $Fe_{36}C_{[001]}$ refer to the energy of the Oh sites with nnb Fe atoms along $[1\,0\,0]_f$ and $[0\,0\,1]_f$, respectively.
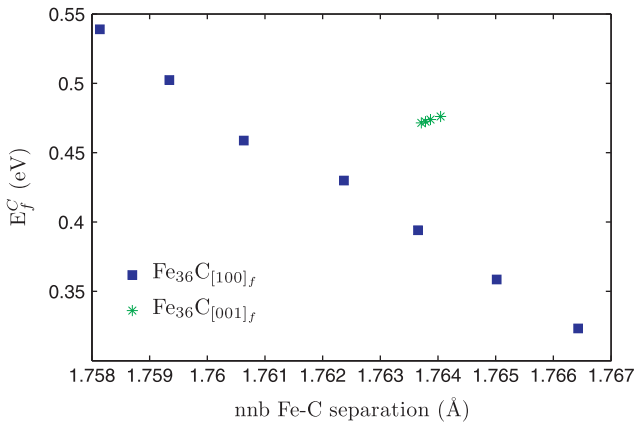
Fig. 4. Formation energy of a C interstitial in ferrite as a function of the separation of the nnb Fe atoms.

where $E_{Fe_3C}^{vac}$ and E_{Fe_3C} are the total energy of cementite in the presence and in the absence of a vacancy, respectively, and μ_C is the C chemical potential, which was set to the cohesive energy of C in the diamond structure. The formation energies shown in Fig. 6 suggest that the strain-induced destabilization of the C vacancy in cementite is much less pronounced than the corresponding stabilisation of the C interstitial in ferrite. Hence the vacancy structures in cementite were found to be destabilized by at most 0.1 and 0.04 eV in the presence of external strains along $[1\,0\,0]_{cem}$ and $[0\,1\,0]_{cem}$, respectively, while the interstitial C configurations within the ferrite matrix are stabilized by ≈ 0.3 and 0.2 eV in the corresponding strain states.

4. Discussion

In this section, we will consider the experimentally observed decomposition of cementite within pearlite during the wire-drawing experiment from a thermodynamic point of view. Hence the decomposition of cementite is assumed to proceed via the formation of C vacancies in cementite and the subsequent incorporation of the C atoms in the ferrite matrix. The thermodynamic driving force for this process is given by the relative stability of C in the two phases as a function of the applied external strain. The more pronounced strain-induced stabilization of the C interstitial in ferrite, as compared to the corresponding destabilization of the C vacancy in cementite, suggests that the transfer of C from cementite to ferrite should become thermodynamically more favourable, as the external strain is increased (see Fig. 8). However, the strain state of the two phases is strongly dependent on their orientation with respect to the applied strain. In the case of an applied strain along the ferrite–cementite interface, the two phases will be in the same strain state (Voigt limit [39], Fig. 7a), while in the case of applied strains normal to the ferrite–cementite interface the stress rather than the strain across the ferrite–cementite interface will be constant (Reuss limit [39], Fig. 7b). In the context of our DFT calculations considering only strains along the ferrite–cementite interface, the Voigt limit is representative of experimental conditions in which the lamellar structure of pearlite is conserved, while the Reuss limit is representative of experimental conditions involving partially dissolved cementite layers (see Fig. 7c). In our analysis we have considered both cases, as described below.

4.1. Voigt limit

In order to determine the thermodynamic driving force for the transfer of C from ferrite to cementite in the Voigt limit, the reaction energy (E^{rxn}) was calculated using:

$$E^{rxn} = E_{int}^f(\varepsilon_f) + E_{vac}^f(\varepsilon_{cem}) \tag{3}$$

assuming the same strain state in the ferrite and the cementite matrix ($\varepsilon_f = \varepsilon_{cem}$). Under these conditions the
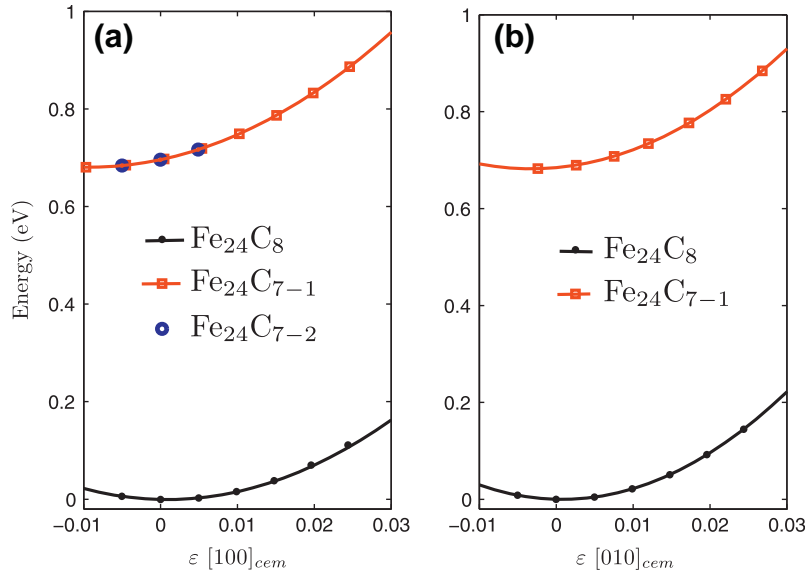
Fig. 5. Total energy of cementite in the presence and in the absence of a vacancy as a function of tensile strain along (a) [100] and (b) [010]. $Fe_{24}C_{7-1}$ and $Fe_{24}C_{[7-2]}$ correspond to the different environments of the C vacancy in cementite, while $Fe_{24}C_8$ indicates the energy of bulk cementite. Both strains and energies are referenced to the ground state properties of cementite. The cohesive energy of a C atom in the diamond phase is added to the energy of the vacancy structures to ensure the same stoichiometry for the different systems considered in the plots.
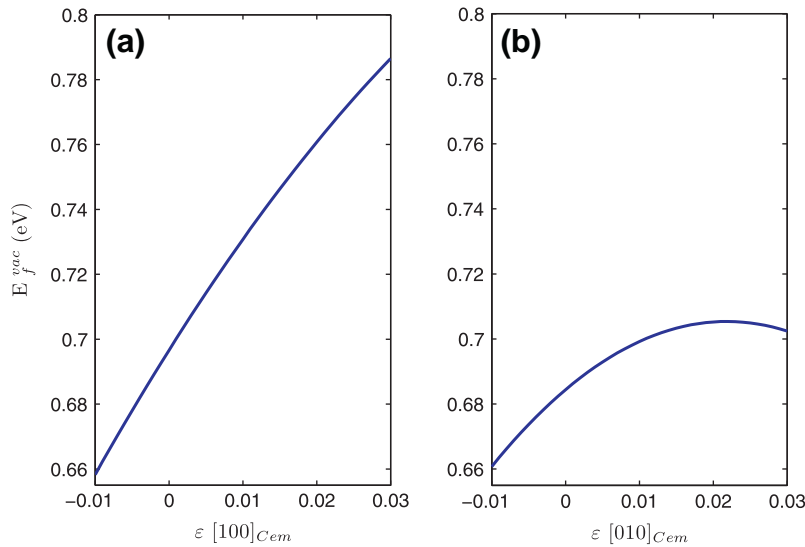
Fig. 6. Vacancy formation energy in cementite as a function of an applied strain along (a) [100]$_{cem}$ and (b) [010]$_{cem}$.

transfer of C from cementite into an Oh site in ferrite involving nearest-neighbour atoms along [001]$_f$ is destabilized by an external strain along [110]$_f$ ([100]$_{cem}$), while the dissolution of C atoms in the Oh sublattice involving nearest-neighbour atoms along [100] is stabilized (see Fig. 8). In practice this will result in a preferential dissolution of C in the latter sublattice. Conversely, the degenerate nature of the Oh sublattices in ferrite under an applied strain along [111]$_f$ is again revealed by the degenerate reaction energetics for the transfer of C from cementite to ferrite, as shown in Fig. 8b.

Under the assumption of ideal solutions in the dilute limit we estimate the equilibrium C concentration in ferrite and the vacancy concentration in cementite as a function of temperature and the applied strain. The number of C atoms in octahedral sites of α-Fe (N_{int}), is given by:

$$N_{int}(\varepsilon) = \sum_i^3 \frac{1}{3} N_{oct} \exp\left(-\frac{E_{int_i}^f(\varepsilon)}{k_B T}\right), \tag{4}$$

where N_{oct} is the number of octahedral sites in α-Fe, k_B is the Boltzmann constant and E_{int}^f is the formation energy of a C interstitial (see Eq. (1)). The sum runs over the three Oh sublattices in ferrite. The number of vacancies in cementite (N_{vac}) is similarly given by:

$$N_{vac}(\varepsilon) = N_C \exp\left(-\frac{E_{vac}^f(\varepsilon)}{k_B T}\right), \tag{5}$$
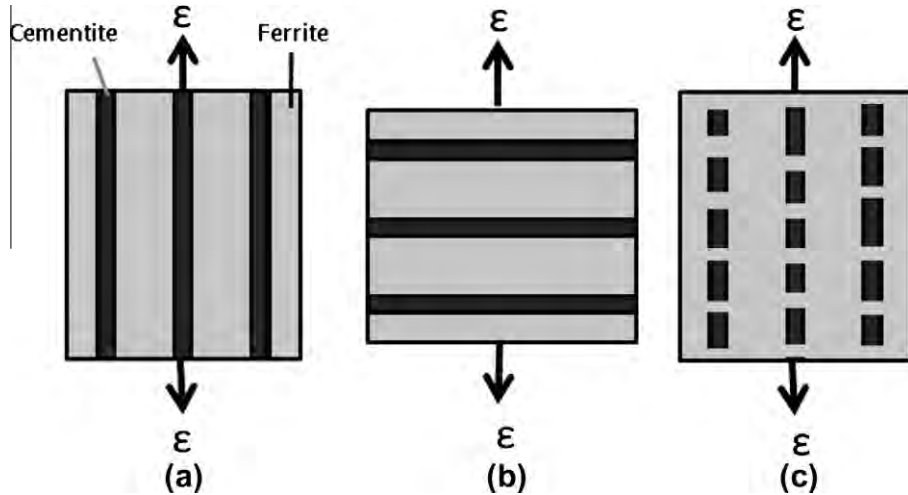
Fig. 7. Schematic of (a) the Voigt (iso-strain) and (b) Reuss (iso-stress) limit. In (c) the realization of iso-stress conditions inside a pearlitic microstructure involving a partially dissolved cementite layer is schematically shown.
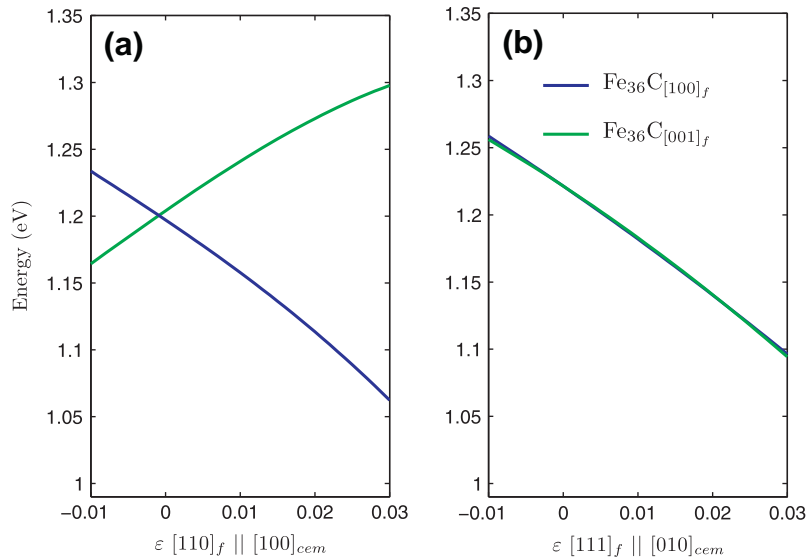
Fig. 8. Calculated reaction energy of transferring C from cementite to ferrite, as a function of strain along (a) $[1\,1\,0]_f$ and (b) $[1\,1\,1]_f$ in ferrite and the corresponding directions in cementite, as given by the Bagaryatsky orientation relationship. A constant strain state across the ferrite–cementite interface was assumed (Voigt limit).

where N_C is the number of C sites and E_{vac}^f is the C vacancy formation energy in cementite (see Eq. (2)). Considering a eutectoid composition (4 at.% C), N_{oct} is found by assuming that all C is initially dissolved in cementite. Under this assumption and the known stoichiometry of cementite, 16% of atoms will constitute the cementite phase, while the remaining 84% correspond to the ferrite fraction. Given that there are three Oh sites for every Fe atom in ferrite and referencing to a total of 100 atoms, N_{oct} will be equal to 252, while N_C is equal to 4. Since a C vacancy has to be formed in cementite for every C interstitial in ferrite, the strain-dependent equilibrium C chemical potential can be found by equating Eqs. (4) and (5), noting that E_{int}^f and E_{vac}^f are related to μ_c via Eqs. (1) and (2). Finally, the

equilibrium C concentration in ferrite and vacancy concentration in cementite at a given strain state are found by evaluating Eqs. (4) and (5), respectively, using this equilibrium C chemical potential.

Considering the iso-strain model (Voigt limit), the equilibrium C concentration in ferrite as a function of the applied strain is shown in Fig. 9. The maximum strain of 3% considered in this analysis corresponds to the calculated strain in the ferrite matrix at the yield point of cold-drawn pearlitic wires (6.3 GPa) [40] and hence constitutes the upper limit of possible strains within the pearlitic microstructure.

Fig. 9 reveals a significant enhancement in the equilibrium C concentration within the ferritic layers of the
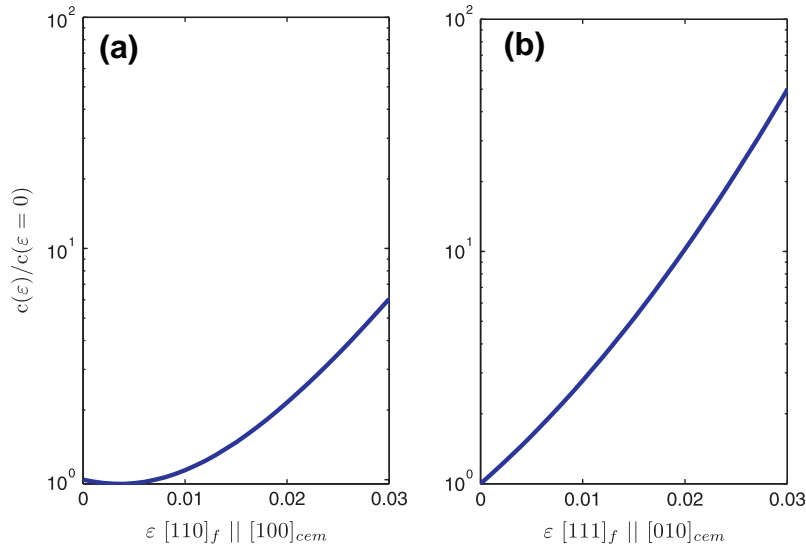
Fig. 9. Relative C concentration in ferrite particles within pearlitic microstructures at 300 K as a function of an applied strain along (a) $[110]_f$ and (b) $[111]_f$ in ferrite and the corresponding directions in cementite, as given by the Bagaryatsky orientation relationship, assuming iso-strain conditions across the ferrite–cementite interface (Voigt limit).

cementite microstructure with increasing strain. In particular, applied strains along $[110]_f$ give rise to an increase in the equilibrium C concentration of up to ≈ 1 order of magnitude, while strains along $[111]_f$ give rise to a somewhat more pronounced enhancement in the C concentration of almost 2 orders of magnitude at an applied strain of 3%. The smaller increase in the equilibrium C concentration under an external strain along $[110]_f$ ($[100]_{cem}$ in cementite) can be traced back to the anisotropy of the Oh sublattices in ferrite under this applied strain (see Fig. 4a) and the somewhat larger vacancy formation energy in cementite in the corresponding strain state (see Fig. 6a).

4.2. Reuss limit

The equilibrium C concentration in ferrite as a function of applied strain, under a constant stress regime (Reuss limit), was found by first determining the strains within the two phases (ε_f and ε_{cem}) at a given stress (0 $\leqslant 6.3$ GPa) using the stress–strain curves obtained from our DFT calculations (see Figs. 10 and 11).

The strain states thus determined were used to calculate the corresponding formation energy of a C interstitial in ferrite and a C vacancy in cementite using Eqs. (1) and (2). These formation energies could then be used to
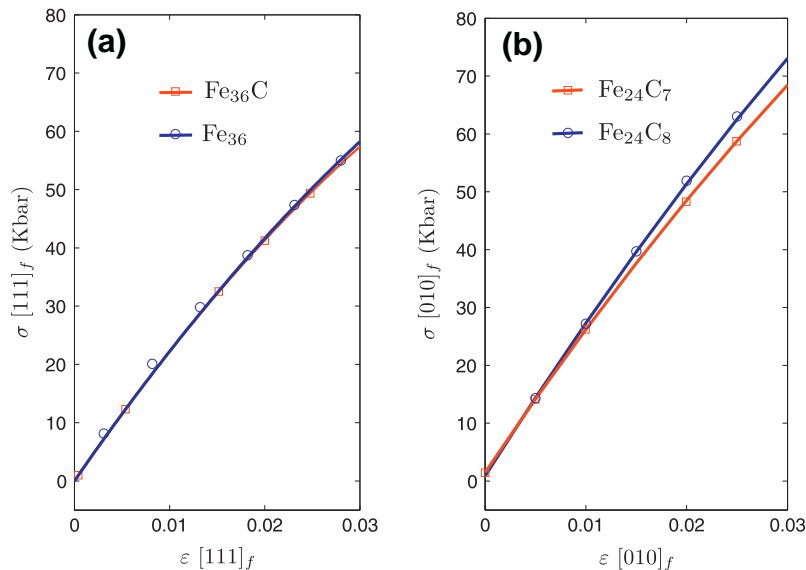
Fig. 10. Variation of the stress (σ) as a function of the applied strain along (a) the $[111]$ direction in ferrite in the presence and absence of an interstitial C atom and (b) the $[010]$ direction in cementite in the presence and absence of a C vacancy. Very similar dependencies were found as a function of external strains along $[110]$ and $[100]$ in ferrite and cementite, respectively.
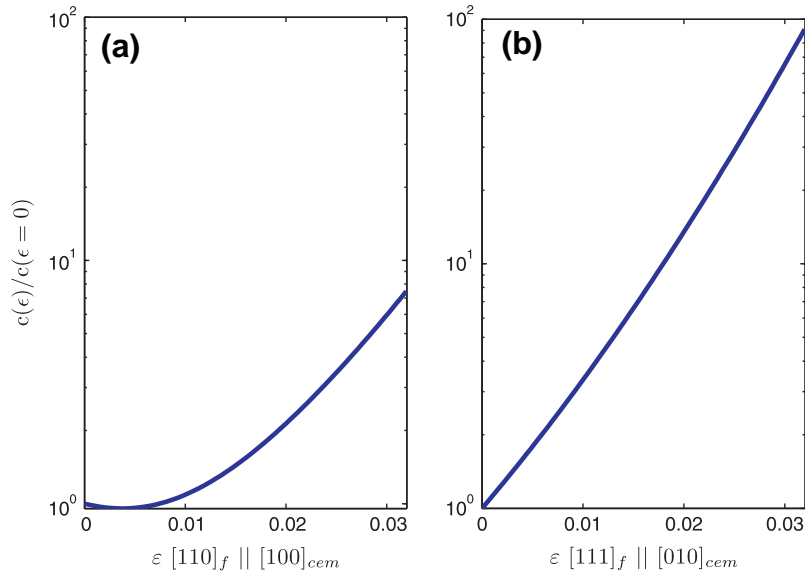
Fig. 11. Relative C concentration in ferrite particles within the pearlitic microstructures at 300 K as a function of applied strain along (a) $[1\,1\,0]_f$ and (b) $[1\,1\,1]_f$ in ferrite and the corresponding directions in cementite, as given by the Bagaryatsky orientation relationship under iso-stress boundary conditions (Reuss limit).

determine the equilibrium C concentration within the ferrite layers using Eqs. (4) and (5), as described above. Finally, the macroscopic (external) strain state (ε_{tot}) of the pearlite sample for a given stress state was found using:

$$\varepsilon_{tot} = \varepsilon_f v_f + \varepsilon_{cem} v_{cem}, \tag{6}$$

where v_f and v_{cem} are volume fractions of ferrite and cementite, respectively, which were assumed to be 0.9 for ferrite and 0.1 for cementite, given the eutectoid composition of pearlite.

A comparison of the equilibrium C concentration in ferrite under iso-strain and iso-stress conditions reveals a somewhat increased solubility in the Reuss limit. This difference stems from the independent deformation of the ferrite and cementite phases in the iso-stress model. Hence, due to its higher stiffness the cementite particles will deform less than the ferrite particles, resulting in a less pronounced destabilisation of the vacancy in cementite and a more pronounced stabilization of C in the ferrite.

Finally, we consider the maximum equilibrium C concentration in ferrite particles within the pearlitic microstructure as a function of temperature (Fig. 12), which suggests that the strain-induced enhancement is fairly temperature independent in both the iso-strain and the iso-stress limit.

4.3. Increase in interfacial area

An additional thermodynamic driving force for the dissolution of cementite is given by the huge increase in interfacial area between the cementite and ferrite layers during the wire-drawing process [1,3]. Taking into account the increase in the free energy due to the presence of the interface (of area S^α), the free energy, F^α, of a phase α containing n^α atoms is given by:

$$F^\alpha = n^\alpha F_n^\alpha + \gamma S^\alpha, \tag{7}$$

where F_n^α is the free energy per atom of the α phase and γ is the interfacial tension. Since in a steel of eutectoid composition the ferrite layers are roughly nine times thicker than the cementite layers [4], the surface term in Eq. (7) is more important in the case of the cementite layers than for the ferrite layers. Using Eq. (7) and assuming an exponential increase in the interfacial area with increasing strain and a strain-independent interfacial tension, Sauvage et al. predicted a substantial destabilization of the cementite layers [4]. In particular, under a true strain of $\varepsilon = 3$, an increase in the C concentration in ferrite by 4 orders of magnitude was predicted [4]. However, according to this analysis the cementite layer should eventually dissolve completely, as the applied strain is increased. This is in conflict with experimental evidence, which clearly reveals the presence of C-rich phases even under a true strain of 5 [5], suggesting that the assumption of a strain-independent interfacial tension is not capturing this destabilizing effect correctly.

In solids, the interfacial energy (γ) is proportional to the interfacial tension (S) via:

$$S = \gamma + \frac{\delta\gamma}{\delta\varepsilon}, \tag{8}$$

where ε is the surface strain [41]. The Gibbs–Thomson equation suggests that the interfacial tension at the ferrite–cementite interface can be estimated by:

$$S_{cem/f} R = P_{cem} - P_f, \tag{9}$$

where R is the curvature of the interface, and P_{cem} and P_f are the pressures in the bulk cementite and ferrite phases, respectively. The large lattice misfit between cementite and ferrite in the given crystallographic orientational relationship [42] provides a substantial driving force for
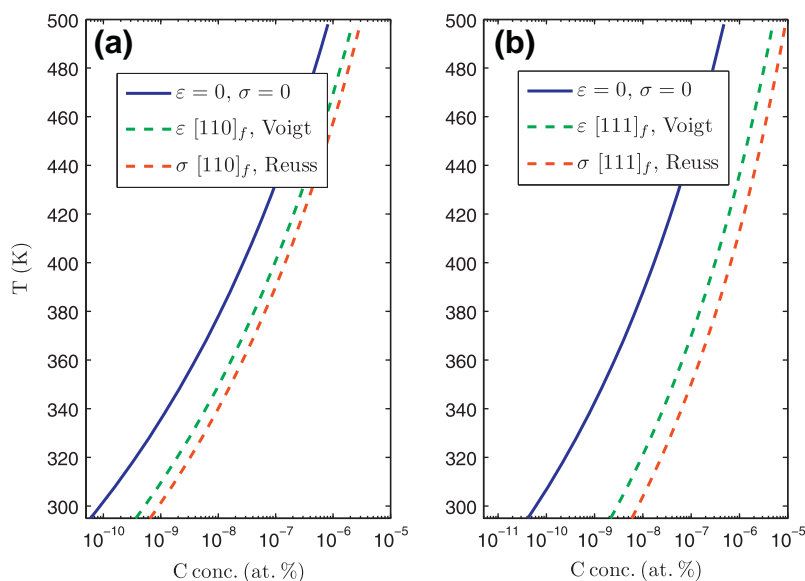
Fig. 12. Equilibrium carbon concentration in deformed and undeformed ferrite layers within pearlitic structures of eutectic composition, as a function of temperature. In the Voigt limit an applied strain of 3% was assumed, while in the Reuss limit an external stress of 6 GPa was considered.

the creation of misfit dislocations in the interface between them in the undeformed pearlitic structure. Experimentally observed dislocation nucleation in the interface during deformation [5] suggests that the ferrite–cementite interface can be considered as a incoherent interface. In undeformed pearlite specimens the cementite lamellae are fairly straight and start to rotate around the wire axis during the initial stages of deformation, resulting in a curvy microstructure and metallographic texture (curling) [3,5,7,14]. Moreover, the cementite particles are fragmented into small uniaxial grains of few nanometers, a behaviour that is attributed to the substantial mismatch in the curvature between the two phases. After the majority of pearlite colonies are aligned along the wire direction ($\varepsilon > 2$), the rate of texture evolution decreases to nearly zero [3], which suggests that the lamellae's curvatures (R) do not change significantly during further-straining.

As shown in Fig. 10, the applied strains considered in this study induce significantly larger stresses in cementite than in ferrite, suggesting that cementite is stiffer along the corresponding directions. According to Eq. (9), the different stiffness of the two materials will give rise to an increased interfacial tension with increasing external strains. However, Fig. 10 also reveals that the introduction of an interstitial C does not significantly alter the stiffness of the ferrite matrix, while cementite is softened by the presence of a C vacancy, which, according to Eq. (9), will result in a reduction in the interfacial tension by $\approx 25\%$. A qualitatively similar behaviour was also observed in the case of an applied strain along [110] in ferrite and the corresponding [100] direction in cementite (not shown in Fig. 10). The fact that cementite-like particles persist even under a true strain of 5 despite their unfavourable surface-to-volume ratio is therefore attributed to their reduced

interfacial tension resulting from the formation of C vacancies. In other words, in addition to the energetic driving force for the transfer of C from cementite to ferrite layers, there is also an elastic driving force for this rearrangement.

From a thermodynamic point of view, the C concentration in ferritic layers of severely plastically deformed pearlitic wires is thus controlled by various effects: the strain-induced stabilization of C interstitials in ferrite layers; the dissolution of cementite layers due to their unfavourable surface-to-volume ratio; and finally the interfacial tension between the two phases, which was shown to also depend on the distribution of C across the interface. Given the highly non-equilibrium conditions of the wire-drawing experiment, additional, kinetically controlled mechanisms are likely to give rise to a further accumulation of C within the ferrite matrix. However, it is noteworthy that even a purely thermodynamic analysis of the wire-drawing process can account for a significant accumulation of C within the ferrite layers of the pearlitic microstructure far beyond the values assumed by conventional thermodynamic estimates.

5. Conclusion

DFT calculations were performed to investigate the thermodynamic driving force for the experimentally observed accumulation of C in ferritic layers of severely plastically deformed pearlitic wires. A considerable strain-induced stabilization of interstitial C atoms in ferrite was found. Hence under an applied strain of 3% along $[111]_f$ and $[110]_f$, the equilibrium C concentration in ferrite is increased by more than two orders of magnitude. However, C vacancies in cementite were found to be destabilized under corresponding strain conditions, resulting in only a moderate reduction of the overall reaction energetics for

the strain-induced transfer of C from cementite to ferrite. In particular, under an applied strain of 3% along $[1\,1\,0]_f$ and $[1\,1\,1]_f$ ($[1\,0\,0]_{cem}$ and $[0\,1\,0]_{cem}$), an increase in the C concentration in ferrite by one and two orders of magnitude respectively was predicted, under the iso-strain condition (Voigt limit). Under iso-stress conditions (Reuss limit) a slightly more pronounced accumulation of C in the ferrite layers of the pearlitic microstructure was predicted. While this constitutes a significant increase in the C solubility, it does not explain the experimentally observed increase by nine orders of magnitude in the C concentration within the ferritic matrix.

Our simulations suggest an additional, elastic driving force for the experimentally observed accumulation of C atoms in the ferrite layers. In particular, the elastic mismatch between cementite and ferrite was found to be reduced by the transfer of C atoms from cementite to ferrite, resulting in a reduced interfacial tension, as given by Eq. (8). A further driving force for the dissolution of C atoms within the ferrite matrix will be the unfavourable surface-to-volume ratio of the cementite particles, which will induce their progressive dissolution as the pearlitic wire is extended. However, the fact that the thermodynamic driving forces can only partially explain the solubility increase implies that the final distribution of C within the plastically deformed pearlitic wires may well also depend on non-equilibrium processes such as a dislocation-based transfer of the C atoms from the cementite–ferrite interface into the ferrite layers and the subsequent trapping of C at lattice defects.

References

[1] Raabe D, Choi P, Li Y, Kostka A, Sauvage X, Lecouturier F, et al. Metallic composites processed via extreme deformation: toward the limits of strength in bulk materials. MRS Bull 2010;35:928–87.

[2] Zhang X, Godfrey A, Huang X, Hansen N, Liu Q. Microstructure and strengthening mechanisms in cold-drawn pearlitic steel wire. Acta Mater.

[3] Zelin M. Microstructure evolution in pearlitic steels during wire drawing. Acta Mater 2002;50(17):4431–47.

[4] Sauvage X, Copreaux J, Danoix F, Blavette D. Atomic-scale observation and modelling of cementite dissolution in heavily deformed pearlitic steels. Philos Mag A 2000;80(4):781–96.

[5] Li Y, Choi P, Borchers C, Westerkamp S, Goto S, Raabe D, et al. Atomic-scale mechanisms of deformation-induced cementite decomposition in pearlite. Acta Mater 2011;59:3965–77.

[6] Li Y, Choi P, Borchers C, Chen Y, Goto S, Raabe D, et al. Atom probe tomography characterization of heavily cold drawn pearlitic steel wire. Ultramicroscopy 2011;111(6):628–32.

[7] Goto S, Kirchheim R, Al-Kassab T, Borchers C. Application of cold drawn lamellar microstructure for developing ultra-high strength wires. Trans Nonferr Metals Soc China 2007;17(6):1129–38.

[8] Embury J, Fisher R. The structure and properties of drawn pearlite. Acta Metall 1966;14(2):147–59.

[9] Embury J, Hirth J. On dislocation storage and the mechanical response of fine scale microstructures. Acta Metall Mater 1994;42(6):2051–6.

[10] Takahashi J, Tarui T, Kawakami K. Three-dimensional atom probe analysis of heavily drawn steel wires by probing perpendicular to the pearlitic lamellae. Ultramicroscopy 2009;109(2):193–9.

[11] Sauvage X, Lefebvre W, Genevois C, Ohsaki S, Hono K. Complementary use of transmission electron microscopy and atom probe tomography for the investigation of steels nanostructured by severe plastic deformation. Scripta Mater 2009;60(12):1056–61.

[12] Pippan F, Sturm R, Kauffmann S, Scheu F, Dehm C, Wetscher G. Metall Mater Trans A: Phys Metall Mater Sci 2006;37(6):1963–8 [cited by (since 1996) 21].

[13] Hono K, Ohnuma M, Murayama M, Nishida S, Yoshie A, Takahashi T. Cementite decomposition in heavily drawn pearlite steel wire. Scripta Mater 2001;44(6):977–83.

[14] Borchers C, Al-Kassab T, Goto S, Kirchheim R. Partially amorphous nanocomposite obtained from heavily deformed pearlitic steel. Mater Sci Eng A 2009;502(1–2):131–8.

[15] Langford G. Deformation of pearlite. Metall Mater Trans A 1977;8(6):861–75.

[16] Ivanisenko Y, Sauvage X, MacLaren I, Fecht HJ. Nanostructuring and dissolution of cementite in pearlitic steels during severe plastic deformation. In: Hahn H, Sidorenko A, Tiginyanu I, editors. Nanoscale phenomena, nanoscience and technology. Berlin (Heidelberg): Springer; 2009. p. 41–55.

[17] Hinchliffe C, Smith G. Strain aging of pearlitic steel wire during postdrawing heat treatments. Mater Sci Technol 2001;17(2):148–54.

[18] Yamada Y. Static strain aging of eutectoid carbon steel wires. Trans Iron Steel Inst Jpn 1976;16(8):417–26.

[19] Watté P, Humbeeck J, Aernoudt E, Lefever I. Strain aging in heavily drawn eutectoid steel wires. Scripta Mater 1996;34(1):89–95.

[20] Xiao L, Fan Z, Jinxiu Z, Mingxing Z, Mokuang K, Zhenqi G. Lattice-parameter variation with carbon content of martensite. I. X-ray-diffraction experimental study. Phys Rev B 1995;52:9970–8.

[21] Udyansky A, von Pezold J, Bugaev VN, Friák M, Neugebauer J. Interplay between long-range elastic and short-range chemical interactions in Fe–C martensite formation. Phys Rev B 2009;79:224112.

[22] Udyansky A, von Pezold J, Dick A, Neugebauer J. Orientational ordering of interstitial atoms and martensite formation in dilute Fe-based solid solutions. Phys Rev B 2011;83:184112.

[23] Hristova E, Janisch R, Drautz R, Hartmaier A. Solubility of carbon in alpha-iron under volumetric strain and close to the i pound sterling 5 (310)[001] grain boundary: comparison of dft and empirical potential methods. Comput Mater Sci 2011;50(3):1088–96.

[24] Huang L, Skorodumova N, Belonoshko A, Johansson B, Ahuja R. Carbon in iron phases under high pressure. Geophys Res Lett 2005;32(21):21314.

[25] Zhou D, Shiflet G. Ferrite: cementite crystallography in pearlite. Metall Mater Trans A 1992;23(4):1259–69.

[26] Isaichev IV. Orientation of cementite in tempered carbon steel. Zh Sakharnoi Promst 1947;17:835–8.

[27] Petch N. The orientation relationships between cementite and α-iron. Acta Crystallogr 1953;6(1):96.

[28] Fasiska E, Jeffrey G. On the cementite structure. Acta Crystallogr 1965;19(3):463–71.

[29] Hohenberg P, Kohn W. Inhomogeneous electron gas. Phys Rev 1964;136(3B):B864.

[30] Kohn W, Sham L, et al. Self-consistent equations including exchange and correlation effects. Phys Rev 1965;140(4A):1133–8.

[31] Blöchl PE. Projector augmented-wave method. Phys Rev B 1994;50:17953–79.

[32] Kresse G, Furthmüller J. Efficiency of ab-initio total energy calculations for metals and semiconductors using a plane-wave basis set. Comput Mater Sci 1996;6(1):15–50.

[33] Perdew J, Burke K, Ernzerhof M. Generalized gradient approximation made simple. Phys Rev Lett 1996;77(18):3865–8.

[34] Monkhorst HJ, Pack JD. Special points for Brillouin-zone integrations. Phys Rev B 1976;13:5188–92.

[35] Methfessel M, Paxton AT. High-precision sampling for Brillouin-zone integration in metals. Phys Rev B 1989;40:3616–21.

[36] Moroni E, Kresse G, Hafner J, Furthmüller J. Ultrasoft pseudopotentials applied to magnetic Fe, Co, and Ni: from atoms to solids. Phys Rev B 1997;56(24):15629.

[37] Dick A, Körmann F, Hickel T, Neugebauer J. Ab initio based determination of thermodynamic properties of cementite including vibronic, magnetic, and electronic excitations. Phys Rev B 2011;84:125101.

[38] Wood I, Vocadlo L, Knight K, Dobson D, Marshall W, Price G, et al. Thermal expansion and crystal structure of cementite, Fe_3C, between 4 and 600 K determined by time-of-flight neutron powder diffraction. J Appl Crystallogr 2004;37(1):82–90.

[39] Harris B. Engineering composite materials. UK: Institute of Metals; 1986.

[40] Li Y, Choi P, Goto S, Borchers C, Raabe D, Kirchheim R. Evolution of strength and microstructure during annealing of heavily cold-drawn 6.3 GPa hypereutectoid pearlitic steel wire. Acta Mater 2012;60(9):4005–16.

[41] Fischer F, Waitz T, Vollath D, Simha N. On the role of surface energy and surface stress in phase-transforming nanoparticles. Prog Mater Sci 2008;53(3):481–527.

[42] Andrews K. The structure of cementite and its relation to ferrite and epsilon carbide - II. Acta Metall 1964;12(8):921–9.

Chemical gradients across phase boundaries between martensite and austenite in steel studied by atom probe tomography and simulation

O. Dmitrieva [a], D. Ponge [a], G. Inden [a], J. Millán [a], P. Choi [a], J. Sietsma [b], D. Raabe [a],*

[a] *Max-Planck-Institut für Eisenforschung, Max-Planck-Str. 1, 40237 Düsseldorf, Germany*
[b] *Delft University of Technology, Faculty 3mE, Dept. MSE, 2628 CD Delft, The Netherlands*

Abstract

Partitioning at phase boundaries of complex steels is important for their properties. We present atom probe tomography results across martensite/austenite interfaces in a precipitation-hardened maraging-TRIP steel (12.2 Mn, 1.9 Ni, 0.6 Mo, 1.2 Ti, 0.3 Al; at.%). The system reveals compositional changes at the phase boundaries: Mn and Ni are enriched while Ti, Al, Mo and Fe are depleted. More specific, we observe up to 27 at.% Mn in a 20 nm layer at the phase boundary. This is explained by the large difference in diffusivity between martensite and austenite. The high diffusivity in martensite leads to a Mn flux towards the retained austenite. The low diffusivity in the austenite does not allow accommodation of this flux. Consequently, the austenite grows with a Mn composition given by local equilibrium. The interpretation is based on DICTRA and mixed-mode diffusion calculations (using a finite interface mobility).
© 2010 Acta Materialia Inc. Published by Elsevier Ltd. All rights reserved.

Keywords: Precipitation hardening; High-strength steels; TRIP; Aging; Atom probe tomography

1. Introduction

Mn is among the most important alloying elements for the design of advanced high-strength steels, as it affects the stabilization of the austenite, the stacking fault energy and the transformation kinetics [1–11]. Besides these global mechanisms which are exploited particularly in designing steels with transformation-induced plasticity (TRIP) and twinning-induced plasticity (TWIP) effects, Mn has very low diffusion rates in the austenite and a high segregation or respectively partitioning tendency at interfaces. This context makes Mn (as well as the other elements discussed in this paper) a very interesting candidate for an atomic-scale study of compositional changes across austenite/martensite interfaces.

The specific material studied in this work is a precipitation-hardened alloy that we refer to as maraging-TRIP steel. It was developed by combining the TRIP mechanism with the maraging (i.e. martensite aging) effect [12,13]. The TRIP effect exploits the deformation-stimulated transformation of metastable retained austenite into martensite and the resulting plasticity required to accommodate the transformation misfit [1–7]. The maraging effect uses the hardening of the heavily strained martensite through the formation of nanosized intermetallic precipitates during aging heat treatment. The maraging-TRIP steels used in this work reveal the surprising property that both strength and total elongation increase upon aging, reaching an ultimate tensile strength of nearly 1.3 GPa at an elongation above 20% [12–14].

The studied alloy contains 12.2 at.% Mn, low carbon content (0.05 at.%) and minor additions of Ni, Ti, Al and Mo. Its microstructure after aging is characterized by the presence of up to 15–20 vol.% austenite, a fine martensite matrix, and dispersed nanoscaled Ni–Al–Mn-enriched zones [12–14]. Besides the increase in strength, a simultaneous increase of ductility was found upon aging. This effect is interpreted in terms of sluggish reaustenitization during aging and the effect of tempering of the as-quenched

martensite [14]. Partial retransformation into austenite (besides the existing retained austenite) by a reconstructive mechanism involving Mn partitioning might be responsible for this process.

In order to elucidate this transformation phenomenon, particularly the role of Mn, we focus in this work on the analysis of nanoscale elemental diffusion gradients across abutting martensite/retained austenite phase areas. Atom probe tomography (APT) is a characterization technique that provides three-dimensional elemental mapping with nearly atomic resolution and gives information on the topology of interfaces and local chemical gradients [15–27]. We conducted APT using an advanced local electrode atom probe device (Imago LEAP 3000X HR). Both the two phases (austenite, martensite) and the interfaces between them were chemically analyzed at the atomic scale. Additionally, statistical thermodynamic and kinetic calculations were conducted for the given initial and boundary values using Thermo-Calc [28,29] in conjunction with the kinetic simulation software DICTRA [30–32] and with a mixed-mode kinetic approach that considers finite interface mobility [33,34].

2. Experimental

The investigated maraging-TRIP steel with a composition of 12.2 Mn, 1.9 Ni, 0.6 Mo, 1.2 Ti, 0.1 Si, 0.3 Al and 0.05 C (at.%) was melted and cast in a vacuum induction furnace. Before final age hardening, a solution treatment was performed in Ar atmosphere at 1050 °C for 0.5 h followed by water quenching. This led to a microstructure consisting of martensite and retained austenite. Final aging was conducted for 48 h at 450 °C. After aging the sample was quenched in water. Details of the alloy preparation have been published elsewhere [12–14].

APT samples were prepared by electrochemical polishing and subsequent sharpening using a focused ion beam device. Pulsed-laser APT was performed using a local electrode atom probe (LEAP™ 3000X HR, Imago Scientific Instruments) tomograph at a specimen temperature of 54 K. An ultrafast pulsed laser of $\sim$10 ps pulse width and 532 nm wavelength was applied at a frequency of 250 kHz. The laser pulse energy was set to 0.4 nJ. The detection rate (target evaporation rate) amounted to 5 atoms per 1000 pulses. Data analysis was performed using the IVAS® software from Imago Scientific Instruments. The specific APT data set analyzed in this work contains about 70 million ions. We used an evaporation field constant of 26 V nm^{-1} for the atomic reconstruction.

Phase fractions and the elemental compositions in thermodynamic equilibrium were calculated using the software Thermo-Calc [28]. The software DICTRA [30–32] and a mixed-mode kinetic approach including finite interface mobility [33,34] were applied to simulate diffusion-controlled phase transformations. The simulations were performed using the thermodynamic database TCFE6 [29] and the mobility database MOB2.

3. Results

3.1. Analysis of the 3-D atom probe reconstruction

3.1.1. Manganese distribution

Fig. 1a gives a microstructure overview of the maraging-TRIP steel after quenching and subsequent aging (48 h at 450 °C). The upper micrograph is an electron backscatter diffraction (EBSD) image where the cubic martensite is plotted green and the retained austenite red (the retained austenite was already present in the as-quenched state before aging [12–14]). The middle image shows a transmission electron microscopy (TEM) micrograph with precipitate-containing martensite and precipitate-free austenite. The bottom image shows an APT reproduction which includes both martensitic and austenitic zones. Ni atoms are shown in cyan and Mn atoms in blue. The yellow isosurfaces indicate 18 at.% Mn. Note that the three images reveal the hierarchy of the microstructure but the individual images were not taken at precisely the positions indicated. Fig. 1b gives a local overview of the distribution of the Ni and Mn atoms in the center of the APT data set presented in Fig. 1a. For clarity, only a longitudinal section of 20 nm thickness is shown, in which only 7.8% of all detected Ni (cyan) and 1.5% of all Mn (dark blue) atoms are displayed. The whole analysis volume is about 4×10^5 nm^3. Fig. 1a and b show three main zones that are separated by inclined plate-like Mn accumulations. Ni-rich nanoprecipitates are dispersed in the left- and right-hand areas. Besides the Ni atoms, higher amounts of Al, Mn, and Ti were also detected in these clusters (Table 1). In the center part between the Mn-enriched plates, no precipitates appear. This observation strongly suggests that this zone corresponds to austenite, whereas the abutting areas containing precipitates are martensitic. Correlative TEM investigations conducted on this alloy in the same aging state (48 h, 450 °C) support the suggestion that the nanoparticles that are enriched in Ni, Al and Mn formed in the martensitic microstructure while the retained austenite (total volume fraction about 15–20 vol.%) was precipitate-free [13,14] (Fig. 1a). From these observations we conclude that the present volume probed by APT contains an austenitic grain enclosed between two martensitic grains. Quantitative chemical analysis of the interfaces between austenite and martensite was performed using 1-D concentration profiles computed over the region of interest (transparent cylindrical units) (Fig. 2a). We calculated the Mn content averaged over the 0.5 nm thick cross-sections of the cylinders at a profile step size of 0.5 nm. For both interfaces, a strong increase in the Mn content up to 27 at.% was observed (Fig. 2b). Away from the interface, the content of Mn within the austenite amounts to about 12 at.% which is close to the average chemical composition of the alloy. Within the bulk martensite the Mn content amounts to about 10 at.%. Mn depletion in the martensite down to 6 at.% was observed close to the interface.
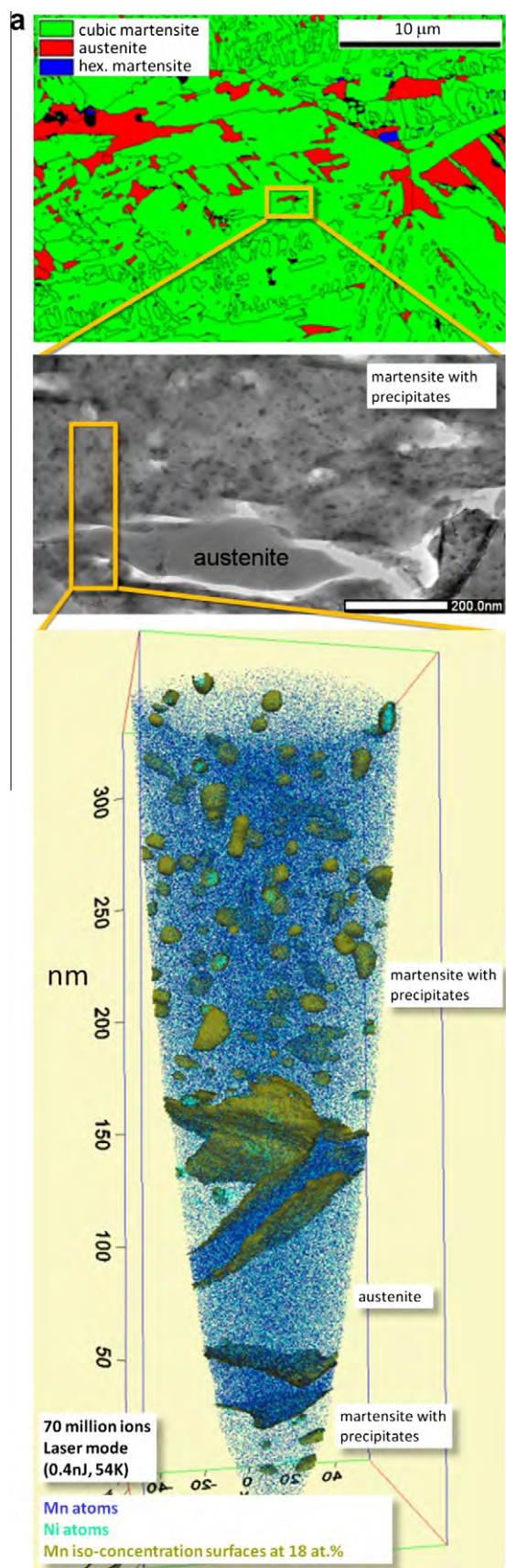
In order to exclude the contribution of the precipitates from the chemical profile within the martensitic area, we separately measured the 1-D concentration profiles within the martensitic matrix after removing the precipitate zones from the analysis volume (described in detail below). The reason for this procedure is that the martensitic area is in itself a two-phase region consisting of martensite and precipitates. Hence, we aim with this method at the separation of the martensite elemental composition and the precipitate elemental composition. These two corrected profiles, containing only the martensite composition, are included in Fig. 2b on the left-hand side in the martensitic area marked "M". The curves are separated from the profile across the interface and in the austenite ("A").

3.1.2. Distribution of other alloying elements

Fig. 3 shows the concentration profiles for the other alloying elements across one of the martensite/austenite phase boundary zones. The area selected is indicated by "Mn layer 2" in Fig. 2a. In addition to Mn (which is studied here in more detail owing to its relevance for high-strength steels), all other elements also reveal a strong partitioning between the two phases. While Mn is enriched by about 2.1 times within the interface boundary layer relative to its average content in the alloy, Ni is accumulated 1.2 times in the same zone. All other elements are depleted in the interface zone: Ti decays by a factor of about 6.9 times relative to the average content, Al by a factor of 6.6, Mo 2.0 and Fe 1.2. Another important observation is the large chemical width of the phase boundary zone: the enrichment zone associated with the austenite/martensite interface extends over a length of about 20 nm normal to the boundary segment studied.

3.1.3. Chemical analysis of the nanoparticles and of the alloy matrix

The nanoparticles detected in the martensite were analyzed using a cluster search algorithm implemented in the

Fig. 1. (a) Microstructure overview of the maraging-TRIP steel after quenching and subsequent aging (48 h at 450 °C). The upper micrograph is an EBSD image where the cubic martensite is plotted green and the retained austenite red (the retained austenite was already present in the as-quenched state before aging). The middle image shows a TEM micrograph with precipitate-containing martensite and precipitate-free austenite. The bottom image shows an APT reproduction which includes both martensitic and austenitic zones. Ni atoms are given in cyan and Mn atoms in blue. The yellow isosurfaces indicate 18 at.% Mn. Note that the three images correctly reveal the hierarchy of the microstructure but the individual images were not taken at precisely the positions indicated. (b) 20 nm thick middle layer slice through the APT reconstruction of the maraging-TRIP steel shown in (a). Ni atoms (cyan symbols) are accumulated in precipitates in the martensitic grains (left- and right-hand side). The precipitate-free austenite (right-hand center) is bordered by plate-like zones that are characterized by strong Mn enrichment (blue symbols). Red dotted lines illustrate the suggested crystallographic positions of the phase boundaries between martensite and austenite.
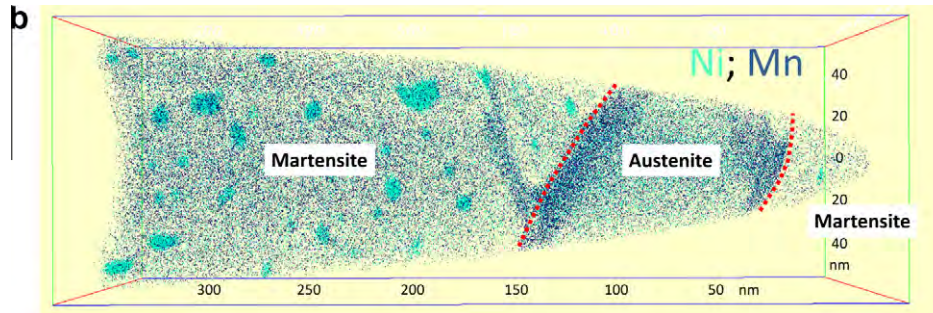
Fig. 1 (*continued*)

Table 1

(Experimental results) Elemental composition of the alloy measured globally on the as-cast sample using wet chemical analysis (total content melt) and obtained locally from the APT measurement on the specimen volume containing a martensite/austenite phase boundary of 450 °C/48 h aged steel (total content APT; martensite; austenite). Enrichment factors are calculated as the relation between the elemental content within the particles to the total content of element in the alloy.

Chemical content, at.%	Total content (melt)	Total content (in APT)	Martensite				Austenite
			Total	Matrix	Particles	Enrichment factor	
Fe	83.71	83.21	84.38	86.82	40.32	0.48	83.53
Mn	12.19	12.34	11.10	10.29	26.07	2.35	12.17
Ni	1.90	2.26	2.32	0.99	25.79	11.12	2.01
Ti	1.17	1.10	1.09	0.98	3.23	2.96	1.14
Mo	0.58	0.60	0.60	0.62	0.27	0.45	0.60
Al	0.31	0.33	0.34	0.14	4.08	12.0	0.38
Si	0.10	0.16	0.15	0.14	0.24	1.6	0.16
C	0.046	0.006	0.001	0.001	0		0.006
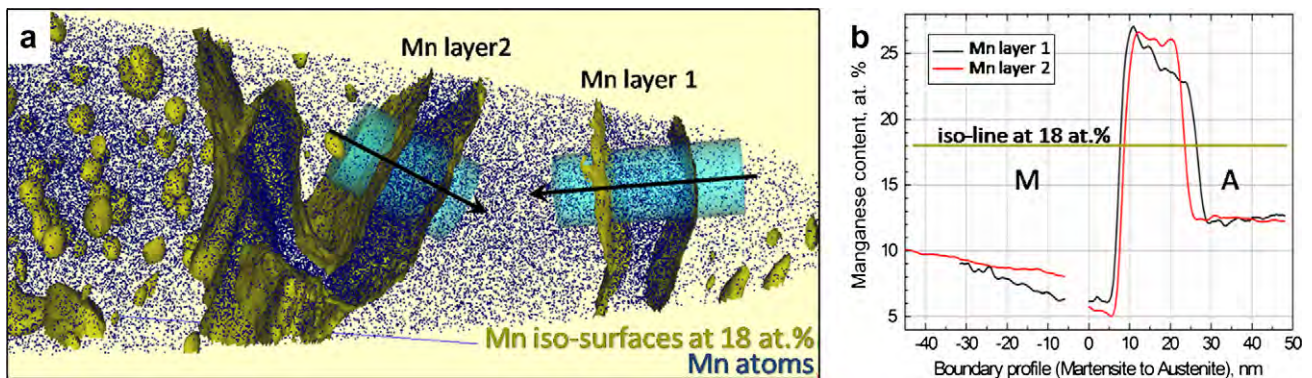
Fig. 2. Quantitative chemical analysis of the interface regions between martensite and austenite (APT results). (a) Atomic map section showing both phase boundaries. Isoconcentration surfaces for the chemical distribution of Mn atoms (blue) were plotted at 18 at.% (yellow). 1-D profiles along the cylindrical units (cyan) provide chemical gradients of elements across the phase boundaries. (b) Gradients in Mn content across the phase boundaries (martensite to austenite).

IVAS® software. For cluster identification, the following parameters as identified by the optimization procedure performed within the cluster search algorithm were used: $d_{max} = 0.6$ nm (maximal distance between the solute atoms belonging to a cluster), $N_{min} = 50$ (minimal number of solute atoms in the cluster), $L = 0.57$ nm (envelope distance: all non-solute ions within a distance L of solute ions are included in the cluster), $d_e = 0.55$ nm (erosion distance: all clustered non-solute ions within a spacing d_e of any ion outside of its assigned cluster are removed from the particle). The cluster search was conducted for the distribution of the Ni atoms that are enriched in the particles. The

chemical composition of the clusters is summarized in Table 1. The calculation of the enrichment factors that were determined as a relation between the content within the particles relative to the total content of the same elements in the entire alloy reveals a strong precipitation character of Ni and Al atoms within the clusters. Enrichment in Mn and Ti was also detected in the particles. For estimating the chemical composition of the surrounding matrix (without the precipitates), the detected clusters were removed from the overall reconstruction, and the composition of the residual matrix volume was calculated again. For this purpose, different cluster search parameters were
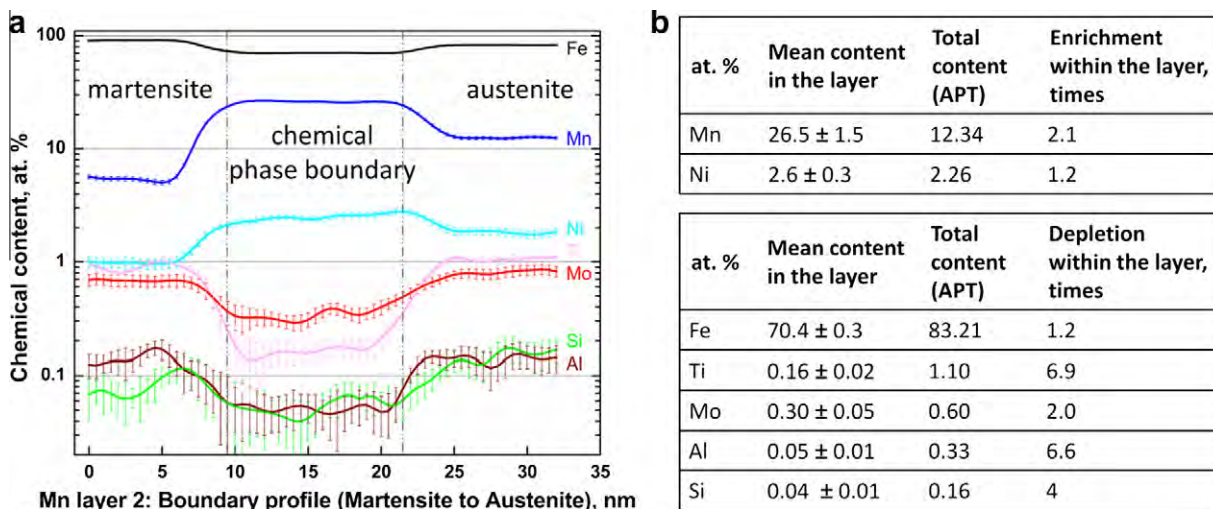
Fig. 3. Experimental APT results. (a) Concentration profiles for all elements across one of the martensite/austenite phase boundaries (see interface referred to as "Mn layer 2" in Fig. 2a). (b) Quantitative characterization of the enrichment or depletion of the elements within the chemical phase boundary.
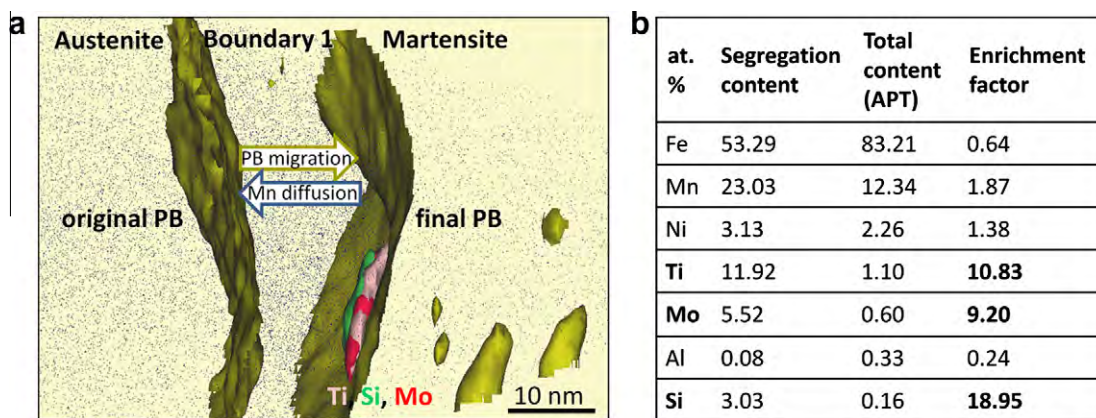
Fig. 4. Compositional changes in the austenite/martensite interface region (APT results). (a) Atomic map section showing a phase boundary between austenite (left) and martensite (right). Isoconcentration surfaces plotted at 18 at.% Mn (dark yellow) correspond to the highest Mn gradient and indicates the positions of the original and the final phase boundaries (PB) (see text). The compositional changes at the final PB are revealed by plotting isoconcentration surfaces for Ti (at 8 at.%), Mo (at 5 at.%), and Si (at 3 at.%). (b) Chemical composition of the Ti–Mo–Si-rich partitioning estimated from the APT data.

used ($d_{max} = 1.0$ nm, $N_{min} = 50$, $L = 0.97$ nm, $d_e = 0.95$ nm) which allow inclusion of more material in the clusters and ensure that after exclusion of the clusters no residual material remains. The composition of the matrix without the particles is presented in Table 1.

3.1.4. Observation of compositional changes within the martensite/austenite interface region

By computing the isoconcentration surfaces for all solute elements from the experimental data we detected changes in composition of Mo, Ti and Si in the martensite/austenite interface region. Fig. 4a shows isosurfaces for Mo, Ti and Si concentrations of 5, 8 and 3 at.%, respectively. The position of this region overlaps with the position of the isoconcentration surface plotted at 18 at.% Mn and, more specifically, corresponds to the range of the highest Mn gradient. A similar region with nearly the

same content and element distribution was also observed at the other martensite/austenite interface (not shown in Fig. 4a). The average chemical composition within the region is summarized in the table in Fig. 4b. The enrichment factors reveal strong compositional increase of Ti, Mo and Si, and strong depletion of Al. The relative concentrations of Fe, Ti and Mo within that region are 75:17:8, suggesting the formation of a Laves phase, which according to Thermo-Calc should be formed at a composition of Fe 67 at.%, Ti 23 at.%, and Mo 10 at.%.

3.2. Thermodynamic calculations

3.2.1. Prediction of the phase equilibrium composition

Using Thermo-Calc, the equilibrium compositions of stable phases at 450 °C were calculated taking into account the total nominal composition of the alloy and all possible

Table 2
Equilibrium phases at 450 °C in the investigated maraging-TRIP steel as obtained by Thermo-Calc calculations quantified in terms of molar fractions (TCFE6 database).

Phase	Mole fraction	Fe	Mn	Ni	Ti	Mo	Al	Si	C
bcc	0.576	95.972	3.064	0.098	0.165	0.113	0.494	0.094	–
fcc	0.377	67.251	27.569	4.887	0.053	0.077	0.041	0.122	–
Laves	0.046	65.911	0.763	–	22.321	11.005	–	–	–
TiC	0.001	–	–	–	54.046	–	–	–	45.954

competing phases available in the database [28,29]. The results of the Gibbs energy minimization technique predicts four phases in thermodynamic equilibrium: body-centered cubic (bcc: ferrite/martensite), face-centered cubic (fcc: austenite), TiC and a Laves phase. The calculated molar fractions for each phase and their chemical compositions are listed in Table 2. It is important to point out that such calculation does not predict the presence of the nanosized particles due to the limited availability of thermodynamic data related to various other possible intermetallic phases in complex maraging steels. At a temperature of 450 °C, a Mn content of about 26.7 and 3.3 at.% is expected in the retained austenite and in the ferrite (martensite), respectively.

3.2.2. Diffusion simulations using DICTRA

For simulation of the kinetic behavior in the vicinity of the martensite/austenite interface, linear cell geometry is appropriate [30]. The kinetic effects to be studied are confined to very small spatial ranges. Within this scale the interfaces are planar in shape and their movement is vertical to the plane. The size of the cell was chosen as 20 μm (see Fig. 5a). The cell was divided into two regions, one corresponding to ferrite, the other to austenite. The space in each region is discretized as a linear grid. The distribution of the grid points is chosen with a high density close to the interface. The grid is defined in terms of geometric series. The compositions of ferrite and austenite were taken according to the values determined via the APT characterization for the austenitic and martensitic matrices, respectively. In the martensitic matrix we detected a slight Mn depletion down to 10.3 at.%. This can be attributed to the formation of nanoprecipitates. Within martensite, a large number of lattice defects, particularly dislocations, enhance the atomic diffusion in this phase. Our previous TEM-based studies on this material [12,13] revealed that

most of the nanoprecipitates were indeed associated with dislocations, which supports the assumption that the pipe mechanism may strongly assist diffusion within the martensite. In order to take into account the variation of composition in the ferrite due to the precipitation of particles, an average composition was used for the ferrite phase (see Fig. 5b). Martensite is not included as a separate phase in the thermodynamic and kinetic databases as the thermodynamic properties of martensite are very much the same as those of ferrite. Therefore, in the thermodynamic calculations, martensite is represented as ferrite. The kinetic parameters, however, may deviate between the two phases owing to the defect structure and distortion of the martensite. To date, no detailed information is available on the effect of these conditions on possible changes in the kinetic parameters between ferrite and martensite.

The size of the cell is fixed during the simulation (20 μm), whereas the interface between the two regions is mobile. The conditions at the moving interface are determined by the local equilibrium assumption, i.e. the chemical potentials of all diffusing elements assume the same value in ferrite and austenite. The value of the potentials is controlled by the mass balance condition. Diffusion of Mn, Mo, Ni, Si and Ti atoms was considered in the calculation. The simulation was performed for an aging temperature 450 °C and stopped at 180,000 s (50 h).

The composition profile of Mn between ferrite and austenite after an annealing time of 50 h at 450 °C is presented in Fig. 6. The interface has moved towards the ferrite side, leaving behind an austenite layer with drastically changed composition. This result is in qualitative agreement with the experimental data presented in Fig. 2b. However, the width of the predicted Mn-rich interfacial layer is too small and, correspondingly, the extent of the Mn depletion zone in ferrite is also relatively small. This discrepancy indicates

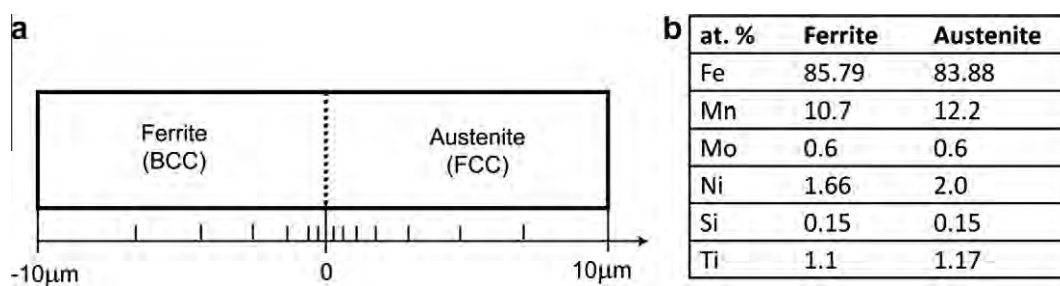| b at. %	Ferrite	Austenite
Fe	85.79	83.88
Mn	10.7	12.2
Mo	0.6	0.6
Ni	1.66	2.0
Si	0.15	0.15
Ti	1.1	1.17

Fig. 5. (a) Linear cell model set-up with ferrite and austenite as used in the DICTRA simulation. The spatial grid is defined in terms of a geometric series with a high density of grid points close to the interface. (b) Composition of the austenite and ferrite phases used as input for the DICTRA simulation.
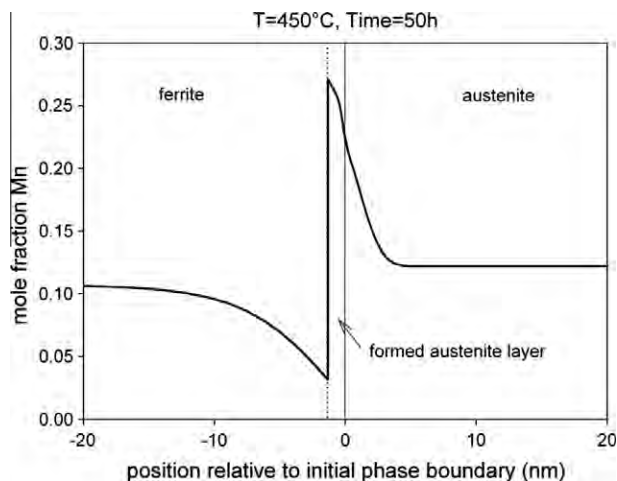
Fig. 6. DICTRA calculation of the Mn distribution at the martensite/austenite phase boundary. Martensite is thermodynamically and kinetically treated as ferrite. The calculation was done for 450 °C (aging temperature). The result is shown for the 180,000 s time step (50 h).
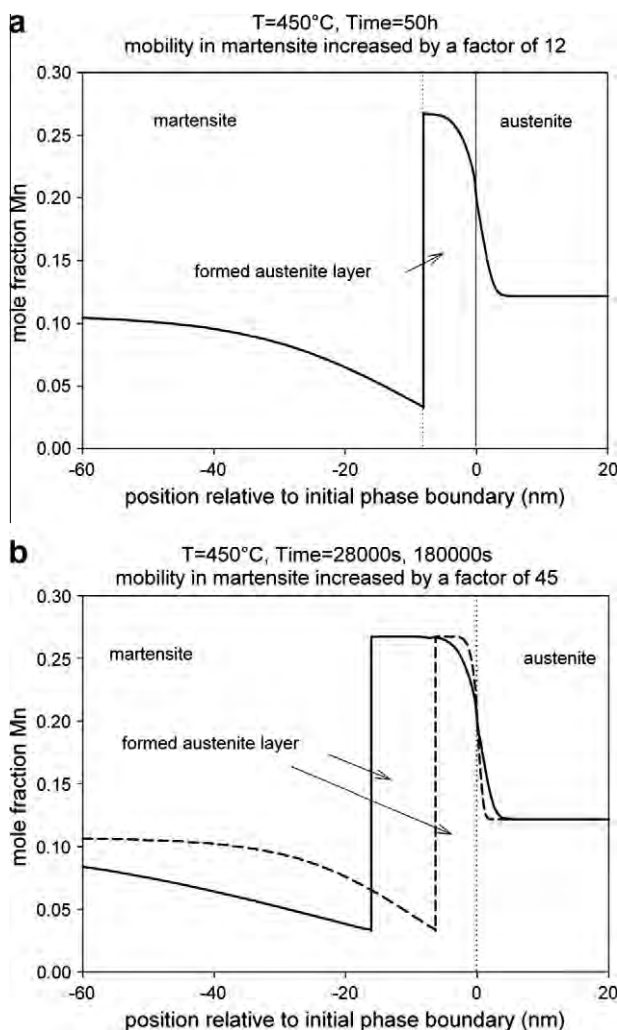
Fig. 7. DICTRA calculation of the Mn distribution at the martensite/austenite interface. Martensite is thermodynamically and kinetically treated as ferrite, but the mobility of the elements is increased by a factor of 12 (a) and 45 (b), respectively.

that the mobility of Mn in the martensitic matrix must be higher than it is in ferrite. Therefore, the simulations were repeated with increased mobilities of the elements in the ferrite. The results of the simulations with a factor 12 and 45, respectively, for the enhanced mobilities in martensite are shown in Fig. 7. The result in Fig. 7b (45 times enhanced Mn mobility in martensite) is in excellent agreement with the experimental results in Fig. 2b. This applies for the depletion profile of Mn in the martensite and also for the Mn-enriched interface zone.

In view of this good agreement, the profiles of the other elements should also be analyzed. Fig. 8a shows the composition profiles of some of the elements for a mobility factor of 45. Fig. 8b presents the predicted enrichment or depletion of the other elements, respectively, in the same way as for the experimental results. The partitioning tendencies of the elements are the same as observed in the experiment (compare Figs. 3a and b and 8a and b). The predicted enrichment of Mn and Ni and the depletion of Mo within the interfacial austenite layer are in good quantitative agreement with the experiments. For Ti and Si, the decrease is less pronounced in the simulation than in the experiment.

We estimated the mean diffusion paths of Mn atoms in both phases using the diffusion coefficients obtained for 450 °C using DICTRA (Mob2 database). The diffusion constant of Mn atoms in a bcc iron matrix (ferrite) was $D_{bcc} = 1.75 \times 10^{-22}$ m^2 s^{-1} and in the fcc iron matrix $D_{fcc} = 5.86 \times 10^{-24}$ m^2 s^{-1}. The mean diffusion path λ of Mn atoms for an aging time of $t = 48$ h was calculated using the volume diffusion equation for cubic metals: $\lambda = (6tD)^{1/2}$. The mean diffusion path of Mn atoms in the bcc lattice was about 13 nm and in the fcc lattice only about 2.5 nm. Thus, the diffusion length of Mn in bcc is significantly larger than in the fcc lattice. When correcting the mobility of the atoms by a factor of 45, as explained above, the diffusion constant in ferrite (which can be then treated as martensite) is 7.56×10^{-21} m^2 s^{-1}. For this case, the mean diffusion path of Mn in bcc increases from 13 to about 90 nm.

4. Discussion

4.1. Phase boundary motion with infinite interface mobility in the DICTRA approach

The global equilibrium calculated with Thermo-Calc (see Table 2) predicts a high amount of Mn in the retained austenite (27.6 at.%) and a low value (3 at.%) in ferrite. Hence, during aging a redistribution of Mn is expected. However, the global equilibrium only indicates the long term trends. The actual situation at the phase boundary is controlled by a local equilibrium.

It is not possible to visualize graphically equilibria in multicomponent systems. Therefore, the following discussion will be done considering only three components: Fe, Mn and Ni. Fig. 9 shows the ternary phase diagram at 450 °C. The initial compositions of martensite (filled

a T=450°C, Time=50h
mobility in martensite increased by a factor of 45

b

at. %	Interface layer	Global content	Enrichment within the layer, times
Mn	27.0	12.2	2.2
Ni	2.9	2.0	1.4

at. %	Interface layer	Global content	Depletion within the layer, times
Ti	0.4	1.17	2.9
Mo	0.4	0.60	1.5
Si	0.1	0.15	1.5

c

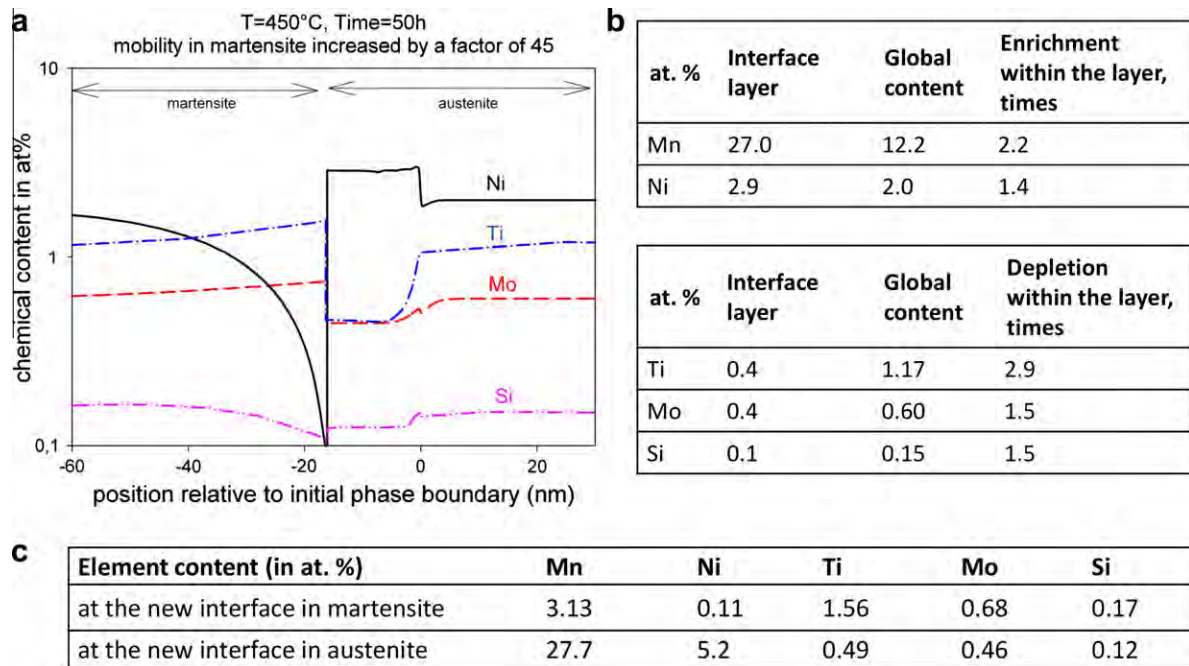| Element content (in at. %)	Mn	Ni	Ti	Mo	Si
at the new interface in martensite	3.13	0.11	1.56	0.68	0.17
at the new interface in austenite	27.7	5.2	0.49	0.46	0.12

Fig. 8. Results of DICTRA calculations. (a) Composition profiles of all elements included in the DICTRA simulation. (b) Quantitative characterization of the calculated profiles. (c) Element contents at the new interface between martensite and austenite at 450 °C for the given global composition.
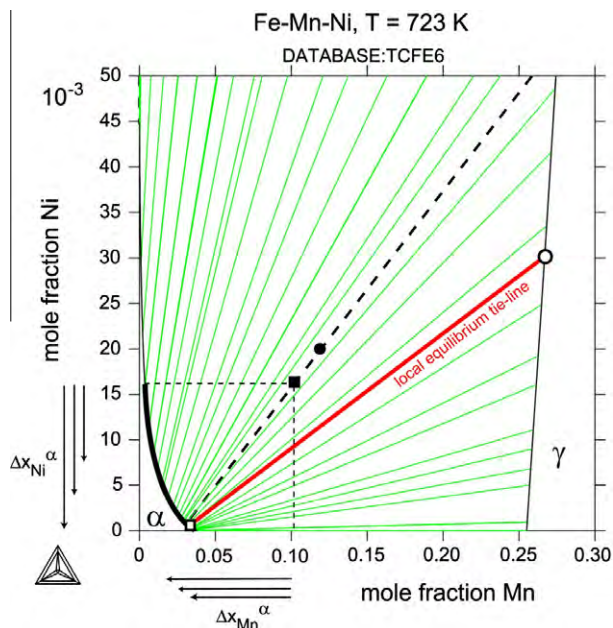
Fig. 9. Isothermal section of the Fe–Mn–Ni ternary system. The starting composition of austenite (filled circle) and martensite (filled square) are indicated. The global equilibrium tie-line is shown as a broken line. The bold part of the ferrite phase boundary indicates the range of possible local equilibrium tie-lines.

square) and austenite (filled circle) are within the two-phase region $\alpha + \gamma$. The global equilibrium tie-line is shown by a dotted line. The slope of the tie-lines indicates that at the austenite phase boundary the level of both Mn and Ni must be higher than in the matrix. Conversely, the level of Mn and Ni at the martensite boundary must be lower

than in the matrix. The range of possible local equilibrium tie-lines is thus confined to those originating from Ni concentrations in martensite below the value in the α-matrix, i.e. $x_{Ni}^{\alpha/\gamma} < x_{Ni}^{\alpha}$. This composition range is marked in Fig. 9 by a bold phase boundary. The operating local equilibrium tie-line is defined by the fluxes of Ni and Mn. The interface displacement caused by these fluxes must be the same for every diffusing element. The resulting operating local tie-line is indicated in Fig. 9, showing the difference to that of global equilibrium.

Due to the low diffusivity in austenite, the fluxes lead to an interface displacement towards martensite. The layer of increased Mn is the result of the partitioning imposed by the local equilibrium tie-line during the formation of austenite. Epitaxial formation of this aging-induced austenite at the phase boundary of the existing austenite is likely.

The overall agreement between experiment and simulation is very good. There is a slight difference in the Mn composition at the martensite boundary though. The experiments yield a value of about 5–6 at.% Mn, while the simulation gives a value of 3 at.%. There are two possibilities to explain this difference. (i) It could be an effect of the resolution of the experiment. The transition from the low concentration at the martensite boundary to the very high concentration at the austenite interface occurs sharply. It is, therefore, plausible that close to this abrupt transition the Mn signal is slightly contaminated by the elevated Mn concentration, leading to a slightly increased composition close to the boundary. (ii) It could be due to the finite mobility of the interface. The local equilibrium approach implies that the interface can move freely. A finite mobility of the interface (see details in the next

Fig. 10. Velocity of the interface α/γ as a function of time.

section) leads to a slower interface velocity than that given by the local equilibrium. Consequently, the boundary condition has to be adapted such that the mass balance is in accordance with the velocity. Th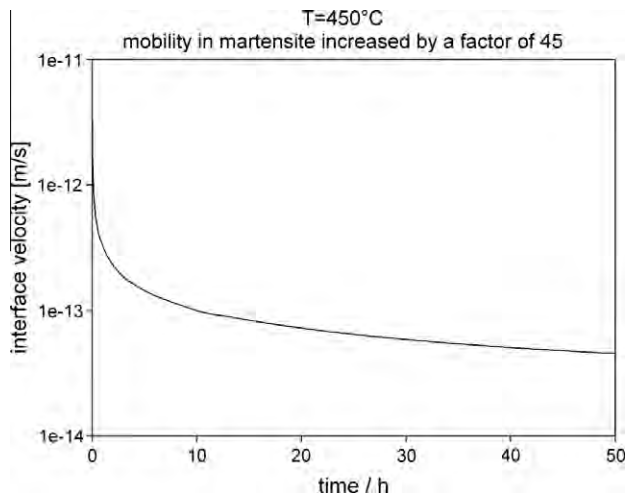is effect, however, should become more relevant at rather high interface velocities. In the present case of low temperature the interface velocity is small (see Fig. 10). This velocity range is more than six orders of magnitude smaller than usual velocities occurring during the transition between austenite and ferrite at temperatures of about 700 °C or higher. We anticipate, therefore, that the finite interface mobility effect might play a second-order role in the current case as discussed in more detail in the next section.

4.2. Phase boundary motion with finite interface mobility in the mixed-mode approach

The simulation of a partitioning phase transformation with DICTRA as outlined above is based on the assumption that Mn diffusion is controlling the transformation kinetics. In a more generalized mixed-mode approach [33,34] the motion of the interface during the transformation is defined by its velocity, v, given by:

$$v = M\Delta G \tag{1}$$

where ΔG is the free-energy difference between the phases, acting as the driving force for transformation, and M is the interface mobility. In the purely diffusion-controlled transformation, such as discussed above, M is assumed to be infinite, which means that the interface instantaneously reacts to any deviation of the local concentration from equilibrium, thus restoring the local equilibrium. If M is finite, however, a certain balance is established between diffusion (in the case of Mn in α increasing the interface concentration, which increases the driving force) and interface motion (decreasing the Mn concentration at the interface, which decreases the driving force). For given values of M and the diffusivity D, the resulting value of the interface concentration, and thus of the driving force and the

velocity, can be simulated for binary Fe–Mn on the basis of two assumptions [33]. The first one is that the driving force is proportional to the deviation from equilibrium:

$$\Delta G = \chi(x_{Mn}^{\alpha\gamma}) - x_{Mn}^{\alpha} \tag{2}$$

where the indices $\alpha\gamma$ denote the equilibrium concentration in the α-phase (martensite) in equilibrium with γ (austenite), and x_{Mn}^{α} is the Mn concentration in martensite at the interface. In the case of partitioning Mn, the proportionality factor χ is negative. The second assumption is that the diffusion in the parent martensitic α-phase leads to a concentration profile that can be described by an exponential function:

$$x_{Mn} = x_0 + (x_{Mn}^{\alpha} - x_0)\exp\left(-\frac{z}{z_0}\right) \tag{3}$$

with the spatial coordinate $z = 0$ at the interface. The width parameter z_0 follows from the values of M and D and the equilibrium and overall (x_0) concentrations [33]. Diffusion of Mn in the austenite is so slow that it can be neglected.

The experimental profile in Fig. 2b shows a Mn concentration in the α-phase at the interface of 5–6 at.%, which is slightly larger than the equilibrium value of 3.3 at.%. This would imply a deviation from local equilibrium. Using the value of the interface mobility M as an adaptable parameter and the same enhanced Mn diffusivity (factor 45) as used in the DICTRA simulations above, the Mn profile in the martensitic phase can be adequately reproduced (Fig. 11). The final profile ($t = 180,000$ s) is given, but also an intermediate stage, after 28,000 s. It is revealed that the deviation from equilibrium is larger in the earlier stages of the transformation. The calculations were conducted for a value of $\chi = -12.8$ kJ mol^{-1}, determined with Thermo-Calc, and a mobility of $M = 2 \times 10^{-21}$ m^4 J^{-1} s^{-1} at $T = 450$ °C. The simulated results reveal an excellent
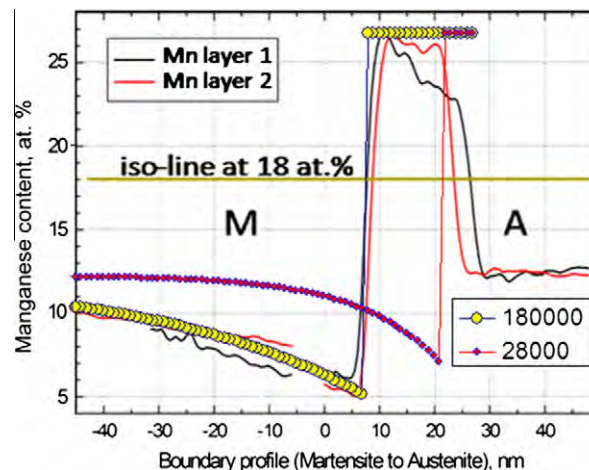

Fig. 11. Results of the mixed-mode predictions of the Mn profile across the austenite/martensite interfaces. In contrast to the DICTRA simulation, here the interface mobility is taken into account [33]. The mixed-mode simulation results for two aging times (red points: 28,000 s; yellow points: 180,000 s) are plotted together with the experimental data (red and black lines, see Fig. 2b).

agreement with the experiments (Fig. 11). The mobility value, however, is distinctly smaller than the mobility data for the standard $\gamma \to \alpha$ transformation around $T = 800\ °C$, when extrapolating with the commonly used activation energy for the mobility of $140\ \text{kJ mol}^{-1}$.

The mixed-mode approach uses the interface mobility as an adaptable parameter. This approach is particularly useful in cases where the transition is not fully controlled by diffusion. In such cases the local chemical equilibrium condition cannot be fulfilled. Instead, a difference in chemical potentials exists at the interface which provides the Gibbs energy required for the motion of the interface. If the interface mobility is known and does act as a limiting kinetic factor, it may play an essential role in the formation of the overall microstructure and hence should be included in the corresponding predictions.

4.3. Comparison and conclusions from the two simulation methods

The Mn distributions predicted by the calculations revealed diffusion of Mn from the ferritic phase towards the austenitic matrix and the accumulation of Mn at the interface between these two regions. The composition profiles obtained experimentally agree with the simulations provided that the mobilities of all alloying elements in martensite are increased compared to ferrite (by a factor of 45, Fig. 7b). This applies to both types of simulation approaches, i.e. DICTRA [30–32] and mixed-mode [33,34]. Such an enhanced diffusion in martensite can be attributed to a high defect concentration (e.g. misfit dislocations introduced through the transformation) in martensite. Pipe diffusion might therefore be one reason for this enhanced diffusion [12–14].

So far it is not clear whether the higher mobility is valid for martensite in general or if this holds only in the neighborhood of the phase boundary which may act as a source of vacancies and provides high local dislocation densities in its vicinity [35]. More experimental information is needed to elucidate this point.

5. Conclusions

We studied compositional variation phenomena on martensite/austenite interfaces in a maraging-TRIP steel. We placed particular attention on the partitioning of Mn at these interfaces using 3-D atom probe analysis in conjunction with Thermo-Calc, DICTRA and mixed-mode simulations (where the latter also includes the heterophase interface mobility). The local boundary condition at the interface leads to the diffusion of Mn in martensite towards austenite. The chemical gradients of Mn predicted by DICTRA at the phase boundary revealed a good quantitative correlation to the experimental findings. The diffusion behavior of other alloying elements such as Ni, Ti and Mo could also be reproduced in the dynamic simulation.

The partitioning at the martensite/austenite interface leads to the formation and growth of a new austenite layer on the existing retained austenite with drastically changed composition compared to the bulk. It is to be expected that such a layer will have an effect on the mechanical properties. In the present case, this layer is likely to be one of the microstructural changes during aging that might be responsible for the unexpected increase in ductility after the annealing treatment [12]. The other contribution for increasing the ductility stems from the tempering of the martensitic matrix during annealing and was reported elsewhere [36].

By using the advanced APT technique we gained deep insights into the chemical nature and dynamics of the martensite/austenite phase boundary during aging. The theory-assisted 3-D chemical analysis at the nanoscale provides significant enhancement of our understanding of partitioning affects and their relationship to phase transformation kinetics in multiphase steels.

Appendix A. Supplementary material

Supplementary data associated with this article can be found, in the online version, at doi:10.1016/j.actamat.2010.09.042.

References

[1] Patel JR, Cohen M. Acta Metall 1953;1:531.
[2] Bhadeshia HKDH, Edmonds DV. Metall Trans 1979;10A:895.
[3] Takahashi M, Bhadeshia HKDH. Mater Trans JIM 1991;32:689.
[4] Jacques PJ, Girault E, Catlin T, Geerlofs N, Kop T, van der Zwaag S, et al. Mater Sci Eng 1999;A273–275:475.
[5] De Meyer M, Vanderschueren D, De Cooman BC. ISIJ Int 1999;39:813.
[6] Traint S, Pichler A, Hauzenberger K, Stiaszny P, Werner E. Steel Res Int 2002;73:259.
[7] Zaefferer S, Ohlert J, Bleck W. Acta Mater 2004;52:2765.
[8] Brüx U, Frommeyer G, Grässel O, Meyer LW, Weise A. Steel Res 2002;73:294.
[9] Tomota Y, Strum M, Morris JW. Metall Mater Trans 1986;17A:537.
[10] Song R, Ponge D, Raabe D, Kaspar R. Acta Mater 2004;53:845.
[11] Song R, Ponge D, Raabe D. Acta Mater 2005;53:4881.
[12] Raabe D, Ponge D, Dmitrieva O, Sander B. Scripta Mater 2009;60:1141.
[13] Raabe D, Ponge D, Dmitrieva O, Sander B. Adv Eng Mater 2009;11(7):547.
[14] Ponge D, Millán J, Dmitrieva O, Sander B, Kostka A, Raabe D. In: Proc 2nd int symp steel sci (ISSS 2009). Kyoto: The Iron and Steel Institute of Japan; 2009. p. 121.
[15] Cerezo A, Godfrey TJ, Smith GDW. Rev Sci Instrum 1988;59:862.
[16] Blavette D, Deconihout B, Bostel A, Sarrau JM, Bouet M, Menand A. Rev Sci Instrum 1993;64:2911.
[17] Miller MK, Cerezo A, Hetherington MG, Smith GDW. Atom probe field ion microscopy. Oxford: Oxford University Press; 1996.
[18] Thuvander M, Miller MK, Stiller K. Mater Sci Eng A 1999;270:38.
[19] Miller MK. Atom probe tomography analysis at the atomic scale. New York: Kluwer Academic/Plenum; 2000.
[20] Kelly TF, Miller MK. Rev Sci Instrum 2007;78:031101.
[21] Seidman D. Annu Rev Mater Sci 2007;37:127.
[22] Miller MK, Forbes RG. Mater Charact 2009;60:461.
[23] Marquis EA, Miller MK, Blavette D, Ringer SP, Sudbrack CK, Smith GDW. MRS Bull 2009;34:725.

[24] Pereloma EV, Stohr RA, Miller MK, Ringer SP. Metall Mater Trans 2009;40A:3069.

[25] Sauvage X, Lefebvre W, Genevois C, Ohsaki S, Hono K. Scripta Mater 2009;60:1056.

[26] Al-Kassab T, Wollenberger H, Schmitz G, Kirchheim R. Tomography by atom probe. In: Rühle M, Ernst F, editors. High resolution imaging and spectroscopy of materials. Springer series in materials science, vol. 50. Berlin: Springer-Verlag; 2000.

[27] Choi P, da Silva M, Klement U, Al-Kassab T, Kirchheim R. Acta Mater 2005;53:4473.

[28] Thermo-Calc Users' Guide, Version R. Stockholm: Thermo-Calc Software AB and Foundation of Computational Thermodynamics; 1995–2006.

[29] Thermodynamic database TCFE6 – TCS Steels/Fe-Alloys Database, Version 6.2, Thermo-Calc Software, www.thermocalc.com.

[30] Borgenstam A, Engström A, Höglund L, Ågren J. J Phase Equilib 2000;21:269.

[31] Crusius S, Inden G, Knoop U, Höglund L, Ågren J. Z Metallk 1992;83:673.

[32] Franke P, Inden G. Z Metallk 1997;88:917.

[33] Bos C, Sietsma J. Scripta Mater 2007;57:1085.

[34] Sietsma J, van der Zwaag S. Acta Mater 2004;52:4143.

[35] Calcagnotto M, Ponge D, Raabe D. Mater Sci Eng A 2010;527:2738.

[36] Ponge D, Millán J, Dmitrieva O, Sander B, Kostka A, Raabe D. Proc 2nd int symp on steel science (ISSS 2009). Kyoto: The Iron and Steel Institute of Japan; 2009. p. 121.

Atomic-scale mechanisms of deformation-induced cementite decomposition in pearlite

Y.J. Li [a,b,*], P. Choi [b], C. Borchers [a], S. Westerkamp [a], S. Goto [c], D. Raabe [b], R. Kirchheim [a,b]

[a] *Institut für Materialphysik, Georg-August-Universität Göttingen, Friedrich-Hund-Platz 1, D-37077 Göttingen, Germany*
[b] *Max-Planck Institut für Eisenforschung, Max-Planck-Str. 1, D-40237 Düsseldorf, Germany*
[c] *Department of Materials Science and Engineering, Faculty of Engineering and Resource Science, Akita University, Tegata Gakuencho, Akita 010-0852, Japan*

Abstract

Pearlitic steel can exhibit tensile strengths higher than 5 GPa after severe plastic deformation, where the deformation promotes a refinement of the lamellar structure and cementite decomposition. However, a convincing correlation between deformation and cementite decomposition in pearlite is still absent. In the present work, a local electrode atom probe was used to characterize the microstructural evolution of pearlitic steel, cold-drawn with progressive strains up to 5.4. Transmission electron microscopy was also employed to perform complementary analyses of the microstructure. Both methods yielded consistent results. The overall carbon content in the detected volumes as well as the carbon concentrations in ferrite and cementite were measured by atom probe. In addition, the thickness of the cementite filaments was determined. In ferrite, we found a correlation of carbon concentration with the strain, and in cementite, we found a correlation of carbon concentration with the lamella thickness. Direct evidence for the formation of cell/subgrain boundaries in ferrite and segregation of carbon atoms at these defects was found. Based on these findings, the mechanisms of cementite decomposition are discussed in terms of carbon–dislocation interaction.

1. Introduction

Pearlitic steel subjected to a severe plastic deformation (SPD) process such as heavy cold-drawing can exhibit tensile strengths higher than 5 GPa [1] and is therefore the strongest structural bulk alloy known. Despite its great potential for engineering applications (e.g. as suspension bridge cables, tire cords, springs and wires), the correlation between the enormous strength of pearlite and its microstructural evolution during SPD is still a matter of debate. While the tensile strength can be measured with standard

equipment, an understanding of the microstructural evolution is often limited by the resolution of the microscopic technique used, as the mechanisms involved are often of an atomic-scale nature. A typical microstructural change, frequently observed with transmission electron microscopy (TEM), is the refinement of the lamellar structure down to several nanometers upon straining [2–7]. This led to the proposal that the strength and the lamellar spacing follows a Hall–Petch relation [2,8]. In addition to the formation of the nanoscaled filaments, a concurrent decomposition of cementite was observed by performing Mössbauer spectroscopy [9], field ion microscopy (FIM) [3,4,10–14] and atom probe tomography (APT) [3,4,6,7,15–17]. Combined internal friction [18] and Mössbauer [19,20] experiments suggested that 20–50 vol.% of the cementite phase decomposes during deformation at room temperature. Such a decomposition process is reported to increase the average

* Corresponding author at: Max-Planck Institut für Eisenforschung, Max-Planck-Str. 1, D-40237 Düsseldorf, Germany. Tel.: +49 211 6792853; fax: +49 211 6792333.

E-mail addresses: y.li@mpie.de (Y.J. Li), d.raabe@mpie.de (D. Raabe), rkirch@ump.gwdg.de (R. Kirchheim).

carbon concentration in ferrite far above the equilibrium concentration and to invoke an additional strengthening mechanism due to mechanical alloying (with the assumption that the dissolved carbon atoms are homogeneously distributed in the ferrite). However, since the first report on the decomposition of cementite in the 1960s [21], both the exact mechanism of the decomposition process and the location of the dissolved carbon atoms in ferrite are still a subject of controversy.

As reviewed by Gavriljuk [22,23], there are generally two interpretations of cementite decomposition. Gridnev et al. [19,22] proposed that cementite decomposition is due to the much higher binding energy between carbon interstitials and ferrite dislocations (0.75 eV [24]) as compared to the binding energy of carbon atoms in the cementite lattice (0.40–0.42 eV [25,26]). Thus, ferrite dislocations near the interface with cementite drag carbon atoms out of the cementite into the ferrite, forming a Cottrell atmosphere. On the other hand, Languillaume et al. [27] suggested that the increase in free energy, caused by the geometrical thinning of cementite lamellae and the creation of slip steps during wire drawing, destabilizes cementite and promotes its decomposition. A similar thermodynamic model, based on the Gibbs–Thomson effect and a diffusion-controlled dissolution process, was proposed in Ref. [16].

However, as pointed out by Gavriljuk [23], the models of cementite decomposition proposed in the literature still require experimental proof. To date, it has been a great challenge to tackle this issue due to a lack of appropriate high-resolution characterization techniques with sufficient compositional accuracy. APT has been shown to be one of the most powerful tools for analyzing pearlite [3,4,6,7,15–17]. In the early stages of atom probe development, one-dimensional atom probe (1DAP) has frequently been used to analyze the carbon concentration in deformed pearlitic steels. However, 1DAP is known to probe a very limited number of atoms with a small field-of-view due to a small acceptance angle of the mass spectrometer [28]. In addition, the specimen preparation technique is also crucial for obtaining reliable quantitative atom probe data. Conventional electropolishing methods normally allow for the preparation of cementite lamellae parallel but not normal to the direction of analysis. Thus, the number of detected cementite lamellae is limited by the field-of-view. Furthermore, the spatial resolution in the analysis direction (perpendicular to the lamellar interfaces) is reported to be low [29] due to the local magnification effect [17,30]. These problems can be overcome by applying focused ion-beam (FIB) milling and the lift-out method according to Refs. [31–33]. A substantial number of cementite lamellae, lying perpendicular to the direction of high field-of-view analysis, can be probed with enhanced spatial resolution, Moreover, local electrode atom probe allows us to study the decomposition of cementite more accurately with higher statistical significance as compared to conventional three-dimensional atom probes (3DAP) [3,4,6,7,15–17].

In the present work, a local electrode atom probe (LEAP) is employed to analyze the carbon distribution in three dimensions. The instrument has several advantages over conventional atom probes such as larger probed volumes ($100 \times 100 \times 1000$ nm^3) and a higher detection sensitivity due to an improved mass resolution ($\Delta m/m = 1/1100$, full width at half maximum at 27 Da (Da is the atomic mass unit)). Cold-drawn pearlitic steels with true strains ranging from 0 (as-patented) to 5.4 were systematically studied with respect to their carbon distribution. Clear correlations between the carbon concentration in ferrite and the strain as well as between the carbon concentration in the cementite lamellae and their thickness were found. There were also strong indications for the formation of cell/subgrain boundaries in the ferrite and the segregation of carbon atoms at these defects. Based on these findings, the mechanisms of cementite decomposition are discussed in terms of solute–dislocation interactions.

2. Experimental

The materials studied in this work are commercial pearlitic steel wires with eutectoid composition (Fe–0.81C–0.49Mn–0.20Si–0.006P–0.008S wt.% and Fe–3.66C–0.48Mn–0.39Si–0.01P–0.01S at.%) provided by Nippon Steel Corporation. The wires, with an initial diameter of 1.70 mm, were patented with an austenitization treatment at 1223 K for 80 s followed by a pearlitic transformation in a lead bath at 853 K for 20 s. The patented wires were cold-drawn (using lubricants) to true strains ϵ of 0 (as-patented), 0.93, 2, 3.47, 5 and 5.4, respectively.

A LEAP (LEAP 3000X HR™, Cameca Instruments) was employed to analyze the carbon distribution in three dimensions. The measurements were performed in voltage mode at 70 K under an ultra-high vacuum of 8×10^{-9} Pa. The total voltage during probing was in the range of 6.2–7.2 kV. The pulse fraction was 15%. The pulse repetition rate was 200 kHz at detection rate of 0.005 atom per pulse.

Samples for APT analyses were prepared with the tips perpendicular to the wire axis using a dual-beam FIB (FEI Helios NanoLab 600TM) according to the procedure described in Ref. [29]. Since the friction between the wire and drawing tools can cause more plastic deformation at the surface than in the center of a wire, the microstructure of the wire may be slightly different from the surface to the center. However, this difference decays with increasing drawing strain. For instance, at $\epsilon = 5$, the tips taken from regions 5 and 25 μm below the surface show virtually no difference in terms of the maximum carbon concentration in cementite [29]. To achieve consistent analyses, all tips were taken from the surface regions of the wires. During annular milling about 250 nm of the material was removed from the surface. Thus, the apex of each tip was located about 250 nm below the wire surface.

Samples for TEM observations were prepared with a FIB FEI Nova 600 Nano Lab with electron optics operated at 5 kV, sample preparation done with 30 kV Ga ions, and
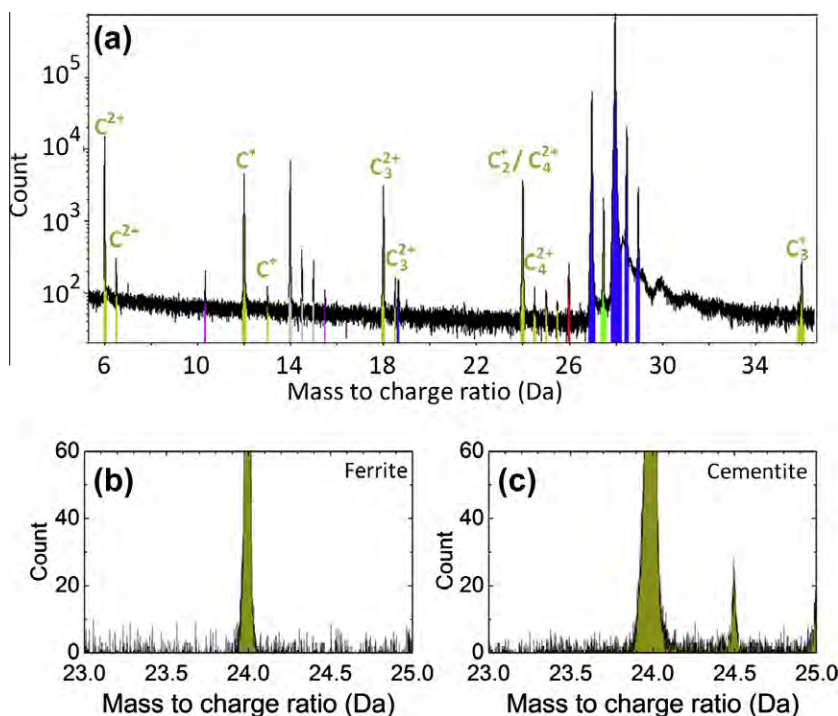
Fig. 1. (a) Example of mass spectrum of a pearlitic steel wire at $\epsilon = 5.4$. All carbon peaks can be identified and are marked. Peaks for the other main elements Fe, Mn and Si are given in blue, green and gray, respectively. (b) and (c) Mass spectra of ferrite and cementite, respectively. Note the presence of the peak of 24.5 Da only in the cementite.

a final finish with 5 kV Ga ions. TEM was performed with a Philips CM30 operated at an acceleration voltage of 300 kV.

3. Results

3.1. Chemical composition measured by using LEAP

Fig. 1 shows a typical mass spectrum of the cold-drawn pearlitic steel wire with $\epsilon = 5.4$. All the mass-to-charge peaks of carbon atoms and molecules are identified and marked. Following a standard assignment method [3,15,29,34,35], the carbon peaks at mass-to-charge ratios $m/n = 6$ and 6.5, 12 and 13, 18 and 18.5, 24.5 and 36 Da can be assigned without ambiguity to C^{2+}, C^{+}, C_3^{2+}, C_4^{2+} and C_3^{+}, respectively. For the peak at 24 Da, however, there exists an uncertainty; it could be due to either C_2^{+} or C_4^{2+}, or a mixture of both. In the literature, this peak is generally assigned as C_2^{+} [3,15,29,36].

Taking into account the relative abundance of isotopes of carbon C_4 including mainly $^{12}C_4^{2+}$ and $(^{12}C_3^{13}C)^{2+}$, Sha et al. concluded that over 50% of the ions detected at the peak of 24 Da are in fact C_4^{2+} [35]. Fig. 1a reveals the existence of the isotope $(^{12}C_3^{13}C)^{2+}$ at the peak of 24.5 Da. Thus, there should exist a certain amount of $^{12}C_4^{2+}$ ions at the peak of 24 Da. A further analysis by using a peak decomposition algorithm (supplied by the software IVAS, Cameca Instruments) similar to the calculation method of Sha et al. [35] shows that the contributions of $^{12}C_2^{+}$ and $^{12}C_4^{2+}$ to this peak are 58% and 42%, respectively. It is

worth noting that the ratios of the two types of ions may differ from one specimen to another, but all values measured in samples with various drawing strains lie in the range of 40–60%.

If the chemical compositions of ferrite[1] (Fig. 1b) and cementite[2] (Fig. 1c) are separately determined, namely by individually cutting each phase out of the entire volume and evaluating the respective mass spectrum, it is found that the peak of 24.5 Da is only present in cementite but not in ferrite. This means that the peak of 24 Da in ferrite can be exclusively assigned to $^{12}C_2^{+}$. For cementite, as mentioned above, there must exist a contribution of $^{12}C_4^{2+}$ to the peak of 24 Da. This is confirmed by the quantitative analysis of the peak decomposition algorithm.

Table 1 displays the average chemical compositions (including both ferrite and cementite) measured by LEAP and the nominal values of all samples. The total number of ions detected in each measurement is also given for a statistical evaluation of accuracy. For the peak of 24 Da the C ion is alternatively assigned as $^{12}C_2^{+}$ and $^{12}C_4^{2+}$. Both results are displayed in Table 1. For the as-patented wire ($\epsilon = 0$) no cementite lamella is detected because of a premature fracture of the sample tip, as the material is relatively soft. Thus, the measured values are obtained only from the ferrite. The measured carbon concentration of 0.05 at.%, which is far above the solubility of carbon atoms in ferrite

---

[1] Defined here as the region with a carbon concentration lower than 3 at.%.

[2] The region with a carbon concentration higher than 7 at.%

Table 1

Comparison between the nominal chemical composition and the values measured by LEAP in the case of assigning the peak of 24 Da to C_2^+ and C_4^{2+}. Unit: at.%.

Element	Nominal	$\epsilon = 0$		$\epsilon = 0.93$		$\epsilon = 2.00$		$\epsilon = 3.47$		$\epsilon = 5.00$		$\epsilon = 5.40$	
		C_2^+	C_4^{2+}	C_2^+	C_4^{2+}	C_2^+	C_4^{2+}	C_2^+	C_4^{2+}	C_2^+	C_4^{2+}	C_2^+	C_4^{2+}
C	3.66	0.05	–	2.59	3.19	3.57	4.37	1.98	2.47	2.82	3.55	3.10	3.89
Si	0.39	0.51	–	0.44	0.44	0.43	0.42	0.53	0.53	0.44	0.44	0.48	0.47
Mn	0.48	0.36	–	0.47	0.46	0.47	0.47	0.41	0.41	0.49	0.49	0.23	0.23
Ga	0	0.04	–	0.13	0.13	0.04	0.03	0.31	0.31	0	0	0	0
Total ions		1,980,000		1,300,000		6,800,000		5,100,000		38,000,000		18,900,000	

at equilibrium, indicates that the as-patented state is already in a non-equilibrium condition. This value is in good agreement with that measured in Ref. [15]. The deviation of the measured carbon contents from the nominal values for $\epsilon = 0.93$ and 3.47 is due to premature tip failure and low counting statistics. For larger detected volumes, as in the cases of $\epsilon = 2$, 5 and 5.4, the statistical quality improves. Consequently, the measured average carbon concentrations are in good agreement with the nominal values, in particular, when the weight factors of $^{12}C_2^+$ and $^{12}C_4^{2+}$ at the peak of 24 Da are taken into account. For the elements, which are homogeneously distributed in pearlite, e.g. Si and Mn, the values measured by LEAP are always close to the nominal ones. The results listed in Table 1 are strong indications for a correct measurement of the chemical composition.

3.2. Investigation of lamellar structure of pearlite by TEM and LEAP

Fig. 2 shows the TEM images of pearlitic wires in the as-patented as well as cold-drawn states. The ferrite regions are separated by thin cementite filaments (dark gray). The dark lines, which cross the ferrite and connect two neighboring cementite lamellae (Fig. 2b), mark cell or low-angle grain boundaries of dislocations, as also reported in Ref. [8]. The high strain contrast in the deformed microstructures indicates a high density of deformation-related defects.

In Fig. 2a–c, we observe a refinement of the lamellar structure with increasing drawing strain. The mean ferrite lamella thickness decreases from about 56 nm for the as-patented state to about 10 nm for $\epsilon = 5$. The mean cementite lamella thickness decreases from 17 to 2 nm. This can also be observed in the 3D atom maps of the wires at $\epsilon = 2$ and 5 (Fig. 3). Here, the carbon-enriched (yellow) and -depleted regions (blue) can be identified as cementite and ferrite, respectively. The variation in the lamellar spacing, as for example shown in Fig. 2b, has been consistently reconstructed in the 3D maps (see e.g. Fig. 3 $\epsilon = 2$). Quantitatively, both TEM and APT images indicate that the average interlamellar spacing decreases from an initial value of 70 nm (as-patented) to 25 nm for $\epsilon = 2$ and further to about 13 nm for $\epsilon = 5$. Fig. 4 displays atom maps (top and middle) and the corresponding 1D carbon concentrations profiles (bottom) of the regions taken from Fig. 3.

Clearly, in addition to the refinement of lamellar spacing, the cementite filaments also become thinner, while the phase boundaries become blurred.

3.3. Carbon concentration in ferrite and cementite

One-dimensional concentration profiles have been frequently used to quantify the overall carbon concentration in pearlitic steel wires [3,4,15,29]. As Fig. 4 shows, when the drawing strain increases from 2 to 5, the carbon concentration in cementite decreases to about 10 at.%, far below the stoichiometric value of 25 at.%. Concomitantly, the carbon concentration in ferrite rises up to 2 at.%. Both findings give direct evidence of cementite decomposition. While the tendency of changing carbon concentrations in both phases is correct, the extraordinarily high carbon concentration of 2 at.% in ferrite is discussed in the following. As mentioned above, for ferrite the peak of 24 Da exclusively corresponds to $^{12}C_2^+$. For cementite, $^{12}C_4^{2+}$ should also be taken into account. Thus the carbon atoms in ferrite and cementite cannot be correctly assigned with an overall 1D concentration profile consisting of both phases. Instead, as proposed in our previous work [37], to achieve a better accuracy in the analysis, one should isolate each phase from the entire 3D volume separately and perform an individual analysis. The details of the subcutting method are reported in Ref. [37].

Fig. 5 shows the carbon concentrations (measured with the subcutting method) in ferrite as a function of wire strain. Each data point is obtained from averaging over 3–10 measurements. The values measured in all wires lie below 0.6 at.% C, which is much smaller than the value obtained from the 1D concentration profiles (Fig. 4). It is seen that the solubility of carbon atoms in ferrite is not a monotonically increasing function of the drawing strain, but starts to saturate at a certain strain ($\epsilon \geqslant 3.47$ in the present work). This observation implies that a saturation of cementite decomposition may also occur at that strain.

The data found in the literature [13,37] (dash-dotted line with small open square symbols) shows a similar concentration–strain relation but with a higher carbon saturation concentration. The higher saturation concentration can be attributed to the fact that this material contains a higher overall carbon concentration of 4.40 at.% than the present material (3.66 at.%).
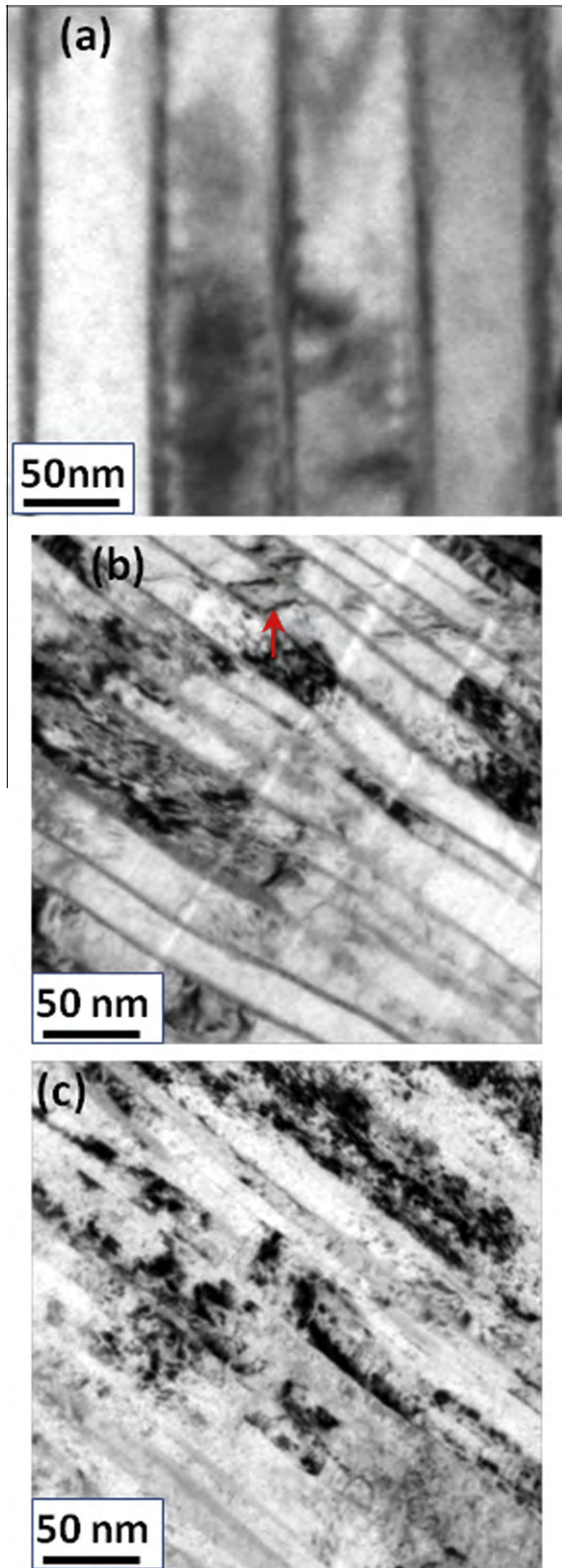
Fig. 2. TEM images of wires taken in longitudinal direction for (a) as-patented state, (b) $\epsilon = 2$ and (c) $\epsilon = 5$. The arrow marks one of the cell boundaries.

Fig. 6 displays the carbon concentration in cementite as a function of the lamellar thickness. The carbon concentra-

tion is measured in the middle of each cementite lamella to avoid errors due to variations in the local magnification (the so-called local magnification effect, see [37] for more details). All samples of different strain share a common feature: the carbon concentration decreases with decreasing thickness of the cementite lamellae. For the same cementite thickness the carbon concentration decreases during further straining from $\epsilon = 2$–3.47. It should be noted that the influence of strain is inverse to the thickness. The curves show a tendency that in those cementite lamellae with sufficient thickness the strain effect may become negligible and the carbon concentration matches the stoichiometric value of 25 at.% for Fe_{3C}. For $\epsilon \geqslant 3.47$ the influence of the drawing strain disappears so that the cementite filaments with the same thickness exhibit the same carbon concentration. This is consistent with the results observed in Fig. 5 where the carbon concentration in ferrite saturates at the same strain.

Evidently, as shown in Figs. 5 and 6, the decomposition is promoted by plastic deformation but within a limited strain regime. Above a critical strain, e.g. 3.47 in the present case, the decomposition of cementite does not proceed. This means that the effect of plastic deformation on cementite decomposition has its limit. In fact, a lamellar structure still exists in the wire produced at even higher plastic deformation of $\epsilon = 6.02$ [37]. The saturation of cementite decomposition at high strain has also been confirmed by Mössbauer spectroscopy investigations [20,38].

The transport of carbon atoms from cementite into ferrite should, in principle, follow the rule of mass balance, namely the loss of carbon atoms in cementite is compensated by the same amount of atoms in ferrite. This leads to a direct connection between the changes of carbon concentration in both phases. According to the carbon concentration in cementite shown in Fig. 6, we are able to estimate the corresponding carbon concentration in ferrite on the basis of the rule of mass balance (see Appendix A for the detailed estimation procedure). The calculation yields a concentration in ferrite of 0.55 at.% C for $\epsilon = 2$ and 1.46 at.% C for $\epsilon \geqslant 3.47$, which are distinctly larger than the respective measured values of 0.3 and 0.5 at.% C (see Fig. 5). However, it should be noted that the data shown in Fig. 5 are measured only in the selected regions (relatively far from the cementite) with a concentration of less than 3 at.% C. If the regions of a carbon concentration between 3 and 7 at.%, which are located near the phase boundaries, are also considered as ferrite, the average carbon concentration in ferrite would increase up to 0.5 at.% for $\epsilon = 2$ and $1.3 \sim 1.7$ at.% for $\epsilon \geqslant 3.47$, respectively, which are in good agreement with the estimated values, as shown in Fig. 7. While these regions dramatically enhance the average carbon concentration in ferrite, they hold volume fractions of only 5% for $\epsilon = 2$ and 15% for $\epsilon \geqslant 3.47$, respectively. This would mean a strongly heterogeneous distribution of carbon atoms in ferrite so that most carbon atoms are located near the phase boundary, where most of dislocations get stored.
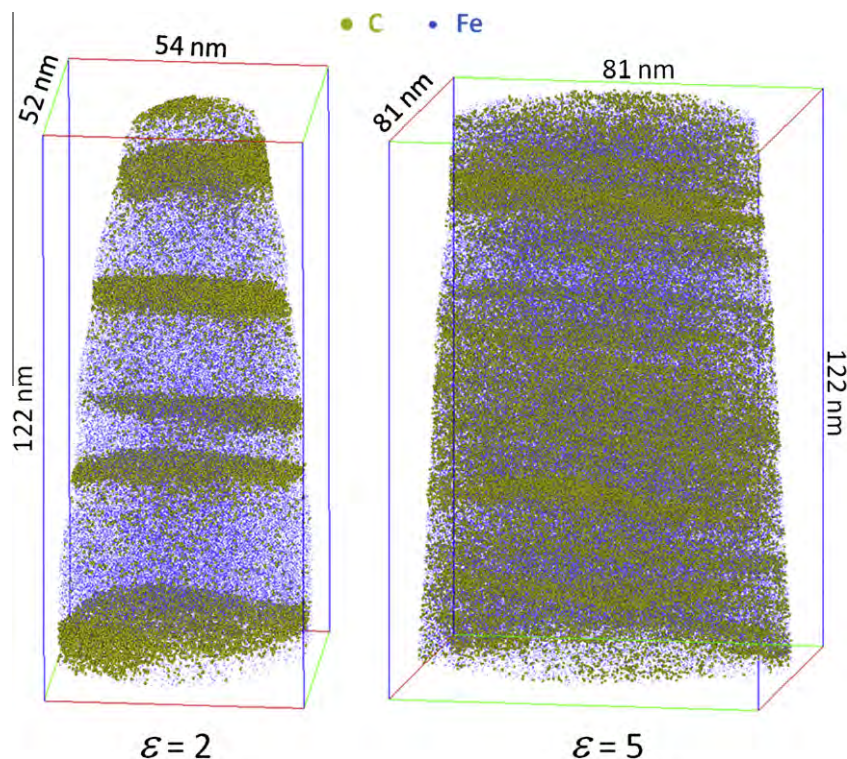
Fig. 3. 3D atom maps of cold-drawn wires for $\epsilon = 2$ (left) containing roughly 6.8×10^6 atoms within a volume of $54 \times 52 \times 122$ nm^3 and $\epsilon = 5$ (right) containing 16.2×10^6 atoms within a volume of $81 \times 81 \times 122$ nm^3. For clarity only 2% of the iron (blue) and 20% of the carbon (yellow) atoms are displayed.

3.4. Segregation of carbon atoms in ferrite

Fig. 8a shows a 3D map of carbon atoms for a wire at $\epsilon = 0.93$. A region of interest (ROI) (marked by the pink box) is selected from the ferrite for a closer investigation. As can be seen from Fig. 8b, the distribution of carbon atoms is not homogeneous. The carbon atoms are mainly located in a curved region, while the rest of the selected ROI is virtually free of carbon atoms. Fig. 8c displays the 3D map for Si and Mn atoms in the ROI, where both elements are distributed relatively homogeneously. The latter observation has been reported previously [3,29]. This result is also confirmed by the nearest-neighbor distance distributions for Si and Mn atoms (Fig. 8e). For carbon atoms, as shown in Fig. 8d, the measured data (solid line) deviates from the randomized distribution (dotted line), indicating their inhomogeneous distribution in the ROI.

Fig. 9 shows another sample observed in the wire produced with $\epsilon = 2$. One can recognize two carbon-enriched zones in the ferrite (marked B1 and B2), which reach from one cementite lamella to the neighboring one (see top figure). The 3D carbon atom map of the ROI shown in Fig. 10 (front view) highlights a strip intersecting with zone B2 at the top of Fig 9. We interpret the carbon enrichment in the two-dimensional zones B1 and B2 as cell or low-angle grain boundaries, as confirmed by TEM observations [8,14] . Most carbon atoms are segregated at the boundary (see Fig. 10a and c). In contrast, Mn and Si atoms are

homogeneously distributed throughout the cell, as shown in Fig. 10b and d.

The segregation of carbon atoms at grain boundaries is more frequently observed in the materials drawn to even higher strains of 3.47 and 5.4. For example, Fig. 11 shows that, in a small selected volume, two parallel cell/low-angle grain boundaries exist. The 2D boundary surface is also revealed by the closer investigation of the ROI (marked with pink color) as shown in Fig. 11b and c. The segregation of carbons atoms at the boundary can be easily recognized from both the atom maps shown in Fig. 11b and c and the concentration profile in Fig. 11d. It should be noted that the peak carbon concentration located in the center of the boundary is higher by a factor of about 2 than that found in Fig. 10c. This observation is a strong indication that cementite decomposition and carbon segregation to cell or grain boundaries are both promoted by plastic deformation. The distribution of Si and Mn atoms is also shown in the figure to validate the statistics for the measurement. Both elements are homogeneously distributed in the sample as also seen in Fig. 10d.

4. Discussion

SPD is an efficient method of refining the lamellar structure of pearlite, and involves refining the thickness as well as the spacing of the cementite lamellae. Such a refinement can be observed by scanning electron microscopy (SEM) [39] and TEM [2]. The refinement of the cementite lamellae
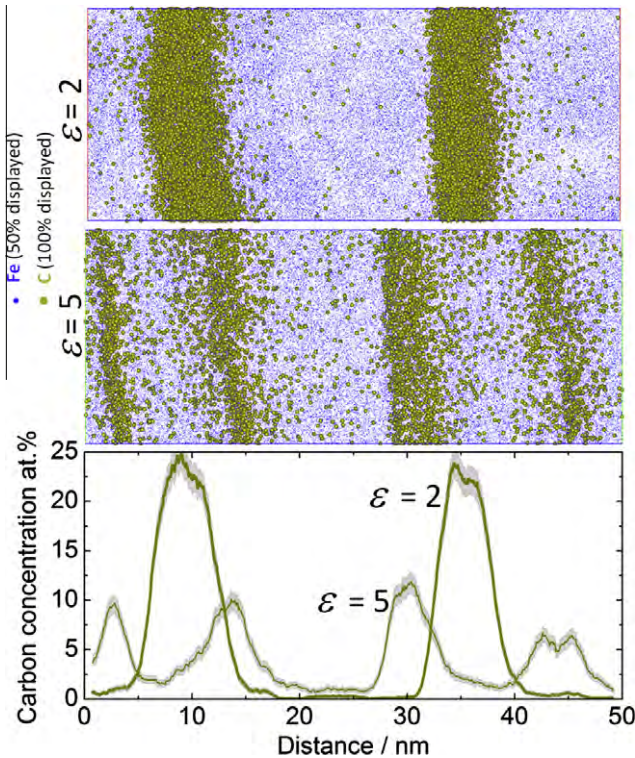
Fig. 4. Atom maps of the selected volume of $4 \times 20 \times 50$ nm^3 in the cold-drawn pearlitic wires at $\epsilon = 2$ (upper) and $\epsilon = 5$ (middle). The large yellow dots and the small blue dots represent carbon (100% shown) and iron (50% shown), respectively. The bottom figure shows the corresponding 1D carbon concentration profiles along the direction perpendicular to the lamellar interfaces (also the probing direction). The error bars are marked in gray.

Fig. 6. Carbon concentrations in the cementite as a function of lamella thickness.

Fig. 7. Comparison of the estimated carbon concentrations with that measured in the regions with a carbon concentration lower than 7 at.%. The measurement errors are within $\pm 0.03\%$.

4.1. Evolution of dislocation structure in ferrite

The dislocation densities measured for the pearlite wire by using X-ray line profile analysis vary from a minimum value of $\rho = 7.8 \times 10^{14}$ m^{-2} at $\epsilon = 0$ (as-patented) to a maximum value of 1.4×10^{16} m^{-2} at $\epsilon = 5$ [40]. These values correspond to an average dislocation spacing $\rho^{-0.5}$ of ~35 and ~8 nm, respectively. The mean free path of dislocations is proportional to the average dislocation spacing. For a safe estimate, if we take the proportionality constant as 10, the mean free paths turn out to be ~350 and ~80 nm, which are larger than the interlamellar spacings of ~60 and ~20 nm in each material, respectively. A similar estimate was also made by Gil Sevillano that the thickness of the ferrite lamellae are approximately 50 times lower than the mean free path of dislocations and less than 10 times the mean interdislocation distance that would develop under free gliding conditions [41]. This means that the formation of a dislocation structures in the ferrite channel, such as a cell or subgrain, is not likely because the probability of dislocation interaction is low.
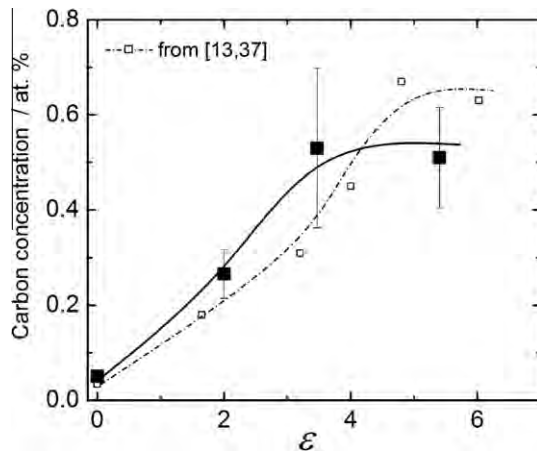

Fig. 5. Carbon concentrations in ferrite as a function of wire strain. Literature data are taken from Ref. [13,37].

is partly due to the plastic deformation occurring inside the cementite phase [2], and partly due to chemical decomposition as described in Section 3. In Section 3.4 we found cell/low-angle grain boundaries in ferrite at which the dissolved carbon atoms are segregated. We first discuss the possibility of the formation of cell/grain structures in ferrite.
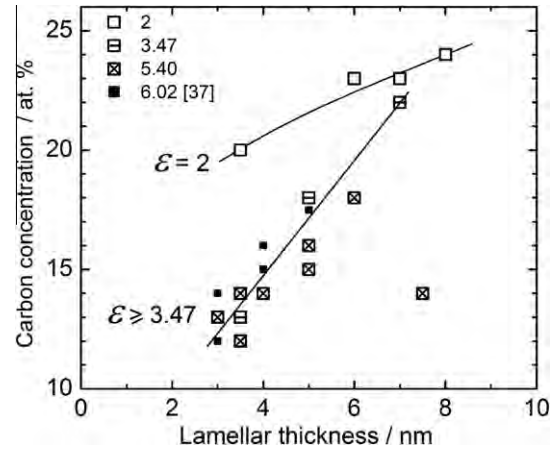
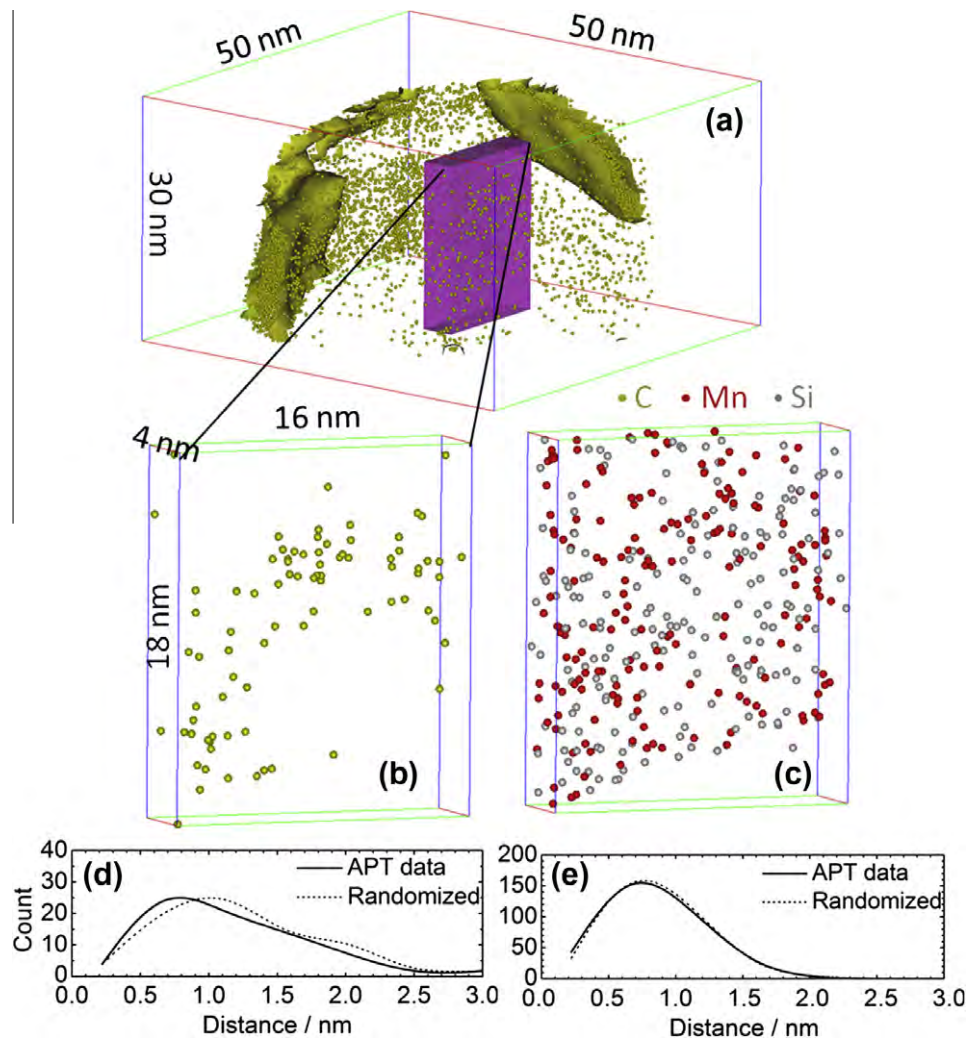Fig. 8. (a) 3D map of carbon atoms with an isoconcentration surface drawn at 7 at.% C for the pearlitic steel wire at $\epsilon = 0.93$. Only 50% of carbon atoms are displayed. (b) The distribution of C in the ROI taken from (a). 100% of the detected carbon atoms are displayed. (c) Analogue of (b) for Mn (red) and Si (gray). The blank area at the bottom is due to lack of material at the specimen tip. (d) Nearest-neighbor distance distributions between the carbon atoms. (e) As (d) for Mn and Si atoms.

Let us consider this problem in 3D space (Fig. 12). Similar to the schematics shown in Ref. [42], consider a general case that the slip plane of dislocations is inclined to the drawing direction and also to the normal direction of the cementite lamellae. At the interface between ferrite and cementite, dislocations can be nucleated provided that there is a mismatch in the elastic moduli of the two phases, and provided that some heterogeneities are present along the interface, which act as stress concentrators [43]. Regarding the dislocation sources, here we consider two possible mechanisms of dislocation multiplication for pearlite with narrow interlamellar spacings as shown in Fig. 12. In contrast to the Frank–Read source, which consists of two pinned ends (see Fig. 12a), the bulging mechanism does not involve any fixed source size. Instead, dislocations bulge out into the ferrite from lamellar interfaces [43] (see Fig. 12b). Gil Sevillano [41] proposed interfacial and intraphase dislocation sources, where dislocations glide between two impenetrable interfaces and within the interlamellar channels, respectively. Such

types of dislocation sources may dominate for the pearlite with coarse interlamellar spacings, because the critical stress for the corresponding configuration is low, and therefore preferable.

Since the mean free path of dislocations is larger than the lamellar spacing, the dislocation segment which reaches the opposite cementite plate must get stored there (see the cementite plate on the top). A further movement of the dislocation segments (corresponding to a further expansion of the dislocation loop) is only possible when the Orowan stress due to the line tension of the dislocation is overcome. The Orowan stress is inversely proportional to the interlamellar spacing. When the interlamellar spacing is sufficiently small, the Orowan stress can be so high that a further movement becomes difficult and the free dislocation segments will get stored in the ferrite.

Associated with the dislocation bulging, when the free segments tend to extend out of the narrow channel, a high Orowan stress has to also be reached, which leads to the storage of free dislocation segments in the ferrite. There-
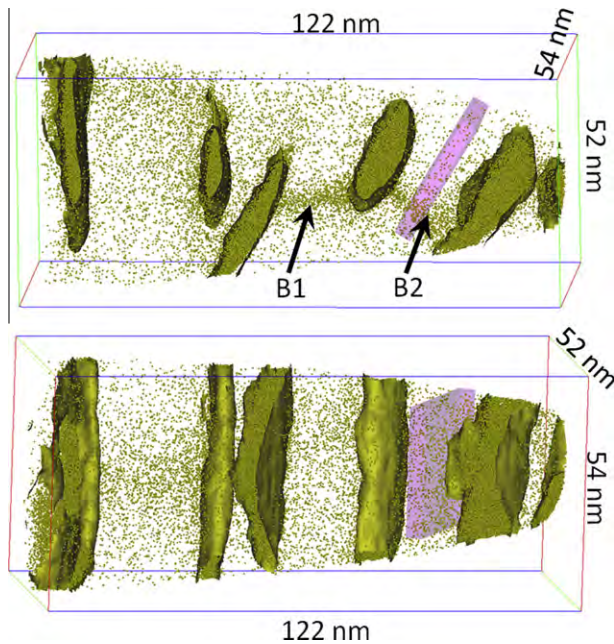
Fig. 9. 3D carbon atom maps with an isoconcentration surface drawn at 7 at.% Carbon for the pearlitic wire at $\epsilon = 2$. Top and bottom images show two side views (rotated 90° with respect to each other) of cementite lamellae, respectively. Only 50% of carbon atoms are displayed. The two grain boundaries B1 and B2 with carbon segregation are marked by the arrows. The detailed 3D map of the region of interest (pink box) with a volume of $30 \times 30 \times 4 nm^3$ is shown in Fig. 10.

Consider that dislocations with the same Burgers vector but opposite sign can be nucleated from opposite interfaces, the dislocation wall may also contain dislocations of different sign. Thus the wall could be a cell boundary or a grain boundary depending on the net sign of the dislocations involved. This mechanism can explain the formation of cell/subgrain boundaries, such as at positions B1 and B2 as shown in Fig. 9.

4.2. Segregation of carbon atoms at the lattice defects in ferrite

Based on literature data, Gavriljuk [22] excluded the possibility of formation of solid solution when cementite decomposes. Instead, he suggested that the dissolved carbon atoms are mainly located at the dislocations that are stored at the ferrite–cementite interface. The dislocation mechanism discussed above supports this analysis. However, we further suggested that dislocation walls can be formed inside ferrite and we assume that the dissolved carbon atoms can also be segregated to these new interfaces. This suggestion is supported by the 3D carbon atom map shown in Figs. 10 and 11. These results are consistent with the fact that the binding energy between dislocations and carbon atoms is higher than that between carbon atoms and iron in cementite [24–26]. Therefore, the distribution of carbon atoms is closely related to the distribution of dislocations. As discussed above, a heterogeneous dislocation structure forms in the ferrite lamellae, which consequently leads to an inhomogeneous distribution also of carbon in the ferrite.

Recently, Kobayashi et al. [44] reported an anomalous distribution of carbon atoms in ferrite of heat-treated

fore, in either case, dislocations will deposit not only at the interface but also inside the ferrite. When dislocations nucleated from parallel slip planes, a dislocation wall can be formed along the longitudinal direction of the lamellae.
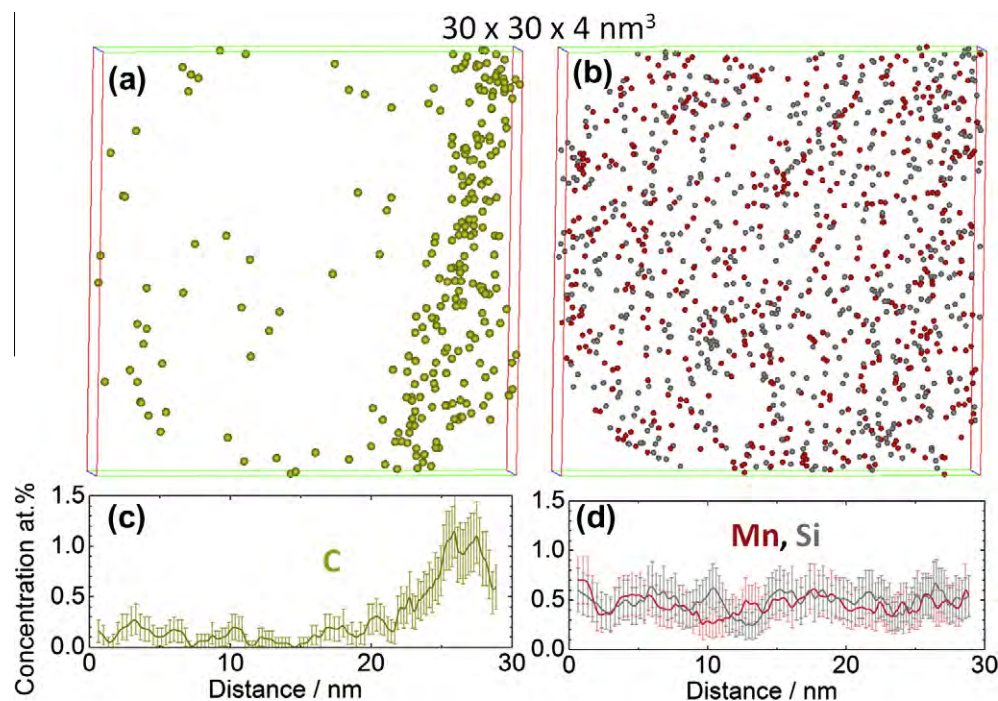

Fig. 10. Distribution of carbon atoms (a) as well as Mn (red) and Si (gray) atoms (b) in the ROI taken from Fig. 9 (ferrite region). All atoms detected are displayed. (c) and (d) show the corresponding 1D concentration profiles for carbon and Si and Mn, respectively.
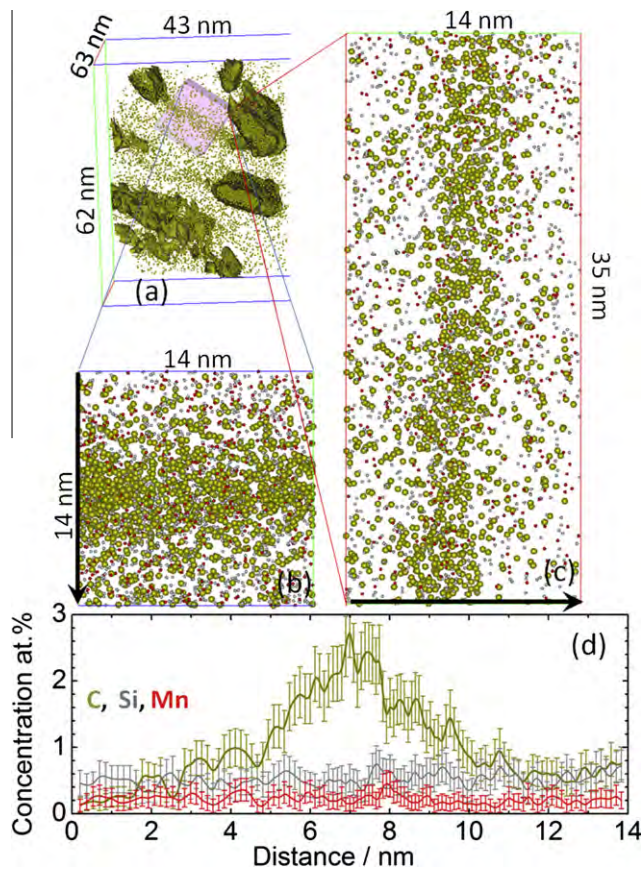
Fig. 11. (a) Part of the 3D carbon atom map with an isoconcentration surface at 7 at.% C for wires at $\epsilon = 5.4$. (b) and (c) Front and side views, respectively, of the atom maps for the ROI taken from (a). The yellow, red and gray dots represent C, Mn and Si atoms, respectively. (d) 1D concentration profiles for the three elements shown in (b) and (c) (fixed count of 5000 atoms) along the direction (marked with the black arrows) perpendicular to the carbon-enriched boundary.

Fig. 12. Schematic diagram explaining the formation of dislocation cell structures in the ferrite modified after Ref. [42]. The slip plane of the dislocations is inclined to the cementite lamellae and the drawing direction. Dislocations may be emitted from Frank–Read sources (a) and according to a bulge mechanism [43] (b).

(773 K for 5 h) pearlitic wire, where carbon atoms were always enriched in certain crystallographic directions [44]. They attribute this enrichment to the difference of the trajectory between iron and solute carbon atoms during their flight in the APT measurement. However, similar observations could not be made in the present investigations. Recent LEAP analyses done in our group on cold-drawn wires annealed at 400 °C for 0.5 h clearly showed that carbon atoms are preferentially located at the boundaries of hexagonal (sub) grains in the ferrite. This means that the detected carbon segregation in this work reflects a real physical process.

It is known that the cell or grain size is dependent on the stress and the strain (before a steady state of deformation is reached under given deformation conditions). Thus, further wire drawing leads to additional work hardening, which causes a finer dislocation structure. In other words, the more cell or grain boundaries are formed upon further straining, the more segregation of carbon atoms in the ferrite is possible. This may explain the fact that the carbon concentration in ferrite increases with drawing strain (see Fig. 5). Following this line of argument, the saturation of

carbon atoms at higher strains should be coupled to the saturation in the dislocation density that can be stored in the ferrite. In the recent measurements of the dislocation density performed with X-ray line profile analysis for the same materials, it was indeed found that the increase of the dislocation density with strain becomes significantly slower at high strains ($\epsilon \approx 4$) [40].

4.3. Thermodynamics and kinetic mechanisms of cementite decomposition

There are two principal interpretations for cementite decomposition in the literature. Based on our results and those found in the literature, we consider that the interaction between carbon atoms and dislocations is likely to be the mechanism responsible for cementite decomposition. Let us start with reviewing the available findings. First, cold working introduces a high density of dislocations at the interfaces between ferrite and cementite [43,45]. Second, the interaction between dislocations and carbon atoms exhibits a higher binding energy [24] than that between carbons and iron atoms in cementite [25,26]. Third, carbon atoms segregate at cell/grain boundaries in ferrite [46] (see also Section 3 above). Fourth, the saturation of the carbon

concentration in the ferrite with strain is associated with a slow increase of the dislocation density at high strains.

These results suggest that the dislocation activity and cementite decomposition are associated phenomena and occur simultaneously during plastic deformation. When the dislocation loops expand from one interface to the opposite one, they also drag the carbon atoms out of the cementite lattice and form a Cottrell atmosphere during motion. The dislocations in ferrite form dislocation walls, which connect the neighboring cementite plates as shown in Figs. 10 and 11 and are decorated with an enhanced amount of carbon atoms.

According to this mechanism, the degree of cementite decomposition is determined by the dislocation structure and its evolution, which in turn is controlled by the drawing stress and strain. A higher degree of plastic deformation introduces a higher density of dislocations which form more cell/grain boundaries. As a result, cementite decomposition is more severe. This leads to a thinning of cementite plate with a reduced carbon concentration (see Fig. 6) and an enhancement of the average carbon concentration in ferrite (see Fig. 5). Gradual saturation in the dislocation structure leads to the saturation in the interaction between dislocations and cementite lamellae. Thus, the relation between the carbon concentration and the thickness of cementite lamellae becomes strain independent (see Fig. 6). For the cementite lamellae with a thickness larger than ~8 nm, as shown in Fig. 6, dislocations may not be able to approach the center of the lamellae even after the highest drawing strain. This means that carbon atoms inside the cementite cannot reach the ferrite dislocations, while carbon near the interfaces can leave the cementite and be stored at the dislocations in the ferrite. Thus, the influence of the neighboring ferrite dislocations saturates upon further deformation, as the dislocation density in the ferrite saturates.

In addition to the elementary interaction between carbon atoms and lattice dislocations in the ferrite, a trans-phase dislocation-shuffle mechanism may act as a kinetic mechanism for the decomposition of cementite [47,48]. According to the mechanism discussed in Ref. [47], provided that dislocations penetrate from ferrite into cementite on more than one active slip system, the shearing of atomic planes along mutually inclined directions can create interface steps and embed small cementite particles in ferrite. Such tiny cementite particles can be further cut by dislocations gliding through them, which enhances the energy of the particles through the Gibbs–Thomson effect so that they finally dissolve. In principle, this mechanism can explain the large deformation-driven transport of carbon from cementite into the ferrite against the thermodynamic equilibrium conditions. However, the effect of this mechanism may be conditioned by several factors, e.g. the magnitude of the resolved shear stress of the dislocations approaching the interface on the activated system, the degree of misorientation between the active slip planes on either side of the interface and the energetic preferability

of the resulted configuration which can, for example, be influenced by the residual dislocation content at the interface through the selection of a transmitted slip system in the body-centered cubic phase [49]. Misra et al. suggested that transmission of dislocations across interfaces is only likely to occur at nanometer length scales (e.g., ~1–2 nm layer thickness) [50]. The observed broken cementite lamella in pearlite [51] may be an indicator of penetration of ferrite dislocations through the thin cementite lamella [48].

5. Conclusions

Cementite decomposition and the associated mechanical alloying in cold-drawn pearlitic steel wires was studied as a function of true drawing strain by using LEAP in conjunction with TEM. The carbon concentrations in ferrite, cementite, and the entire analyzed volumes were measured systematically by applying a decomposition algorithm for overlapping mass-to-charge peaks of carbon. Cementite decomposition was found to be promoted by plastic deformation. However, the decomposition of cementite and the carbon concentration in ferrite both saturate after a true drawing strain of 3.47, and thus the lamellar structure exists even at a drawing strain of up to 5.4. Strong indications for the formation of cell–grain boundaries in ferrite, at which most of carbon atoms in ferrite segregate, were observed. Based on these findings, we suggest that the dislocation density in the ferrite is probably the mechanism underlying cementite decomposition.

Appendix A. Simple estimate of the carbon balance after cementite decomposition

A.1. C-concentration in the cementite

Each cementite lamella is cut by the same number of dislocations per area A which removes a total of n mol C per area from the carbide. Then the C-concentration changes from 0.25 to x according to the following balance:

$$x\frac{Ad}{\Omega_C} = 0.25\frac{Ad}{\Omega_C} - \Delta nA \tag{1}$$

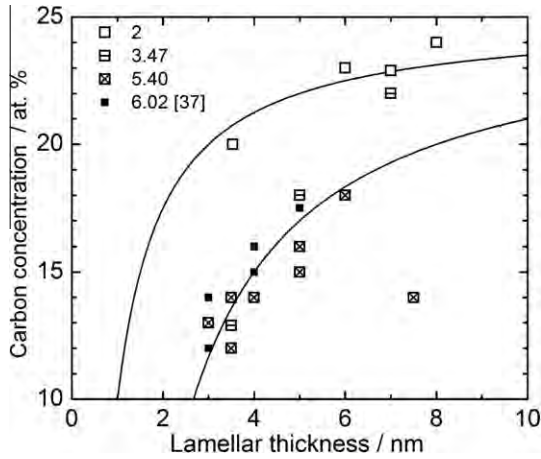where d is the thickness of the lamella and Ω_C the molar volume of cementite. Rearranging yields:

Fig. A.1. C-concentration in cementite x after deformation as a function of the lamella thickness d. Lines are fit to Eq. (2).
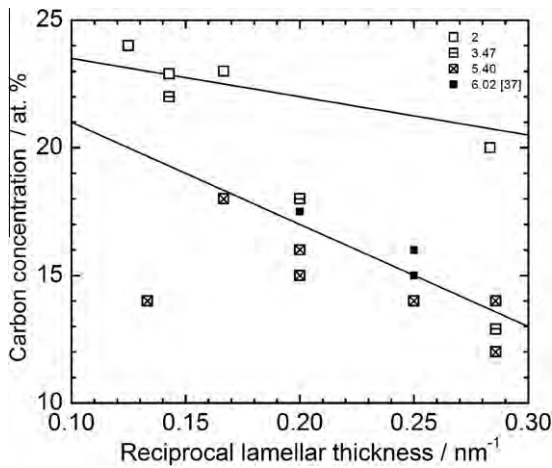

Fig. A.2. C-concentration vs. d^{-1} according to Eq. (2).

$$x = 0.25 - \Delta n \frac{\Omega_C}{d} \qquad (2)$$

As shown in Fig. A.1, this equation agrees well with the experimental data. The process of C-removal stops at large strains, when the dislocations are entering the cementite from the ferrite with the same amount of carbon as they take out when they leave the cementite to enter the ferrite.

A.2. C-concentration in the ferrite

In ferrite, the released carbon Δn_{tot} per area A for a number of lamellae, Z, is given by:

$$A\Delta n_{\text{tot}} = Z\Delta nA \qquad (3)$$

Z is obtained from the total volume of cementite divided by the average volume of one lamella:

$$Z = \frac{V_{\text{Cem}}}{Ad_{\text{aver}}} = \frac{x_w V_w}{25Ad_{\text{aver}}} = \frac{x_w Ad_w}{25Ad_{\text{aver}}} = \frac{x_w d_w}{25d_{\text{aver}}} \qquad (4)$$

where d_{aver} is the average thickness of cementite lamella and x_w and d_w are the C-concentration and thickness of the wire:

$$\Delta n_{\text{tot}} = \Delta n \frac{x_w d_w}{25d_{\text{aver}}} \qquad (5)$$

This will change the C-concentration in the ferrite to:

$$\Delta c_{\text{fer}} = \frac{\Delta n_{\text{tot}} A\Omega_{\text{fer}}}{Ad_w} = \Delta n \frac{x_w \Omega_{\text{fer}}}{25d_{\text{aver}}} = \frac{slope}{\Omega_C} \frac{x_w \Omega_{\text{fer}}}{25d_{\text{aver}}} \qquad (6)$$

where slope is the slope of the concentration vs. d^{-1} plot, x_w is the total C-concentration of the wire in at.% and Ω_{fer} is the atomic volume of ferrite. Using $\Omega_C = \Omega_{\text{fer}}$, slope = 40 at.% nm (from Fig. A.2 for larger strains) $d_{\text{aver}} = 4$ nm and $x_w = 3.66$ at.% yields $\Delta c_{\text{fer}} = 1.46$ at.% C. For $\epsilon = 2$ the slope is 15 at.% nm (from Fig. A.2 for lower strain), yielding $\Delta c_{\text{fer}} = 0.55$ at.% C.

References

[1] Takahashi T, Ochiai I, Tashiro H, Ohashi S, Nishida S, Tarui T. Nippon Steel Tech Rep 1995;64:45.
[2] Landford G. Metall Trans A 1977;8:861.
[3] Hong MH, Reynolds Jr WT, Tarui T, Hono K. Metall Mater Trans A 1999;30:717.
[4] Hono K, Ohnuma M, Murayama M, Nishida S, Yoshie A. Scripta Mater 2001;44:977.
[5] Taniyama A, Takayama T, Arai M, Hamada T. Scripta Mater 2004;51:53.
[6] Goto S, Kirchheim R, Al-Kassab T, Borchers C. Trans Nonferrous Met Soc China 2007;17:1129.
[7] Borchers C, Al-Kassab T, Goto S, Kirchheim R. Mater Sci Eng A 2009;502:131.
[8] Embury JD, Fisher RM. Acta Metall 1966;14:147.
[9] Gridnev VN, Gavrilyuk VG, Dekhtyar IY, Meshkov YY, Nizin PS, Prokopenko VG. Phys Status Solidi A 1972;14:689.
[10] Read HG, Reynolds Jr WT, Hono K, Tarui T. Scripta Mater 1997;37:1221.
[11] Tarui T, Takahashi T, Ohashi S, Uemori R. Iron Steelmaker 1994;21:25.
[12] Tarui T, Takahashi J, Tashiro H, Nishida S. In: Paris HG, Kim DK, editors. Processing and applications of metal wires. Warrendale, PA: TMS; 1996. p. 87.
[13] Maruyama N, Tarui T, Tashiro H. Scripta Mater 2002;46:599.
[14] Tarui T, Maruyama N, Takahashi J, Nishida S, Tashiro H. Nippon Steel Tech Rep 2005;91.
[15] Danoix F, Julien D, Sauvage X, Copreaux J. Mater Sci Eng A 1998;250:8.
[16] Sauvage X, Copreaux J, Danoix F, Blavette D. Philos Mag A 2000;80:781.
[17] Sauvage S, Lefebvre W, Genevois C, Ohsaki S, Hono K. Scripta Mater 2009;60:1056.
[18] Yamada Y. Trans ISIJ 1976;16:417.
[19] Gridnev VN, Nemoshkalenko VV, Meshkov YY, Gavrilyuk VG, Prokopenko G, Razumov ON. Phys Status Solidi A 1975;31:201.
[20] Nam WJ, Bae CM, Oh SJ, Kwon SJ. Scripta Mater 2000;42:457.
[21] Belous MV, Cherepin VT. Fiz Metall Metalloved 1961;12:685.
[22] Gavriljuk VG. Scripta Mater 2001;45:1469.
[23] Gavriljuk VG. Mater Sci Eng A 2003;345:81.
[24] Cochardt AW, Schoek G, Wiedersich H. Acta Metall 1955;3:533.
[25] Johnson RA, Diens GI, Damask AC. Acta Metall 1964;12:125.
[26] Johnson RA. Acta Metall 1967;15:513.
[27] Languillaume J, Kapelski G, Baudelet B. Acta Mater 1997;45:1201.
[28] Kelly TF, Miller MK. Rev Sci Instrum 2007;78:031101.
[29] Takahashi J, Tarui T, Kawakami K. Ultramicroscopy 2009;109:193.
[30] Sauvage X, Thilly L, Blavette D. J Phys IV France 2001;11:27.
[31] Miller MK, Russell KF, Thompson GB. Ultramicroscopy 2005;102:287.

[32] Miller MK, Russell KF, Thompson K, Alvis R, Larson DJ. Microsc Microanal 2007;13:428.

[33] Thompson K, Lawrence D, Larson DJ, Olson JD, Kelly TF, Gorman B. Ultramicroscopy 2007;107:131.

[34] Takahash J, Kawakami K, Yamaguchi Y. Microsc Microanal 2009;15(Suppl 2):3036.

[35] Sha W, Chang L, Smith GDW, Cheng L, Mittemeijer EJ. Surf Sci 1992;266:416.

[36] Miller MK, Beaven PA, Brenner SS, Smith GDW. Metall Trans A 1983;14:1021.

[37] Li YJ, Choi P, Borchers C, Chen YZ, Goto S, Raabe D, et al. Ultramicroscopy 2011. doi:10.1016/j.ultramic.2010.11.010.

[38] Gavriljuk VG. Carbon distribution in steel (in Russian). Kiev: Naukova dumka; 1987.

[39] Zelin M. Acta Mater 2002;50:4431.

[40] Chen YZ, Csiszár G, Cizek J, Westerkamp S, Borchers C, Ungr T, et al. Unpublished results; 2010.

[41] Gil Sevillano J. J Phys III 1991;1:967–88.

[42] Schastlivtsev VM, Yakovleva IL, Karkina LE, Khlebnikov YV, Tabatchikova TI, Urtsev VN. Russ Phys J 2004;47:807.

[43] Janecek M, Louchet F, Doisneau-Cottignies B, Bréchet Y, Guelton N. Philos Mag A 2000;80:1605.

[44] Kobayashi Y, Takahashi J, Kawakami K. Ultramicroscopy 2011. doi:10.1016/j.ultramic.2011.01.016.

[45] Embury JD, Hirth JP. Acta Metall Mater 1994;42:2051.

[46] Waugh AR, Paetke S, Edmonds DV. Metallography 1981;14:237.

[47] Raabe D, Ohsaki S, Hono K. Acta Mater 2009;57:5254.

[48] Raabe D, Choi P, Li YJ, Kostka A, Sauvage X, Lecouturier F. MRS Bull 2010;35:982.

[49] Sinclair CW, Embury JD, Weatherly GC. Mater Sci Eng A 1999;272:90.

[50] Misra A, Hirth JP, Hoagland RG. Acta Mater 2005;53:4817.

[51] Sauvage X, Guelton N, Blavette D. Scripta Mater 2002;46:459.

Evolution of strength and microstructure during annealing of heavily cold-drawn 6.3 GPa hypereutectoid pearlitic steel wire

Y.J. Li [a,b,*], P. Choi [b], S. Goto [c], C. Borchers [a], D. Raabe [b,*], R. Kirchheim [a,b]

[a] *Institut für Materialphysik, Georg-August-Universität Göttingen, Friedrich-Hund-Platz 1, D-37077 Göttingen, Germany*
[b] *Max-Planck Institut für Eisenforschung, Max-Planck-Str. 1, D-40237 Düsseldorf, Germany*
[c] *Department of Materials Science and Engineering, Faculty of Engineering and Resource Science, Akita University, Tegata Gakuencho, Akita 010-0852, Japan*

Abstract

Hypereutectoid steel wires with 6.35 GPa tensile strength after a cold-drawing true strain of 6.02 were annealed between 300 and 723 K. The ultrahigh strength remained upon annealing for 30 min up to a temperature of 423 K but dramatically decreased with further increasing temperature. The reduction of tensile strength mainly occurred within the first 2–3 min of annealing. Atom probe tomography and transmission electron microscopy reveal that the lamellar structure remains up to 523 K. After annealing at 673 K for 30 min, coarse hexagonal ferrite (sub)grains with spheroidized cementite, preferentially located at triple junctions, were observed in transverse cross-sections. C and Si segregated at the (sub)grain boundaries, while Mn and Cr enriched at the ferrite/cementite phase boundaries due to their low mobility in cementite. No evidence of recrystallization was found even after annealing at 723 K for 30 min. The stability of the tensile strength for low-temperature annealing (<473 K) and its dramatic drop upon high-temperature annealing (>473 K) are discussed based on the nanostructural observations.
© 2012 Acta Materialia Inc. Published by Elsevier Ltd. All rights reserved.

Keywords: Pearlitic steel; Ultrahigh strength; Atom probe tomography; Annealing; Grain boundary segregation

1. Introduction

Cold-drawn, hypereutectoid pearlitic steel wires show maximal tensile strength above 5 GPa [1], thus making them the strongest bulk nanostructured materials. Although pearlite has a large potential in engineering applications, the microstructural origin of its extreme strength is not well understood. It has been shown by several authors that cold drawing not only strengthens pearlite by refining the lamellae structure [2–5], but also simultaneously causes partial chemical decomposition of cementite [6–18] and a structural transition from crystalline to amorphous cementite

[9,13,14]. The deformation-induced decomposition and microstructural change of cementite is closely related to several other phenomena, such as a strong redistribution of carbon and other alloy elements like Si and Mn in both cementite and ferrite; a variation of the deformation accommodation at the phase interfaces due to a change in the carbon concentration gradient at the interfaces; mechanical alloying; and a further reduction of the deformability of cementite when rendered amorphous. Since these phenomena occur at the atomic scale, the understanding of the strengthening mechanisms of cold-drawn hypereutectoid pearlitic wires can only be improved on the basis of atomic-scale investigations.

Taking a first step in this direction, we recently studied the redistribution of carbon in ferrite and cementite in ultrahigh-strength pearlitic steel wires for a wide range of (true) drawing strains between 0 and 6.02 using atom probe

---

* Corresponding authors. Address: Max-Planck Institut für Eisenforschung, Max-Planck-Str. 1, D-40237 Düsseldorf, Germany. Tel.: +49 211 6792853; fax: +49 211 6792333.
E-mail addresses: y.li@mpie.de (Y.J. Li), d.raabe@mpie.de (D. Raabe), rkirch@ump.gwdg.de (R. Kirchheim).

tomography (APT) [17,18]. In ferrite, we found that the carbon concentration increases with the drawing strain up to 3.47 and then saturates with further deformation. We found evidence of the formation of dislocation (sub)-grain boundaries in the ferrite lamellae and observed the segregation of carbon at ferrite dislocations and (sub)grain boundaries. In cementite, we found that the carbon concentration decreases with the thickness of the cementite lamellae. This finding gives a quantitative correlation between plastic deformation and cementite decomposition in cold-drawn pearlitic steel wires [17,18]. Furthermore, both the saturation of the carbon content in the ferrite and the discontinuation of further decomposition of cementite at high strains indicate the important role of dislocations during cementite decomposition. This is also supported by the direct observation of carbon segregation at ferrite dislocations and grain boundaries [17,18].

Nanostructured materials produced by severe plastic deformation are highly susceptible to grain coarsening upon heating, due to the large density of dislocations and grain boundaries. However, little attention has been paid so far to the thermal stability of the nanostructure of heavily cold-deformed pearlitic wires [9,19–21] and its effect on the mechanical properties. In this work, we study the changes in the nanostructure of a heavily cold-drawn hypereutectoid pearlitic steel wire upon annealing in order to elucidate the mechanism leading to the ultrahigh strength of cold-drawn pearlitic steel wires. The wires studied here were subjected to the most extreme deformation by cold drawing to a true drawing strain of $\epsilon = 6.02$ and exhibit the highest tensile strength achieved to date (6.35 GPa). The tensile strength was measured as a function of the annealing temperature between 423 and 723 K and of the annealing time. The samples were characterized by means of APT in conjunction with transmission electron microscopy (TEM). APT yields three-dimensional elemental maps with near-atomic resolution. This technique is a key to the current study as it allows us to identify the carbon distribution in the drawn and heat-treated pearlite samples [16,22–28]. A local electrode atom probe (LEAP 3000X HR^{TM}, Cameca Instruments) was used, which provides a larger field of view, faster data acquisition rates and higher mass resolution [29–32] compared to conventional atom probes and thus yields compositional data with high accuracy. We surprisingly observed hexagonal (sub)grains in ferrite after annealing, where carbon is segregated to (sub)grain boundaries and spheroidized cementite particles are preferentially located at triple junctions. In addition, the redistribution of other alloying elements, such as Si, Mn and Cr, upon annealing is also quantified and discussed from the viewpoint of the kinetic barriers in terms of the differences in diffusion coefficients between the two abutting phases (ferrite and cementite). On the basis of our experimental observations, we discuss the influence of annealing temperature T and time, and also of the alloying elements and their respective redistribution on the drop in tensile strength upon heat treatment.

2. Experimental

2.1. Material and experimental methods

The material studied in this work was a pearlitic steel wire of hypereutectoid composition (Fe–0.98C–0.31Mn–0.20Si–0.20Cr–0.01Cu–0.006P–0.007S in wt.% and Fe–4.40C–0.30Mn–0.39Si–0.21Cr–0.003Cu–0.01P–0.01S in at.%), provided by Suzuki Metal Industry Co., Ltd. The as-deformed wires were in a cold-drawn state, with a true strain of $\epsilon = 6.02$. Samples taken from this material were annealed for 30 min between 423 and 723 K, at 50 K intervals. Tensile strength, APT and TEM measurements were taken on the as-deformed and annealed wires. The tensile strength was measured with a Dia Stron LEX 810 device using an initial strain rate of $\dot{\epsilon}_0 = 1.16 \times 10^{-3}$ s^{-1}.

The local electrode atom probe was used to analyze the nanostructural changes and the three-dimensional (3-D) elemental distributions upon annealing. The measurements were performed in voltage mode at 70 K, with a pulse fraction of 15%, a pulse repetition rate of 200 kHz and a detection rate of 0.005 atoms per pulse. APT samples perpendicular to the wire axis were prepared using a dual-beam focused ion beam (FEI Helios NanoLab 600TM) according to the procedure described in Ref. [15]. Reconstructions of the APT data were made using standard parameters for the image compression factor (1.65) and the evaporation field (33 V nm^{-1}), with an efficiency of the detector of 0.37. The final specimen tip radii (after APT measurements) were also taken into account for the reconstructions. TEM samples were prepared using the focused ion beam lift-out method. The sample preparation was done with 30 kV Ga ions, finishing the last step with 5 kV Ga ions. We used a Philips CM30 instrument at an acceleration voltage of 300 kV.

2.2. Mass spectrum analyses of atom probe data

The assignment of ion peaks in a mass spectrum of cold-drawn pearlitic steel wire has been addressed previously [8,15,18]. A mass spectrum of an annealed wire with an initial drawing strain of 6.02 is shown in Fig. 1a. All peaks due to Fe, alloy elements (C, Si, Cr and Mn) as well as impurities like P and S are assigned. As reported in Refs. [17,18] for cold-drawn wires, the mass spectra of ferrite (Fig. 1b) and cementite (Fig. 1c) also reveal the presence of the peak at 24.5 Da in cementite only, which means that 100% of the peak at 24 Da is due to C_2^+ in the ferrite, while a mixture of ions from C_2^+ and C_4^{2+} in the cementite contribute to this peak. A peak deconvolution algorithm (supplied by the software IVAS, Cameca Instruments) taking into account the isotope ratios of C was applied to the peak at $m/n = 24$ Da. The result shows that less than 50% of the peak is due to C_4^{2+} in the cementite, while for the cold-drawn wires the contribution from C_4^{2+} exceeds 80% [17]. It is reported that the fractions of carbon molecular ions change with the APT acquisition conditions, e.g. temperature,
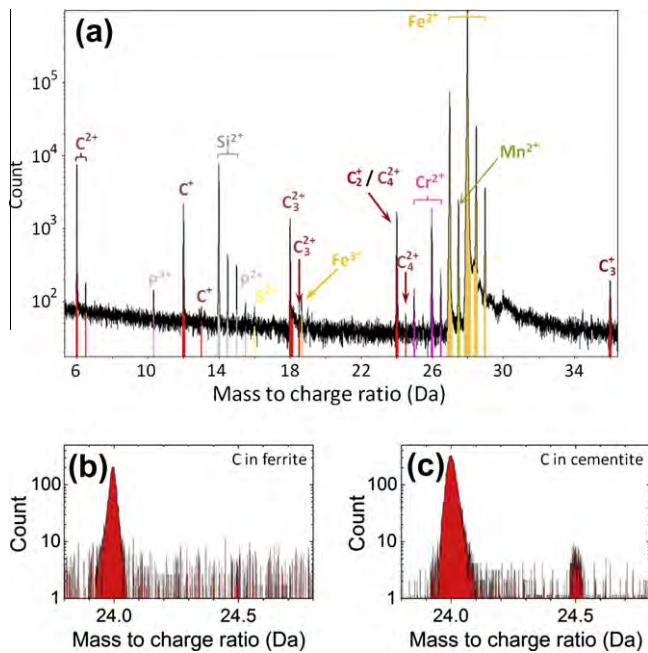
Fig. 1. (a) Mass spectrum of a cold-drawn ($\epsilon = 6.02$) wire after annealing at 673 K for 30 min. Peaks ascribed to C, Si, Cr, Mn and Fe are marked in red, gray, pink, green and yellow, respectively. (b and c) Mass spectra for ferrite and cementite, respectively. Note the presence of the peak of 24.5 Da only in the cementite.

Fig. 2. Tensile strength as a function of annealing temperature for an annealing time of 30 min for cold-drawn hypereutectoid pearlitic steel wires. The red circles mark the annealing conditions for which APT measurements were performed.

Fig. 3. Tensile strength as a function of annealing time at various temperatures for cold-drawn hypereutectoid pearlitic steel wires. The red circles mark the annealing conditions for which HRTEM studies were performed.

pulse fraction and evaporation rate [33]. It might be possible that the different material states (e.g. deformed and annealed) also influence the ratio of field-evaporated carbon molecules. As C_2^+ mainly contributes to the peak at 24 Da according to the peak deconvolution analysis, this peak was assigned as C_2^+ for atom maps of the annealed samples.

3. Results

3.1. Evolution of tensile strength upon annealing

Fig. 2 shows the tensile strength as a function of the annealing temperature. At room temperature the as-deformed material exhibits a tensile strength of 6.35 GPa, which, to the best of our knowledge, makes it the strongest pearlitic steel wire available today. The ultrahigh tensile strength remains after annealing at 423 K for 30 min. Beyond this temperature, the tensile strength decreases approximately linearly with the annealing temperature. The evolution of the tensile strength with annealing time shown in Fig. 3 indicates that the dramatic drop in tensile strength mainly occurs within the first 2–3 min of the annealing process. After this short time interval, the tensile strength remains approximately constant at a relatively low temperature of 523 K. Even for the highest temperature of 723 K, the tensile strength decreases only slightly with further annealing time. This suggests that the underlying structural changes take place during the early annealing stage. The large circles in Figs. 2 and 3 mark the annealing conditions

under which the nanostructure and the distribution of alloy elements in the deformed and annealed wires were studied by APT and high-resolution (HR) TEM.

3.2. Evolution of microstructure upon annealing

APT results on the as-deformed and the 473 K and 673 K heat-treated states are displayed in Fig. 4. The atom maps of the as-deformed material (Fig. 4a) clearly show that a lamellar structure consisting of carbon-depleted (ferrite) and -enriched (cementite) regions still prevails after severe cold-drawing up to a strain of 6.02, although fragmentation of cementite lamellae can be observed. The lamellar structure remains stable after annealing at 473 K for 30 min (Fig. 4b). No cementite spheroidization occurs.
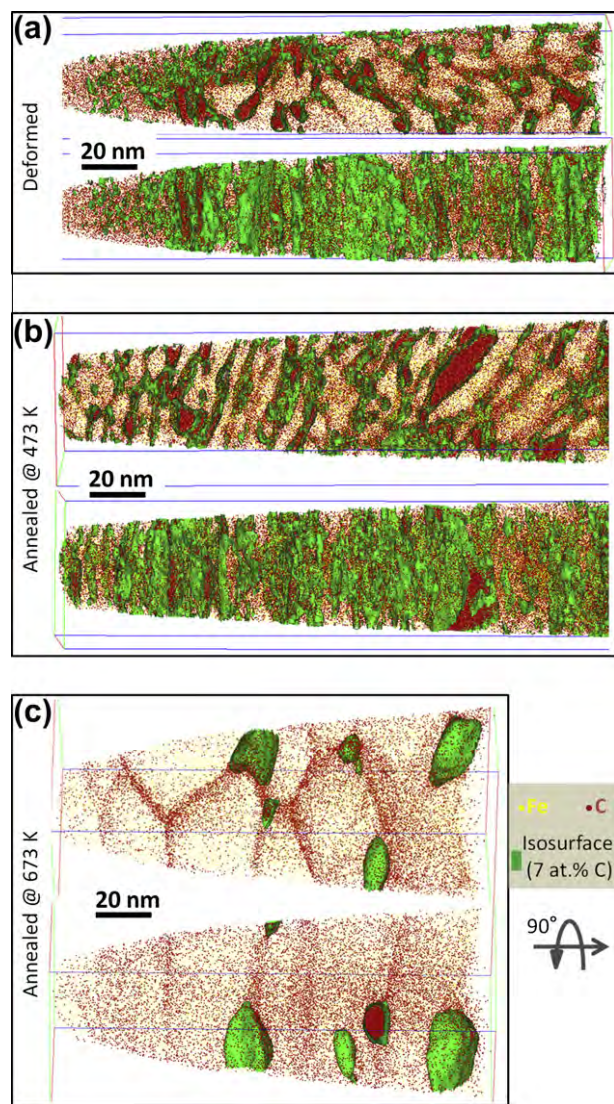
Fig. 4. 3-D carbon atom maps of hypereutectoid pearlitic steel wires with a cold drawing strain of $\epsilon = 6.02$: (a) as-deformed state; (b) annealed at 473 K for 30 min; and (c) annealed at 673 K for 30 min. The isoconcentration surfaces for 7 at.% carbon are shown in green. Only 30% of all carbon and 0.5% of all iron atoms are displayed. Both the cross-sectional (top) and longitudinal views (bottom) of the wires are shown.

However, Languillaume et al. observed speroidized cementite particles at 473 K [19]. Since the alloy elements, the initial strain and the annealing time of the pearlitic wire studied in Ref. [19] were different from those studied in this work, it is difficult to analyze the exact reasons for the different observations.

After heat treatment at 673 K for 30 min, strong microstructural changes occur. The original lamellar pearlitic structure is no longer visible; instead, a nearly equiaxed hexagonal (sub)grain structure has formed inside the ferrite (see Fig. 4c). The (sub)grain boundaries enclosing the carbon-depleted ferrite (sub)grains are decorated with carbon atoms. The (sub)grains exhibit an average grain size of 30–40 nm, which is about 2–3 times higher than the interlamellar spacing in the as-deformed wire [17,18]. Furthermore,

the cementite lamellae have undergone spheroidization and are mainly located at the triple junctions. Similar observations were made by TEM for pearlitic steel wires at true drawing strains of 3.5 after annealing for 1 h at 823 K [19], 4.22 for 1 h at 673 K [9] and 5 for 0.5 h at 723 K [20]. Closer observation of Fig. 4c shows that the grains are not equiaxed but, rather, elongated along the drawing direction, with longitudinal sizes above 70 nm. It is noted that the reconstruction of the APT data shown in Fig. 4c was done based on the final tip radius after APT measurement, and is hence reliable. This observation suggests that the relatively coarse (sub)grain structure observed in the ferrite is not due to recrystallization, as this mechanism would lead to equiaxed grains.

Fig. 5 shows TEM micrographs of pearlitic wires for the corresponding conditions marked in Fig. 3. Strong strain contrast due to heavy drawing can be observed from Fig. 5a. The phase boundaries between ferrite and cementite are blurred and nearly invisible. The observation in the cross-section of the wire (Fig. 5b) shows the typical curled ribbon-like lamellar structure around the wire axis [3,34,35]. As explained by Hosford [36], the $\langle 1\,1\,0\rangle$ fiber texture developed during wire drawing confines further slipping in each lamella to a plain strain state, and thus the compatibility of the neighboring grains can be maintained only by the bending of the grains around one another. This mechanism is referred to as curling [36–38]. The observation of fragmentation of cementite in Fig. 5b is consistent with the APT result shown at the bottom of Fig. 4a, where the cementite lamellae are curled and fragmented into numerous short segments and even small particles. This is direct evidence that cementite lamellae are capable of undergoing plastic deformation and even strain-induced fragmentation, as reported in Ref. [2,3]. Upon annealing at 523 K for 30 min, the lamellar structure is still preserved and no recrystallization occurs (Fig. 5c).

After annealing at 723 K (see Fig. 5d), the lamellar structure along the drawing direction is still visible, while cell/subgrain boundaries have formed in the ferrite and the cementite lamellae have undergone spheroidization. The ferrite cell/subgrains are elongated along the wire axis, in agreement with the APT observation at 673 K (Fig. 4c). In the direction perpendicular to the wire axis, the average subgrain size is below 80 nm.

3.3. Redistribution of carbon during annealing

Fig. 6 illustrates the carbon partitioning among the various phases or regions (ferrite, cementite and interface region) in the as-deformed and annealed samples, where the bulk carbon concentration is plotted against the cumulative (phase) volume fractions. In accordance with our previous works [17,18], the phases of ferrite and cementite, and the interface between them, are defined according to their carbon content (see also caption of Fig. 6), where the volume fraction of each phase can be estimated as the ratio of the total number of atoms in each phase to the total
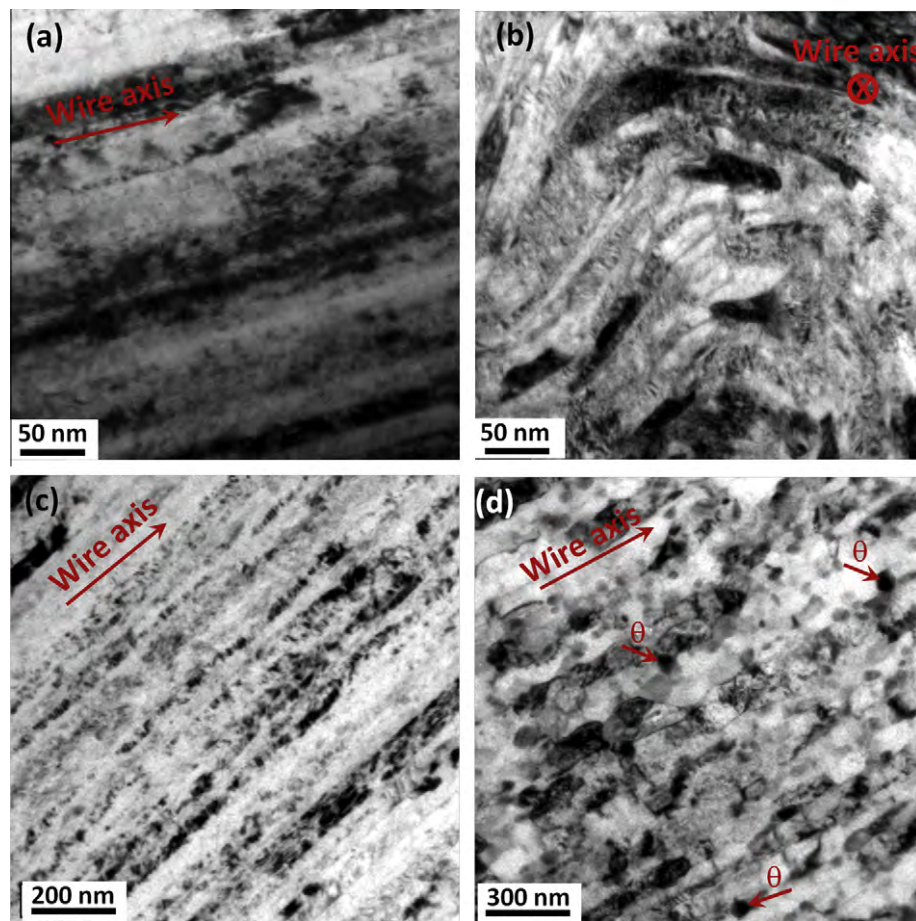
Fig. 5. TEM images of hypereutectoid pearlitic steel wires. (a and b) As-deformed ($\epsilon = 6.02$) states in longitudinal and transverse cross-sections of wires, respectively. (c and d) As-annealed states at 523 and 723 K for 30 min, respectively. The arrows mark the wire axis which is also parallel with the ferrite/cemetite interfaces. Some globular cementite particles (θ) are marked.
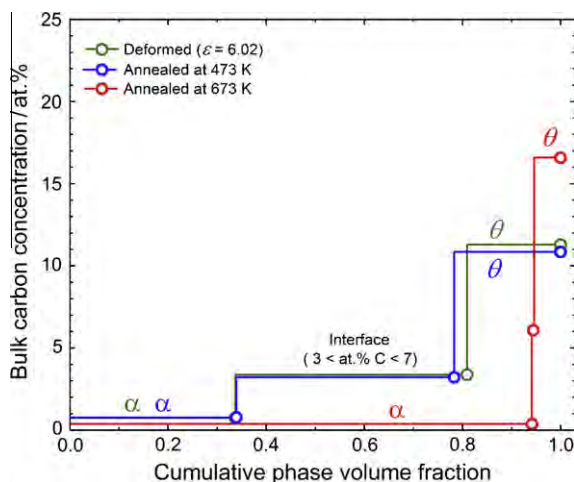
Fig. 6. Bulk carbon concentrations in the defined phase zones vs. volume fractions of the corresponding phase zones. Ferrite (α) and cementite (θ) are defined as the regions with carbon concentrations lower than 3 at.% and higher than 7 at.%, respectively. The region between the two phases is defined as the ferrite/cementite interface.

number of atoms in the whole sample. The result shows that, in the as-deformed sample, the carbon concentration

of 0.73 ± 0.006 at.% in the ferrite is far beyond the equilibrium value of several tens of atom ppm, while the carbon concentration in the cementite decreases to approximately half of the stoichiometric value. In addition, the large volume fraction of the interface characterized by an extended carbon concentration gradient suggests dissolution of carbon atoms from cementite to ferrite and a mechanical alloying process. After annealing at 473 K for 30 min, no significant redistribution of carbon atoms is found, since both the carbon concentrations and the volume fractions of all phases remain close to the values measured in the as-deformed sample.

A dramatic change in the redistribution of carbon occurs after annealing at 673 K for 30 min. As shown in Fig. 6 (red curve), the high volume fraction of the ferrite/cementite interface produced during extreme deformation decreases greatly after annealing. The bulk carbon concentration in ferrite is reduced to 0.37 ± 0.003 at.% and the carbon concentration in the cementite of 16.6 ± 0.013 at.% approaches the stoichiometric value. We observe that the volume fraction of ferrite after annealing at 673 K even exceeds the value of 85% (for C wt.% = 0.98), as expected from the lever rule. This is due to the fact that a limited size

of the probed volume confines the statistics in determining the phase volume fractions. However, this limit has little influence on the accuracy of the concentration measurement in each individual phase region.

Note that 16.6 at.% is not the carbon concentration in the center of the cementite particles, but the average one in the defined region (see caption of Fig. 6). As will be shown in Section 3.4, the carbon concentration inside these particles reaches 25 at.% after annealing at 673 K for 30 min. Both the dark-field image and the HRTEM result shown in Fig. 7 demonstrate the crystallinity of the cementite particle that may form during annealing at $T \geqslant 673$ K. However, its transformation mechanism upon high-temperature annealing is complicated in the present case due to the uncertainty of the existence of lamellar cementite before annealing. If the cementite undergoes only a partial chemical (not structural) decomposition before annealing, then the formation of cementite particles upon annealing proceeds without nucleation; instead, it is driven simply by the reduction of the ferrite/cementite phase boundary area.

3.4. Grain boundary excess of carbon after annealing at 673 K

Fig. 4 shows that carbon atoms segregate at the ferrite (sub)grain boundaries at 673 K. By using the sub-cutting method [17], the average carbon concentration inside the ferrite grains was measured to be 0.163 ± 0.057 at.% (see the dotted lines in Fig. 8f and g), while it exceeds 1.5 at.% at the grain boundaries (Fig. 8f and g). Two regions of interest cutting through the spheriodized cementite are selected for the analysis of the carbon concentration. The measured values of about 25 at.% C (Fig. 8h and i) show that the carbon concentration in cementite has reached the stoichiometric value again.

It is known that segregation of solute atoms at grain boundaries decreases the grain boundary energy, as described by the Gibbs adsorption isotherm [39–41],

$$d\gamma = -\Gamma_A d\mu_A \qquad (1)$$

where γ is the specific grain boundary energy, Γ is the excess amount of A atoms at the boundary and μ_A is the chemical potential of the solute atoms of type A. This means that the higher the solute excess at the grain boundary, the lower the grain boundary energy.

$\Gamma^\alpha_{C,gb}$, the grain boundary excess of carbon, can be determined either from 1-D concentration profiles (e.g. Fig. 8f and g) or by direct counting of the number of carbon atoms per grain boundary area. With the former method, the carbon concentration in (sub)grain interiors (as shown by the dotted lines in Fig. 8f and g) is subtracted from the measured concentrations. Using the latter method, the number of carbon atoms within the selected region, e.g. "GI" in Fig. 8a, is subtracted from the number of carbon atoms in region "GB", which has the same size as the domain "GI". By using the two methods, $\Gamma^\alpha_{C,gb}$ is determined to be (5.30 ± 0.73) atoms nm^{-2} $(8.80 \times 10^{-6}$ mol m$^{-2})$ and (5.14 ± 0.72) atoms nm^{-2} $(8.54 \times 10^{-6}$ mol m$^{-2})$, respectively.

According to Eq. (1), a carbon excess of $\approx 9 \times 10^{-6}$ mol m^{-2} reduces the grain boundary energy and thus reduces the driving force for grain coarsening, even when annealing the heavily cold-drawn pearlitic steel sample at 723 K. The stabilization of defects such as grain boundaries and dislocations by solute segregation, known as the defactant concept [39–41], has also been reported in Refs. [42–45].

3.5. Redistribution of Si, Mn and Cr during annealing at 673 K

Fig. 9a–d shows the atom maps of Si, Cr, Mn and C (as a reference), respectively, in the wire annealed at 673 K for 30 min. To quantify the distribution of the solute atoms, concentration profiles along a domain $10 \times 2 \times 83$ nm^3 in size, as shown in Fig. 9d, were plotted in Fig. 9f. Corresponding atom maps within the inspected region are shown in Fig. 9e. In accordance with the carbon distribution shown in Fig. 9e, the carbon concentration reaches a maximum in the center of a cementite particle and at the grain boundaries in ferrite, respectively, and has a minimum in the grain

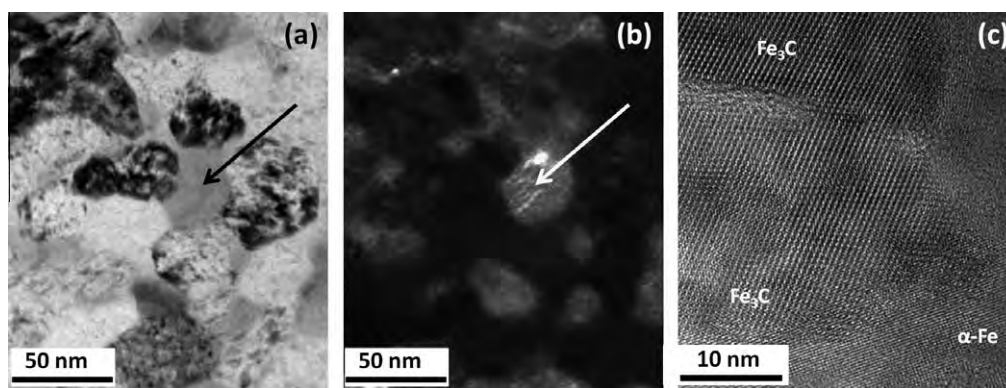Fig. 7. (a) TEM bright-field and (b) dark-field images in the transverse cross-section of a hypereutectoid pearlitic wire after annealing at 673 K for 30 min. A distinct contrast line in the form of bright lines in one cementite particle marked with an arrow indicates a crystalline particle. (c) HRTEM image of a wire after annealing at 723 K for 30 min, showing a crystalline cementite particle in the ferrite matrix.
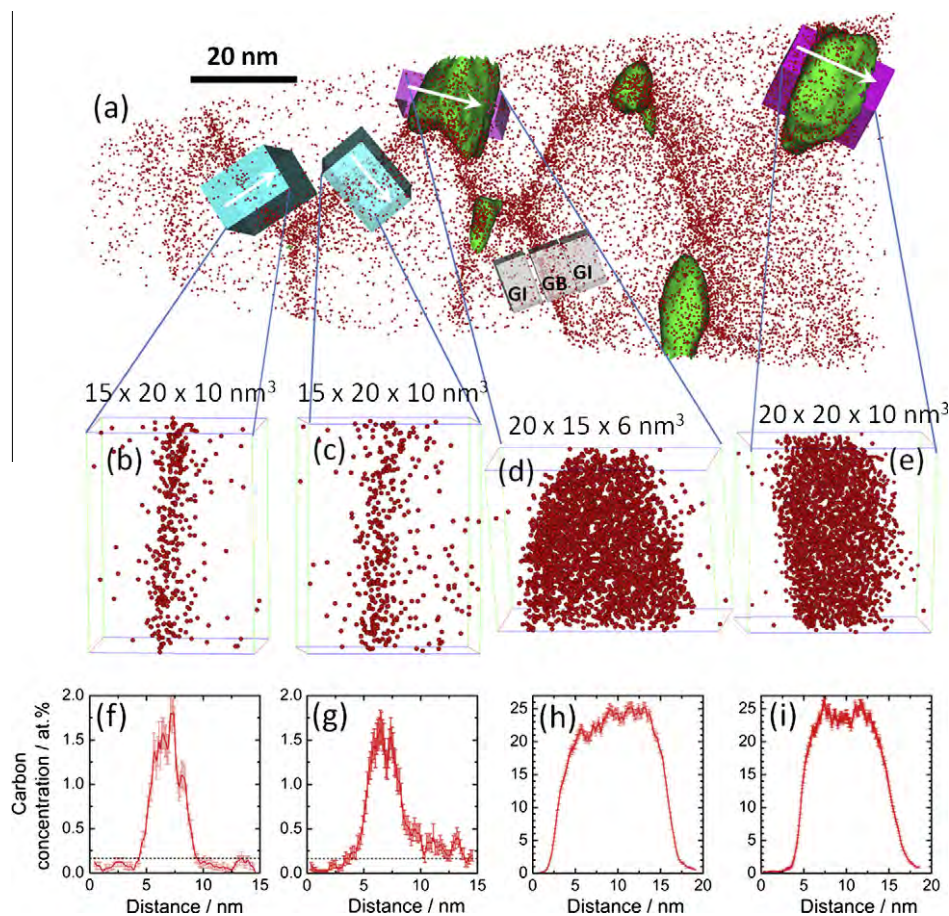
Fig. 8. (a) Carbon atom map of the annealed (673 K for 30 min) hypereutectoid pearlitic steel wire with selected regions of interest (ROIs). The white arrows mark the directions along which the concentration profiles are drawn. The gray-colored ROIs containing grain boundary (GB) and grain interior (GI) are shown as an example for determining the grain boundary excess of carbon (see text). (b–e) Carbon atom maps for the ROIs. The corresponding 1-D carbon concentration profiles are displayed below each atom map (f–i).The average carbon concentration inside the ferrite grains is displayed as short-dashed lines in (f) and (g).

interior (see Fig. 9e). Si is also segregated at the subgrain boundaries (see Fig. 9a and f), where the maxima and minima of the Si concentration correspond well to the locations of subgrain boundaries and subgrain interiors, respectively. The absolute minimum of Si at the center of the cementite particle is consistent to the diminishing equilibrium solubility of Si in cementite as calculated by Thermo-Calc (see Table 1). Cr and Mn atoms are strongly segregated in cementite (see Fig. 9b, c and e). In the grain interior we also observed a depletion of Cr and Mn atoms next to some subgrain boundaries (see the arrows in Fig. 9c). This suggests twofold kinetics in the redistribution of the alloy elements during annealing. One process is the diffusion of Cr and Mn atoms from the subgrain interior to the subgrain boundary inside the ferrite, which leads to Cr- and Mn-depleted areas next to the subgrain boundaries. In the second process, the subgrain boundaries supply a fast diffusion path along which Cr and Mn atoms can quickly diffuse to triple-junction lines, where the spheroidized cementite particles are located owing to the higher vacancy flux along subgrain boundaries. In addition, the distribution of Cr and Mn atoms in cementite is also inhomogeneous (see Fig. 9b, c and e top). The concentration profiles of Cr and

Mn in Fig. 9f show a double plateau (see arrows), located at the ferrite/cementite phase boundaries.

4. Discussion

4.1. Thermal stability of microstructure and strength upon annealing below 473 K

The ultrahigh strength remained stable after the material was annealed at temperatures below 473 K for 30 min (see Fig. 2). This observation is consistent with the analyses of the as-deformed and annealed wires by APT (see Fig. 4a and b). The TEM image in Fig. 5c shows that the lamellar structure still remains even after annealing at 523 K. We conclude that no substantial microstructural change has taken place during annealing at temperatures below 473 K.

One can argue that some softening might already occur due to a slight recovery at the relatively low annealing temperatures. However, this could be compensated by static strain aging during low-temperature annealing or even during the storage of the cold-deformed material at room temperature. The net effect from these two phenomena is that the strength remains unchanged. This argument can
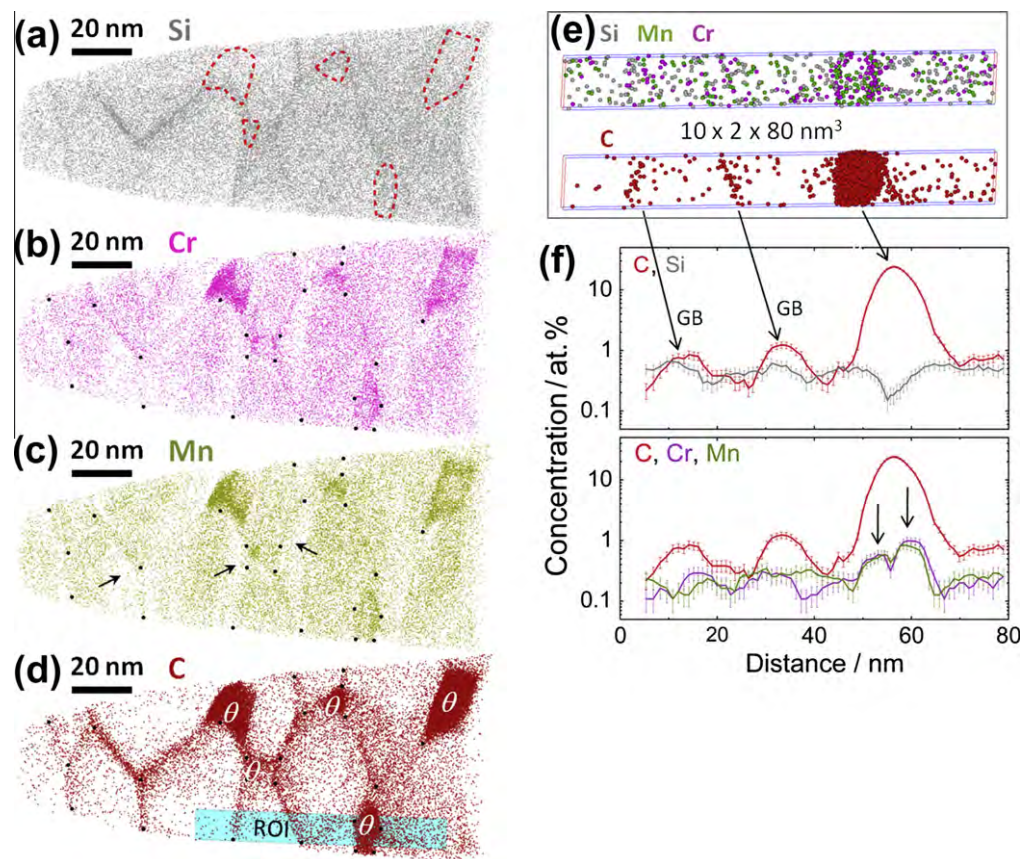
Fig. 9. 3-D atom maps of Si, Cr, Mn and C of a sample annealed at 673 K. 100% of Si, Cr and Mn and 30% of the carbon atoms are displayed. Cementite is labeled with "θ". The red dashed borders in (a) and the black dots in (b) and (c) mark cementite particles and grain boundaries shown in (d), respectively. The 1-D concentration profiles along the ROI chosen in (d) are shown in (f).

Table 1
Solubilities of Si, Mn and Cr in ferrite and cementite under equilibrium conditions calculated by Thermo-Calc using the nominal composition of the wire given in Section 2 (unit: at.%).

Temperature (K)	Si		Mn		Cr	
	Ferrite	Cementite	Ferrite	Cementite	Ferrite	Cementite
473	0.46	0	1.39×10^{-3}	1.81	1.37×10^{-4}	1.24
673	0.46	0	1.86×10^{-2}	1.73	3.27×10^{-3}	1.225

be further discussed as follows: before measuring the tensile strength (both at room temperature and after the various heat treatments), the as-cold-drawn wires were kept at room temperature for about 6 months. The carbon diffusion distance can be estimated as $x = \sqrt{6Dt}$ by taking the bulk diffusivity $D_\alpha^C = D_{0,\alpha}^C \cdot \exp\left(\frac{-Q}{RT}\right)$ ($D_{0,\alpha}^C = 2 \times 10^{-6}$ m² s⁻¹ and $Q = 84.1$ kJ mol⁻¹ [46], R is the gas constant) of carbon in ferrite. This rough estimate yields a carbon diffusion distance of 650 nm in ferrite at room temperature for $t = 0.5$ year and an additional 300 nm at 423 K for 30 min. This estimate shows that carbon can diffuse to dislocations within the fine ferrite lamellae. However, our recent results show that strain aging becomes less significant with increasing wire strain. For a true strain of 6.02 the strain aging effect is barely noticeable. This means that for

weakly drawn wires some carbon atoms have not diffused sufficiently to decorate dislocations even after a storage period of 6 months at room temperature. However, they can diffuse to dislocations upon annealing for only 30 min. This implies an overestimation of the carbon diffusion length at room temperature, possibly due to the supersaturation of the ferrite with carbon upon cold drawing. We attribute the absence of strain aging upon high-temperature annealing for highly strained pearlitic wires ($\epsilon > 5$) to the slightly higher temperature that occurs during drawing as compared to weakly strained wires. This effect facilitates the strong segregation of carbon to single dislocations in the case of highly strained ferrite during the drawing process [17,18]. The effect limits the free sites at dislocations that remain for carbon decoration during static storage at room temperature or annealing at elevated temperatures. Moreover, the

density of single dislocations decreases with further drawing due to the formation of ferrite dislocation cell/substructures which are also decorated with carbon [17,18].

4.2. Recovery and recrystallization during annealing above 473 K

Both the APT (Fig. 4c) and TEM (Fig. 5d) observations show that the elongated ferrite grains inherited from cold drawing still exist after annealing at 673 and 723 K for 30 min. These results suggest that no recrystallization occurs, since recrystallization typically yields equiaxed grains. Furthermore, after annealing at 673 K for 30 min, the carbon content in the ferrite amounts to 40 times the equilibrium value of 0.001 wt.% C at room temperature. This indicates an existence of lattice defects such as vacancies, dislocations and (sub)grain boundaries in the ferrite because these types of defects are able to supply additional sites to trap a large amount of carbon atoms [14,17,18,21]. This means that a typical entirely defect-free recrystallized structure has not yet been formed after annealing at 673 K for 30 min. In addition, the slight (sub)grain structure coarsening in ferrite indicates that recovery rather than recrystallization takes place during annealing because the observed grain size remains far below the typical recrystallized grain size, which is in the micrometer range.

The inhibition of recrystallization in the most heavily cold-deformed ($\epsilon = 6.02$) pearlitic wire can be attributed to the strong fiber texture [3,35], which reduces the driving force for recrystallization and decreases the mobility of grain boundaries by forming low-angle grain boundaries (one dominant grain orientation). Embury and Fisher [2] reported that the misorientation between the ferrite cells is of the order of 1° at a true drawing strain of 3.1. Tarui et al. [47] also confirmed the formation of a cell structure in the ferrite of pearlite at $\epsilon = 4.2$ by selected-area electron diffraction. In addition, the segregation of carbon at the cell/subgrain boundaries and the spheroidized cementite may also inhibit the recrystallization by reducing the grain boundary energy and pinning the grain boundaries against migration, respectively. Also, primary recrystallization proceeds through a nucleation and growth sequence, and the confined interlamellar spacing might be too small for a critical nucleus size to be reached. Thus, we suggest that the formation of cell/subgrain structures after annealing at temperatures above 473 K results not from recrystallization, but from strong recovery of the deformed microstructure.

4.3. Softening during annealing above 473 K

Based on the discussion above, the dramatic drop in tensile strength upon annealing at temperatures above 473 K seems to be mainly due to static recovery of the deformed microstructure through annihilation, rearrangement or polygonization of ferrite dislocations. Readers are referred to Ref. [18] for the mechanism of formation of (sub)grain structure inside the ferrite channel. In addition, the other microstructural changes upon annealing, such as cementite spherodization, redistributions of alloy elements, recovery of point defects (vacancies and interstitials) and relatively slight coarsening of cell/subgrain structures, may also cause the drop in tensile strength, as discussed below in more detail.

4.3.1. Recovery of dislocations at cell/subgrain boundaries

Severe plastic deformation such as cold drawing introduces a high dislocation density into the material. Recently, Zhang et al. [48] reported that the dislocation density ρ in the ferrite lamellae increases from 7.5×10^{13} m^{-2} in the as-patented state to 2×10^{16} m^{-2} after a cold-drawing strain of 3.68. Chen and Kirchheim [49] measured the dislocation density in an annealed pearlitic (0.8 wt.% C) steel wire produced by cold drawing to $\epsilon = 3$. They found that the dislocation density decreases to 8.53×10^{14} m^{-2} after annealing at 723 K for 30 min. While it is not clear how the recovery process occurs, it is very likely in the current system that dislocation recovery takes place mainly at the ferrite/cementite interfaces. For the materials studied in the present work, the lamellar spacing decreases to about 10 nm, thus the major portion of the dislocations created during cold drawing becomes stored at the interface between ferrite and cementite, where they form cell/grain boundaries superimposing on the phase boundaries [18]. Meanwhile, due to the decomposition of cementite, the dislocations from neighboring ferrite may meet at the sites of the original cementite and form a dipolar configuration. Together with an enhanced diffusion process along the phase interface due to severe plastic deformation, a fast annihilation of the dislocation dipoles during annealing becomes feasible. One may note that the quick drop of the tensile strength in the first few minutes during annealing agrees well with the feature of dipole annihilation, as suggest by Hausselt and Blum [50]. We estimate the reduction of the dislocation density on the basis of the drop of the tensile strength by calculating the change of the athermal stress due to the dislocations after annealing:

$$\Delta\sigma_G = \alpha M G b \left(\sqrt{\rho_0} - \sqrt{\rho(T,t)} \right) \tag{2}$$

where α is the dislocation interaction constant, M is the Taylor factor, G is the shear modulus at ambient temperature, b is the length of the Burgers vector, ρ_0 is the dislocation density for the as-deformed state and $\rho(T, t)$ is the dislocation density for the as-annealed state. As a first estimate, we use $\alpha = 0.35$, $M = 3.06$, $G(300 \text{ K}) = 8.2 \times 10^4$ MPa [51] and $b = 0.25$ nm, and the dislocation densities of the above-mentioned measurements. This yields a reduction of the athermal stress of 2.5 GPa by taking the measured dislocations densities of 2×10^{16} m^{-2} for as-deformed wire [48] and 8.53×10^{14} m^{-2} for the wire annealed at 723 K for 30 min [49]. We ignore the possibility of relaxation of the dislocation stress field due to the segregation of carbon atoms at dislocation cores. While this value explains a major part of the strength reduction of 3.4 GPa at 723 K (Fig. 2), one should also consider possible effects associated with other microstructural changes.

4.3.2. Cell/subgrain coarsening during annealing

In the preceding section we discussed that the reduction of strength during annealing can be explained in terms of recovery of dislocations at cell/grain boundaries. As demonstrated by Blum and Zeng [52], the dislocation density in ultrafine-grained materials is closely related to the grain size since dislocations are mainly stored at grain boundaries. Here, as an alternative approach, we may directly describe the relationship between the strength and the (sub)grain size. From Figs. 4 and 5, the initial (sub)grain size d_0 can be roughly estimated to be 10 nm, and the size values $d(T)$ in the transverse direction of the wires are about 30 and 70 nm after annealing at 673 and 723 K, respectively. The corresponding strengths before (σ_0) and after (σ_T) annealing read 6.35, 3.64 and 2.92 GPa (see Fig. 2), respectively. The annealing apparently leads to coarsening of the grain structure, which consequently degrades the strength of the material. These data can be approximated by a Hall–Petch-type relationship:

$$\sigma_0 - \sigma_T = k_{H-P}\left(d_0^{-0.5} - d(T)^{-0.5}\right) \tag{3}$$

with $k_{H-P} \approx 550$ MPa $\mu m^{0.5}$. It has been frequently reported that the Hall–Petch slope in steels increases with the carbon concentration [53], in particular with the carbon concentration at grain boundaries [54–57]. Although a direct comparison of the carbon concentration-dependent k_{H-P} values between our measurement and the literature data is difficult because of the large scatter of the latter data sets [54–57], our measured value falls reasonably within the commonly observed range of $k_{H-P} = 315 \sim 760$ MPa $\mu m^{0.5}$ for steels with carbon segregation at ferrite grain boundaries [55,58].

4.3.3. Spheroidization of cementite

Steels containing pearlitic microstructures have higher strength and hardness than those with spherical cementite because the latter materials have a smaller area fraction of heterointerfaces. In the present case, it is hard to quantify the reduction of tensile strength resulting from the loss of phase boundary density due to cementite spheroidization. During annealing at temperatures above 473 K, the reduced phase boundaries are replenished by cell/subgrain boundaries. The question arises how effective the cell/subgrain boundaries are as barriers to dislocation motion. Together with the spheroidization of cementite, the ferrite cell/subgrain structure continuously coarsens during annealing. Hence, it is difficult to distinguish the softening effects resulting from the loss of phase boundaries from that associated with coarsening of the cell/subgrain structure. The estimate shown in Section 4.3.2 indicates the importance of the cell/subgrain size in the ferrite for the strength of pearlite.

4.3.4. Reduction of solid solution hardening

The loss of solid solution hardening due to the transport of solute atoms from the ferrite to the (sub)grain boundary as well as to cementite during annealing also leads to softening. A loss of carbon solid solution hardening between 300 and 673 K can be estimated by

$$\Delta\sigma_{sol} = k\left(\sqrt{C_{300}} - \sqrt{C_{673}}\right) \tag{4}$$

where k is a prefactor ($\approx 1.12 \times 10^4$ MPa for carbon in Fe [59]) and C_{300} and C_{673} are the carbon concentrations in weight percent in the ferrite after annealing at 300 and 673 K, respectively, for 30 min. Based on the values of 0.75 at.% (0.167 wt.%) for C_{300} and 0.16 at.% (0.036 wt.%) for C_{673} measured by APT, $\Delta\sigma_{sol}$ amounts to only 240 MPa. This means that the loss of solid solution hardening due to the redistribution of carbon atoms upon annealing does not play a major role in the reduction of the tensile strength.

The strengthening effect of other alloying elements, like Mn and Cr, is even lower than that of carbon in the ferrite. Therefore, significant softening resulting from the loss of solid solution hardening by Mn and Cr is not expected. On the contrary, these two elements may have a strengthening effect during annealing, as they are found to segregate at the interfaces between ferrite and cementite, and thus suppress the further growth of cementite particles during annealing. Regarding the solid solution effect, Si is known to be even less effective than Mn. Except for its segregation at ferrite gain boundaries, the distribution of Si in the ferrite and cementite upon annealing does not show a significant difference from that in the as-deformed wire (Fig. 10b).

4.4. Redistribution of alloy elements upon annealing

To better understand the elemental redistribution processes during annealing, proximity histograms [32,60] across ferrite/cementite interfaces were analyzed. Fig. 10 shows the proximity histograms of C, Si, Cr and Mn averaged over multiple interfaces in the as-deformed and annealed wires.

As the concentration profiles show little difference before (i.e. the as-deformed state) and after annealing at 473 K, we only compare in more detail the results between the as-deformed state and the state after annealing at 673 K. In the as-deformed state, two effects of the severe deformation on the microstructure can be observed. One is the partial redistribution of carbon from cementite into ferrite; the other is the approximately homogeneous distribution of Cr and Mn among ferrite and cementite compared to the equilibrium values (Table 1), which we attribute to mechanical mixing (see the green curves in Fig. 10(c) for Cr and (d) for Mn). The main reason why Si does not undergo mechanical mixing upon deformation is the insolubility of Si in cementite (see Table 1). In addition, Si is preferentially located at the ferrite grain boundaries, as seen in Fig. 9aa. This might render mechanical mixing phenomena more sluggish.
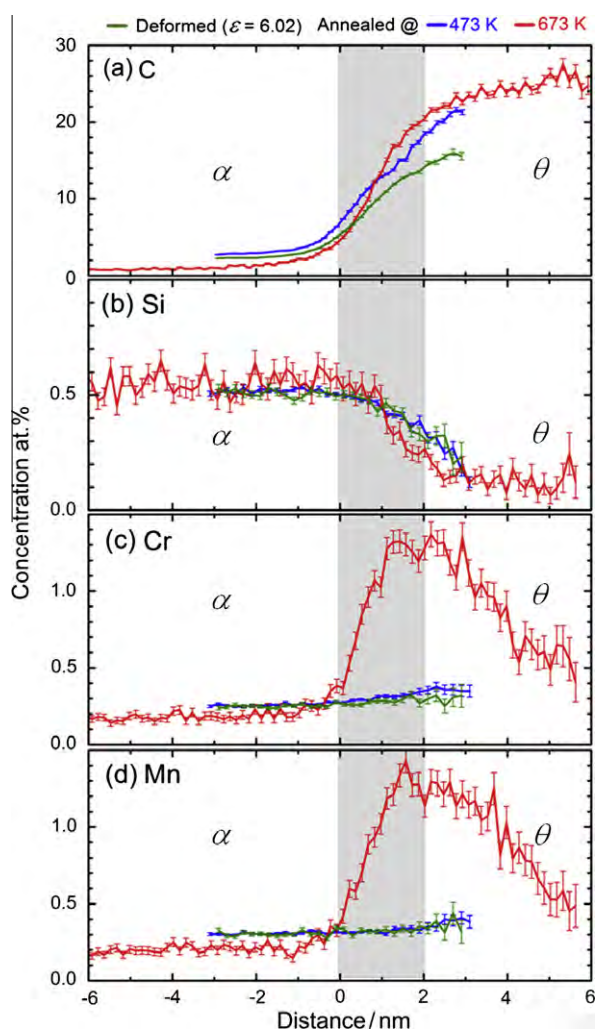
Fig. 10. The proximity histograms [32,60] of (a) C, (b) Si, (c) Cr and (d) Mn obtained from multiple interfaces shown in Fig. 4 for as-deformed (green) and as-annealed states at 473 K (blue) and 673 K (red). Ferrite and cementite separated by the interface (gray zone) are marked with α and θ, respectively.

low initial Si content in cementite (in the as-deformed state) and the fast diffusivity of Si at ferrite grain boundaries, along which the Si can leave the cementite.

Third, a significant number of Cr and Mn atoms diffuse from ferrite to the interfaces between ferrite and cementite. It is known that Cr and Mn are carbide-forming elements and that their solubilities in cementite are much higher than in ferrite (Table 1), as they can substitute Fe in the carbides and form $(Fe,Cr)_3 C$ and $(Fe,Mn)_3C$ [62,63], respectively. As a result, there is a driving force for Cr and Mn to diffuse from ferrite to cementite during annealing. However, the limited diffusivity of these atoms in cementite is likely to act as a kinetic barrier for the fast accommodation of the incoming atom flux from ferrite. According to Ref. [64], the diffusion coefficient of Mn in ferrite D_α^{Mn} (2.4×10^{-23} m^2 s^{-1}) is about three orders of magnitude higher than that in cementite D_θ^{Mn} (8.8×10^{-27} m^2 s^{-1}). According to Ref. [65], Cr behaves similarly to Mn. In particular, at ferrite grain boundaries the diffusivity of Cr and Mn can be even higher, so that the incoming atoms segregate at the ferrite/cementite interface and result in the concentration peaks we observe here (Fig. 10c and d). A similar scenario was recently reported for a maraging-TRIP steel, where the Mn partitioning at martensite/austenite interfaces is due to the low diffusivity of Mn in the austenite, which does not allow the incoming Mn flux from the adjacent martensite to be accommodated within the austenite [66,67].

5. Conclusions

The micro- and nanostructures of a heavily cold-drawn hypereutectoid pearlitic steel wire were studied by APT and TEM in both the as-deformed and annealed states. The lamellar structure consisting of ferrite and cementite is preserved up to annealing at 473 K, with only small changes in the distribution of the solute atoms. Upon annealing at 673 K, the lamellar structure transforms to a subgrain structure in ferrite, with carbon atoms segregated at the grain boundaries and spheroidized cementite located at the triple junctions inside the ferrite. No evidence of recrystallization was found after annealing up to 723 K. The atom maps and concentration profiles of the solutes suggest that (sub)grain boundaries provide a fast diffusion path, along which Si atoms can diffuse from cementite to ferrite and segregate at ferrite grain boundaries. Cr and Mn diffuse from ferrite to cementite, where a kinetic freezing effect (smaller diffusion coefficient in cementite) for the further diffusion of Cr and Mn deeper into the cementite leads to segregation of Cr and Mn at the phase boundaries between ferrite and cementite. The considerable drop in tensile strength after annealing can be mainly attributed to the recovery of dislocations and coarsening of dislocation substructures. The loss of solid solution hardening due to the redistribution of carbon atoms upon annealing gives only a small contribution.

After annealing at 673 K for 30 min, the alloy elements undergo strong redistribution. First, as shown in Fig. 10a, the reduced carbon content in cementite after deformation returns to the stoichiometric value. It should be mentioned that the carbon concentrations we found in cementite in the as-deformed state are inversely dependent on the thickness of the cementite lamellae [17]. The green curve shown in Fig. 10a is obtained from the analysis of relatively thick cementite lamellae. In addition, the concentration gradient at the interfaces between ferrite and cementite becomes sharper after annealing as compared to the blurred interface in the as-deformed state.

Second, a similar increase in the concentration gradient of Si at the ferrite/cementite interfaces indicates an enhanced redistribution of Si atoms from cementite to ferrite due to annealing (see Fig. 10b). It is noted that the concentration of Si increases monotonically from cementite to ferrite without any sign of enrichment of Si at the ferrite/cementite interface [9,61]. This may be attributed to a

Acknowledgements

References

[1] Takahashi T, Ochiai I, Tashiro H, Ohashi S, Nishida S, Tarui T. Nippon Steel Tech Rep 1995;64:45.
[2] Embury JD, Fisher RM. Acta Metall 1966;14:147.
[3] Langford G. Metall Trans A 1977;8:861.
[4] Embury JD, Hirth JP. Acta Metall Mater 1994;42:2051.
[5] Raabe D, Choi P, Li YJ, Kostka A, Sauvage X, Lecouturier F, et al. MRS Bull 2010;35:982.
[6] Belous MV, Cherepin VT. Fiz. Met Metalloved 1961;12:685.
[7] Gridnev VN, Gavrilyuk VG, Dekhtyar IY, Meshkov YY, Nizin PS, Prokopenko VG. Phys Status Solidi A 1972;14:689.
[8] Danoix F, Julien D, Sauvage X, Copreaux J. Mater Sci Eng A 1998;250:8.
[9] Hong MH, Reynolds Jr WT, Tarui T, Hono K. Metall Mater Trans A 1999;30:717.
[10] Sauvage X, Copreaux J, Danoix F, Blavette D. Philos Mag A 2000;80:781.
[11] Hono K, Ohnuma M, Murayama M, Nishida S, Yoshie A. Scripta Mater 2001;44:977.
[12] Wetscher F, Pippan R, Sturm S, Kauffmann F, Scheu C, Dehm G. Metall Mater Trans A 2006;37:1963.
[13] Goto S, Kirchheim R, Al-Kassab T, Borchers C. Trans. Nonferrous Met Soc China 2007;17:1129.
[14] Borchers C, Al-Kassab T, Goto S, Kirchheim R. Mater Sci Eng A 2009;502:131.
[15] Takahashi J, Tarui T, Kawakami K. Ultramicroscopy 2009;109:193.
[16] Sauvage X, Lefebvre W, Genevois C, Ohsaki S, Hono K. Scripta Mater 2009;60:1056.
[17] Li YJ, Choi P, Borchers C, Chen YZ, Goto S, Raabe D, et al. Ultramicroscopy 2011;111:628.
[18] Li YJ, Choi P, Borchers C, Westerkamp S, Goto S, Raabe D, et al. Acta Mater 2011;59:3965.
[19] Languillaume J, Kapelski G, Baudelet B. Acta Mater 1997;45:1201.
[20] Borchers C, Chen Y, Deutges M, Goto S, Kirchheim R. Philos Mag Lett 2010;90:581.
[21] Takahashi J, Kosaka M, Kawakami K, Tarui T. Acta Mater 2012;60:387.
[22] Cerezo A, Godfrey TJ, Smith GDW. Rev Sci Instrum 1988;59:862.
[23] Blavette D, Deconihout B, Bostel A, Sarrau JM, Bouet M, Menand A. Rev Sci Instrum 1993;64:2911.
[24] Miller MK, Cerezo A, Hetherington MG, Smith GDW. Atom probe field ion microscopy. Oxford: Oxford University Press; 1996.
[25] Kelly TF, Miller MK. Rev Sci Instrum 2007;78:031101.
[26] Seidman D. Annu Rev Mater Sci 2007;37:127.
[27] Marquis EA, Miller MK, Blavette D, Ringer SP, Sudbrack CK, Smith GDW. MRS Bull 2009;34:725.
[28] Pereloma EV, Stohr RA, Miller MK, Ringer SP. Metall Mater Trans 2009;40A:3069.
[29] Miller MK. Rev Sci Instrum 2007;78:031101.
[30] Miller MK, Russell KF. Surf Interface Anal 2007;39:262.
[31] Kelly TF, Miller MK. Microsc Res Tech 2006;69:359.
[32] Miller MK, Forbes RG. Mater Charact 2009;60:461.
[33] Takahashi J, Kawakami K, Kobayashi Y. Ultramicroscopy 2011;111:1233.
[34] Langford G. Metall Trans 1970;1:465.
[35] Zelin M. Acta Mater 2002;50:4431.
[36] Hosford Jr WF. Trans AIME 1964;230:12.
[37] Raabe D, Heringhaus F, Hangen U, Gottstein G. Z Metallkd 1995;86:405.
[38] Heringhaus F, Raabe D, Gottstein G. Acta Mater 1995;43:1467.
[39] Kirchheim R. Acta Mater 2002;50:413.
[40] Kirchheim R. Acta Mater 2007;55:5129.
[41] Kirchheim R. Acta Mater 2007;55:5139.
[42] Boylan K, Ostrander D, Erb U, Palumbo G, Aust KT. Scripta Metall Mater 1991;25:2711.
[43] Mehta SC, Smith DA, Erb U. Mater Sci Eng A 1995;204:227.
[44] Farber B, Cadel B, Menand A, Schmitz G, Kirchheim R. Acta Mater 2000;48:789.
[45] Choi P, da Silva M, Klement U, Al-kassab T, Kirchheim R. Acta Mater 2005;53:4473.
[46] Wert CA. Phys Rev 1950;79:601.
[47] Tarui T, Maruyama N, Takahashi J, Nishida S, Tashiro H. Nippon steel technical report no. 91; January 2005.
[48] Zhang X, Godfrey A, Huang X, Hansen N, Liu Q. Acta Mater 2011;59:3422.
[49] Chen YZ, Kirchheim R. Personal communication.
[50] Hausselt J, Blum W. Acta Metall 1976;24:1027.
[51] Frost HJ, Ashby MF. Deformation-mechanism maps. Oxford: Pergamon Press; 1982.
[52] Blum W, Zeng XH. Acta Mater 2009;57:1966.
[53] Nam WJ, Bae CM, Lee CS. J Mater Sci 2002;37:2243.
[54] Wilson DV. Met Sci J 1967;1:40.
[55] Mintz B, He H, Smith GDW. Mater Sci Technol 1992;8:537.
[56] Takeda K, Nakada N, Tsuchiyama T, Takaki S. ISIJ Int 2008;48:1122.
[57] Takahashi J, Kawakami K, Ushioda K, Takaki S, Nakata N, Tsuchiyama T. Scripta Mater 2012;66:207.
[58] Mintz B. Met Technol 1984;11:265.
[59] Gottstein G. Physikalische grundlagen der materialkunde. Heidelberg: Springer-Verlag; 1998.
[60] Hellman OC, Vandenbroucke JA, Rüsing J, Isheim D, Seidman DN. Microsc Microanal 2000;65:437.
[61] Balak J, Sauvage X, Lee DL, Lee CY, Pareige P. Adv Mater Res 2007;26–28:45.
[62] Gurry RW, Christakos J, Darken LS. Trans ASM 1961;53:187.
[63] Schaaf P, Wiesen S, Gonser U. Acta Metall Mater 1992;40:373.
[64] Fridberg J, Trndahl LE, Hillert M. Jernk Ann 1969;153:263.
[65] Barnard SJ, Smith GDW, Garratt-Reed AJ, Vander Sande JB. In: Aaronson HI, Laughlin DE, Sekerka RF, Wayman CM, editors. Proceedings of the international conference on "solid–solid phase transformations". Warrendale (PA): AIME; 1982. p. 881.
[66] Raabe D, Ponge D, Dmitrieva O, Sander B. Scripta Mater 2009;60:1141.
[67] Dmitrieva O, Ponge D, Inden G, Millán J, Choi P, Sietsma J, et al. Acta Mater 2011;59:364.

Nanoscale austenite reversion through partitioning, segregation and kinetic freezing: Example of a ductile 2 GPa Fe–Cr–C steel

L. Yuan [a], D. Ponge [a], J. Wittig [a,b], P. Choi [a], J.A. Jiménez [c], D. Raabe [a,*]

[a] *Max-Planck-Institut für Eisenforschung, Max-Planck-Str. 1, 40237 Düsseldorf, Germany*
[b] *Vanderbilt University, Nashville, TN 37235-1683, USA*
[c] *CENIM-CSIC, Avda. Gregorio del Amo 8, 28040 Madrid, Spain*

Abstract

Austenite reversion during tempering of a Fe–13.6 Cr–0.44 C (wt.%) martensite results in an ultra-high-strength ferritic stainless steel with excellent ductility. The austenite reversion mechanism is coupled to the kinetic freezing of carbon during low-temperature partitioning at the interfaces between martensite and retained austenite and to carbon segregation at martensite–martensite grain boundaries. An advantage of austenite reversion is its scalability, i.e. changing tempering time and temperature tailors the desired strength–ductility profiles (e.g. tempering at 400 °C for 1 min produces a 2 GPa ultimate tensile strength (UTS) and 14% elongation while 30 min at 400 °C results in a UTS of ∼1.75 GPa with an elongation of 23%). The austenite reversion process, carbide precipitation and carbon segregation have been characterized by X-ray diffraction, electron back-scatter diffraction, transmission electron microscopy and atom probe tomography in order to develop the structure–property relationships that control the material's strength and ductility.
© 2012 Acta Materialia Inc. Published by Elsevier Ltd. All rights reserved.

Keywords: Austenite reversion; Partitioning; Diffusion; Strength; Ductility

1. Introduction

A high demand exists for lean, ductile and high-strength Fe–Cr stainless steels in the fields of energy conversion, mobility and industrial infrastructure. As conventional martensitic stainless steels (MSSs) typically exhibit brittle behavior, supermartensitic Fe–Cr stainless steels (SMSSs) with enhanced ductility have been designed in the past years by reducing carbon (<0.03 wt.%) and adding nickel (4–6.5 wt.%) and molybdenum (2.5 wt.%) [1–4]. The heat-treated microstructures of these materials are characterized by tempered martensite and retained austenite [1–4].

In this work we present an alternative approach of designing MSSs with both high strength and high ductility. Our method is based on nanoscale austenite reversion and martensite relaxation via a modest heat treatment at 300–500 °C for several minutes. We make the surprising observation that this method leads to very high strength (up to 2 GPa) of a Fe–13.6Cr–0.44C (wt.%) steel without loss in ductility (X44Cr13, 1.4034, AISI 420).

Quenching followed by tempering is known to improve the strength and toughness of martensitic steels [5–7]. Specifically, quench and partitioning (Q&P) treatments are efficient for producing steels with retained austenite and improved ductility [8]. The heat treatment sequence for Q&P steel involves quenching to a temperature between the martensite-start (M_s) and martensite-finish (M_f) temperatures, followed by a partitioning treatment either at, or above, the initial quench temperature. Partitioning is typically designed in a way that enriches and stabilizes the retained austenite with carbon from the supersaturated martensite [9]. In conventional Q&P processes, the quench temperature is hence chosen such that some retained austenite prevails and subsequent tempering leads to carbon

* Corresponding author. Tel.: +49 0211 6792 333.
E-mail address: d.raabe@mpie.de (D. Raabe).

partitioning between martensite and austenite. Typically, no new austenite is formed during partitioning.

In our study we modify this approach with the aim to increase the amount of austenite during low-temperature partitioning. We start with austenitization and water quenching to room temperature. This provides a martensitic–austenitic starting microstructure. During a subsequent heat treatment in the range 300–500 °C, austenite reversion [10–15] takes place on the basis of partial partitioning according to local equilibrium, segregation and kinetic freezing of carbon inside the newly formed austenite.

It is important to point out that the phenomena occurring during austenite reversion are in the present case different from conventional Q&P approaches: in Q&P processing, the carbon diffuses from martensite into the already present austenite during tempering where equilibration of the carbon distribution inside the austenite is generally assumed. In the current case of low-temperature partitioning, however, the carbon is enriched in front of the austenite boundary and accumulates there since it has a much higher diffusion rate in body-centered cubic (bcc) than in face-centered cubic (fcc) material. The accumulated carbon at the martensite–austenite interface then provides a high local driving force for austenite reversion. Once captured by the growing austenite, the carbon is kinetically frozen owing to its small mobility in this phase.

The phenomena occurring during austenite reversion in Fe–Cr–C stainless steels are complex due to the high content of carbon and substitutional alloying elements. In contrast to typical Q&P steels where carbide precipitation (M_3C) is suppressed by alloying with Si and/or Al [16], in the present alloy M_3C-type carbide precipitation occurs at 400 °C. This means that a kinetic and thermodynamic competition exists for carbon between austenite reversion, enrichment of retained austenite and carbide formation during tempering.

Therefore, the partitioning temperature must be chosen on a theoretically well founded basis for two reasons: first, low temperature annealing requires more local carbon enrichment to provide a driving force high enough for austenite reversion. We emphasize in this context that the local equilibrium matters for this process, i.e. a high carbon content is required at the martensite–austenite interface (not everywhere within the austenite). Equilibration of the carbon inside the austenite is not necessarily required. Second, high temperature annealing may cause more carbide formation, consuming too much carbon, so that austenite reversion is suppressed due to an insufficient carbon chemical potential to promote it.

In order to elucidate the competing phenomena occurring during such low-temperature partitioning, namely, carbide formation vs. austenite reversion as well as the carbon redistribution inside the retained and reversed austenite fractions, atom probe tomography (APT) was used. This method allows us to measure the carbon content inside the austenite, which determines its stability, as well as inside the martensite and the carbides [17–28]. The APT method allows for three-dimensional (3-D) elemental mapping with nearly atomic resolution and provides information about internal interfaces and local chemical gradients [28–32].

2. Experimental

The material used in this study was a martensitic stainless steel with the chemical composition Fe–13.6Cr–0.44C (wt.%; 1.4034, X44Cr13, AISI 420), which was provided by ThyssenKrupp Nirosta as a cold rolled sheet, Table 1. The Ae_3 temperature, calculated by Thermo-Calc [33] using the TCFE5 database [34], indicates that the incipient holding temperature for full austenitization should be above 800 °C. The calculation further reveals that full dissolution of chromium carbides in austenite is achieved at ~1100 °C. Hence, the annealing conditions were set to 1150 °C for 5 min. Dilatometer tests were performed using a Bähr Dil805 A/D quenching and deformation device to identify the M_s temperature during quenching. After water quenching, tempering at 300, 400 and 500 °C, respectively, with different holding times was performed to study carbon redistribution, austenite reversion and carbide formation (Fig. 1).

Mechanical properties were determined by tensile and Vickers hardness measurements (980N load, HV10). Tensile tests were carried out along the rolling direction of the samples at room temperature. Flat tensile specimens were machined with a cross-section of 2.5 mm × 8 mm and a gauge length of 40 mm. The tests were conducted on a Zwick/Roell Z100 tensile testing machine at a constant cross-head speed of 1 mm min^{-1}, corresponding to an initial strain rate of 4.2×10^{-4} s^{-1}.

The volume fraction of the austenite phase after heat treatments (carbide dissolution annealing and tempering at 400 °C for 1, 2, 10 and 30 min) was measured by X-ray diffraction (XRD), electron back-scatter diffraction (EBSD) and magnetic characterization (Feritscope MP30E-S).

EBSD samples were prepared by standard mechanical grinding and polishing procedures normal to the rolling direction. Subsequently, these samples were electropolished using Struers electrolyte A3 at room temperature using a voltage of 40 V, a flow rate of 20 s^{-1} and a polishing time of 20 s. EBSD was performed on a JEOL-6500F high-resolution field-emission scanning electron microscope operated at 15 kV [35].

XRD measurements were carried out using Co Kα radiation. XRD data were collected over a 2θ range of 30–138°

Table 1
Chemical composition of material used for the investigation (1.4034, X44Cr13, AISI 420).

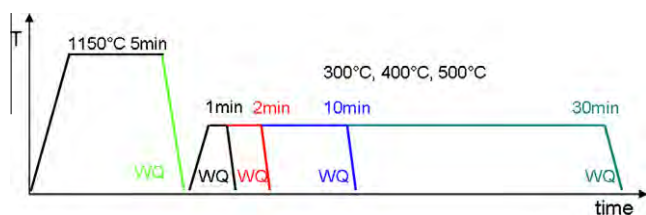|	C	Cr	Mn	Ni	Si	N	Fe
wt.%	0.437	13.6	0.53	0.16	0.284	0.0205	Bal.
at.%	1.97	14.19	0.52	0.15	0.55	0.079	Bal.

Fig. 1. Schematic diagram of the heat treatment route (WQ: water quenching).

with a step width of 0.05° and a counting time of 10 s per step. The Rietveld method was used for the calculation of the structural parameters from the diffraction data of the polycrystalline bulk materials. We used version 4.0 of the Rietveld analysis program TOPAS (Bruker AXS). The analysis protocol included consideration of background, zero displacement, scale factors, peak breath, unit cell parameter and texture parameters. The room temperature structures used in the refinement were martensite/ferrite and austenite.

Thin foils were prepared using standard twin-jet electropolishing from the as-quenched material and the tempered samples before and after deformation [36]. These samples were examined by transmission electron microscopy (TEM) in a Philips CM 20 at an acceleration voltage of 200 kV to characterize the carbide evolution and the formation of reverted austenite. Carbide characterization was also carried out by using a carbon extraction replica technique [37] and investigated by electron diffraction and energy dispersive spectroscopy (EDS) in the transmission electron microscope.

Needle-shaped APT samples were prepared by applying a combination of standard electropolishing and subsequent ion-milling with a focused-ion-beam (FIB) device. APT analyses were performed with a local electrode atom probe (LEAP™ 3000X HR) in voltage mode at a specimen temperature of ~60 K. The pulse-to-base voltage ratio and the pulse rate were 15% and 200 kHz, respectively. Data analysis was performed using the IVAS software (Cameca Instruments).

3. Results

3.1. Mechanical properties

The as-received cold rolled and recrystallized material has an ultimate tensile strength (UTS) of 640 MPa and a uniform elongation of 19%, Fig. 2a. After austenitization at 1150 °C and water quenching, the material is brittle and fails before the yield stress is reached at a stress of 400 MPa (Fig. 2a). Thus, the true UTS for the as-quenched state could be only estimated from the indentation hardness. The relationship between Vickers hardness (HV) and tensile strength was calculated considering a linear relationship of the form $\Delta HV = K \times \Delta UTS$. A constant K of 3.5 was determined by linear regression through data

obtained from the hardness and UTS values obtained from samples after tempering at 400 °C for different times. Fig. 2e suggests that the hardness for the as-quenched state corresponds to a tensile strength of more than 2300 MPa.

Fig. 2a also shows the stress–strain curves obtained from the tensile tests performed on samples tempered at 400 °C for different times. The most remarkable feature of these curves is the transition from a brittle behavior in the as-quenched material to a ductile one after tempering. When the tempering time is increased, we observe an increase in uniform elongation and a decrease in UTS. After 30 min, the uniform elongation of the sample reaches a value of ~22% and a UTS above 1760 MPa. This value for the UTS can be also reached upon tempering at 500 °C, but in this case, a gradual increase in total elongation upon increase in tempering time is not observed, Fig. 2b. It can be observed that in this case the stress does not go through a maximum; that is, σ/e (the partial derivative of the stress with respect to strain) does not go through zero. This would indicate that the sample fractures before the strain reach the necking value. At 300 °C, after 1 min, the ductility improves slightly, i.e. longer tempering is required for obtaining better ductility at this temperature, as shown in Fig. 2c. When comparing the mechanical properties of samples tempered at different temperatures (Fig. 2d), the 400 °C treatment yields the optimum improvement in both UTS and total elongation (TE).

3.2. Phase fractions and kinetics: predictions and experiments

Thermo-Calc was used to calculate the phase equilibrium at the different partitioning temperatures. For evaluating kinetics during heating and cooling, we conducted dilatometer tests (Fig. 3). The heating and cooling rates were set to 10 and -30 K s^{-1}, respectively. Above 876 °C, the microstructure is fully austenitic. The M_s temperatures were derived from the dilatometer tests (118 °C after 1150 °C annealing and 360 °C after 950 °C annealing). The Thermo-Calc calculations were used to predict the equilibrium carbon content of the austenite after annealing at different temperatures (Fig. 3c).

Fig. 4 shows the phase fraction of austenite vs. tempering time for 400 °C measured by feritscope (magnetic signal), EBSD and XRD. For the as-quenched state the EBSD result provides a higher volume fraction (20%) than the magnetic (14.5%) and the XRD data (8%), which is attributed to the limited statistics of the EBSD method. During the first 2 min of tempering the amount of austenite increases rapidly, indicating austenite reversion. After 30 min, nearly 40 vol.% austenite is observed consistently for all three methods.

Fig. 5 shows in situ EBSD observations of the austenite during tempering. Fig. 5a maps the material in the as-quenched state containing only retained austenite. Fig. 5b shows the same area during the in situ experiment containing both retained plus reverted austenite after 5 min
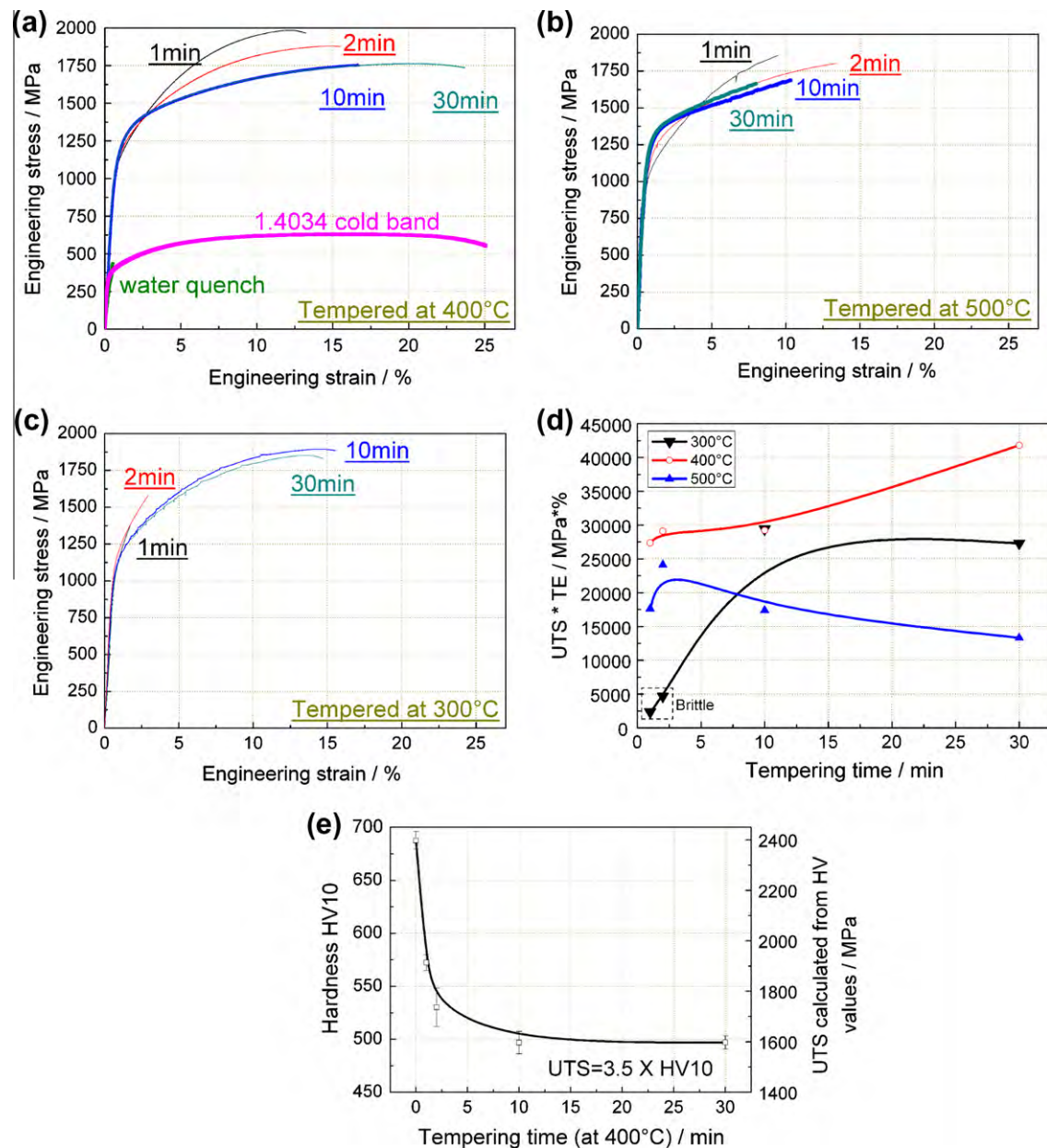
Fig. 2. Mechanical properties of the quenched and partitioned stainless steel Fe–13.6Cr–0.44C (wt.%, 1.4034, AISI 420) after different types of partitioning and austenite reversion treatments. The original state of a commercial alloy (1.4034, cold band) is shown as reference. The term "cold band" refers here to hot rolled, cold rolled and finally recrystallized material. (a–c) Stress–strain curve of samples tempered at 400, 500 and 300 °C, respectively. Note in (a) that the as-quenched sample (green) fails already in the elastic regime. (d) Multiplied quantity UTS × TE as a function of annealing time for the three different temperatures; (e) UTS–HV relationship (UTS: ultimate tensile strength; HV: Vickers hardness; TE: total elongation).

tempering at 400 °C subsequent to the quenching treatment. The EBSD map reveals the fine dispersion of the newly formed reverted austenite after 5 min. We observe two kinds of austenite, namely one with a coarse topology and another one with a fine and dispersed topology.

The microstructures of the samples tempered for 0, 1 and 2 min, respectively, are shown in Fig. 6. The as-quenched material (0 min tempering) is brittle and failed already in the elastic regime during tensile testing. From the microstructure it can be seen (Fig. 6b, left: before tensile test; right: after tensile test, for each state) that only a small amount of austenite was transformed to martensite when the material failed, i.e. austenite bands can still be observed near the fracture interface. For samples after 400 °C tempering, no premature failure takes place and the total elongation (TE) reaches 14% (engineering strain). The microstructure at the fracture zone shows nearly no remaining austenite. This observation indicates that deformation-driven austenite-to-martensite transformation takes place. Secondary cracks along the tensile direction are visible in the EBSD maps. It seems that these cracks follow the band-like former retained austenite regions, which transformed during straining into martensite.
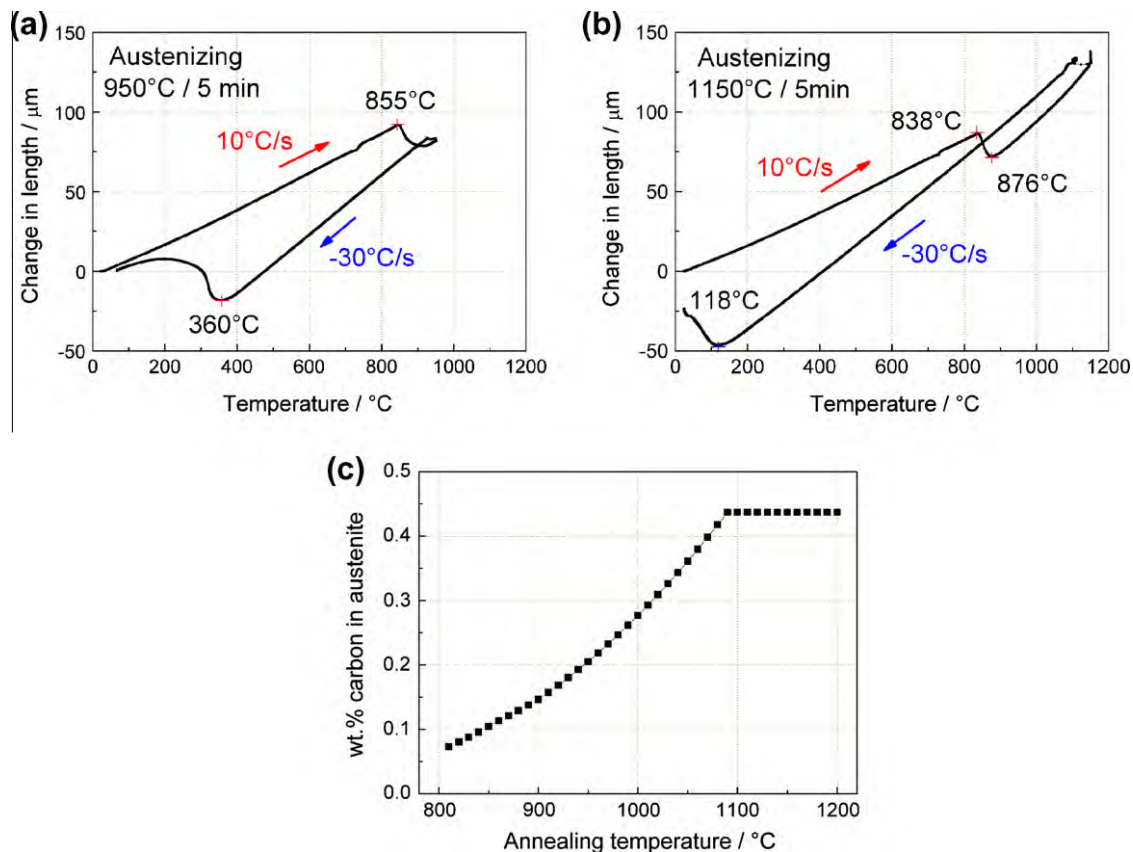
Fig. 3. Results of the dilatometer tests of the stainless steel Fe–13.6Cr–0.44C (wt.%, 1.4034). (a) Austenitization at 950 °C for 5 min. (b) Austenitization at 1150 °C for 5 min. (c) Calculated equilibrium carbon content in austenite at different annealing temperatures (Thermo-Calc TCFE5).
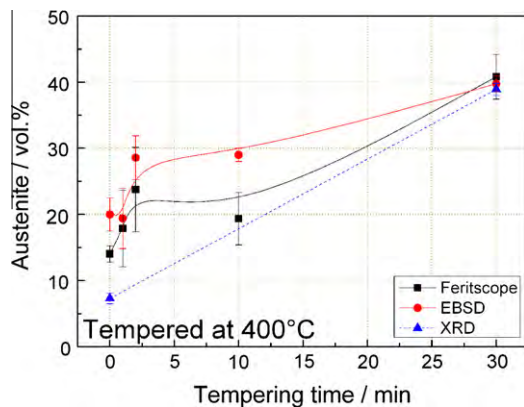

Fig. 4. Austenite volume fraction as a function of tempering time (at 400 °C) measured by feritscope (magnetic signal), EBSD and XRD.

3.3. TEM characterization

After solid solution and subsequent water quenching, we found no retained austenite in the TEM foils (Fig. 7a and b). This is in contrast to the results obtained from the EBSD maps which show retained austenite in the as-quenched state (Figs. 5 and 6). We attribute this discrepancy between TEM and EBSD results to the fact that the as-quenched metastable retained austenite – when thinned

for TEM analysis – is no longer constrained by the surrounding martensite and hence transforms into martensite.

After 1 min tempering at 400 °C we observe a high tensile strength of 2 GPa, Fig. 2a. The corresponding microstructure was monitored by TEM, Fig. 7. Fig. 7c and d gives an overview of the nanoscaled elongated carbides formed during tempering.

The carbides have an average length of 70 nm and an average width of 5 nm. After 30 min tempering the average particle spacing is ∼80 nm and the length 110 nm. The carbides after 1 min tempering at 400 °C were examined via carbon extraction replica. The diffraction patterns reveal that they have M_3C structure. This means that the formation of $M_{23}C_6$ carbides is suppressed at such a low tempering temperature. EDS analyses showed that the metal content in the carbide (M in M_3C) amounts to 74 at.% Fe and 26 at.% Cr, i.e. the Cr/Fe atomic ratio is 0.35. The measured chromium content in the M_3C carbides significantly deviates from the nominal chromium concentration of 14.2 at.% Cr/82.5 at.% Fe = 0.17.

Fig. 7e shows the formation of a thin austenite layer that is located at a former martensite–martensite grain boundary. Fig. 7f is a close-up view of a thin austenite zone that is surrounded by martensite. Electron diffraction analysis reveals that a Kurdjumov–Sachs orientation relationship exists between the martensite matrix and the thin austenite
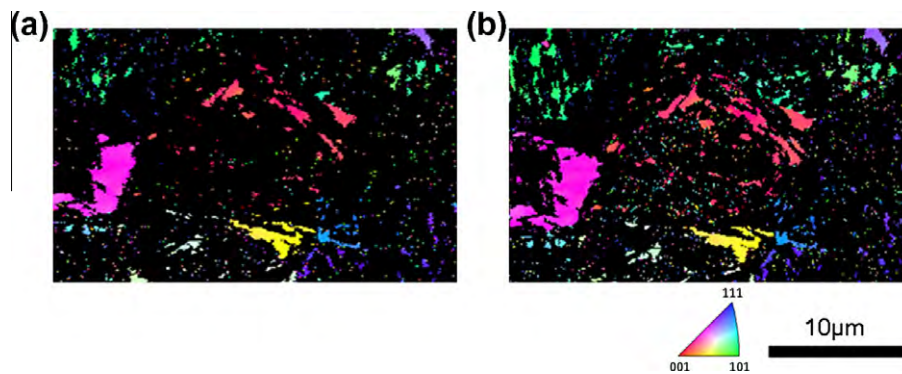
Fig. 5. EBSD inverse pole figure map of the same specimen region showing retained and reverted austenite (IPF∥ND, only austenite shown): (a) shows the material as-quenched containing only retained austenite; (b) shows the material containing both retained plus reverted austenite after quenching and 5 min tempering at 400 °C (EBSD: electron back-scatter diffraction; IPF: inverse pole figure color code; ND: normal direction).
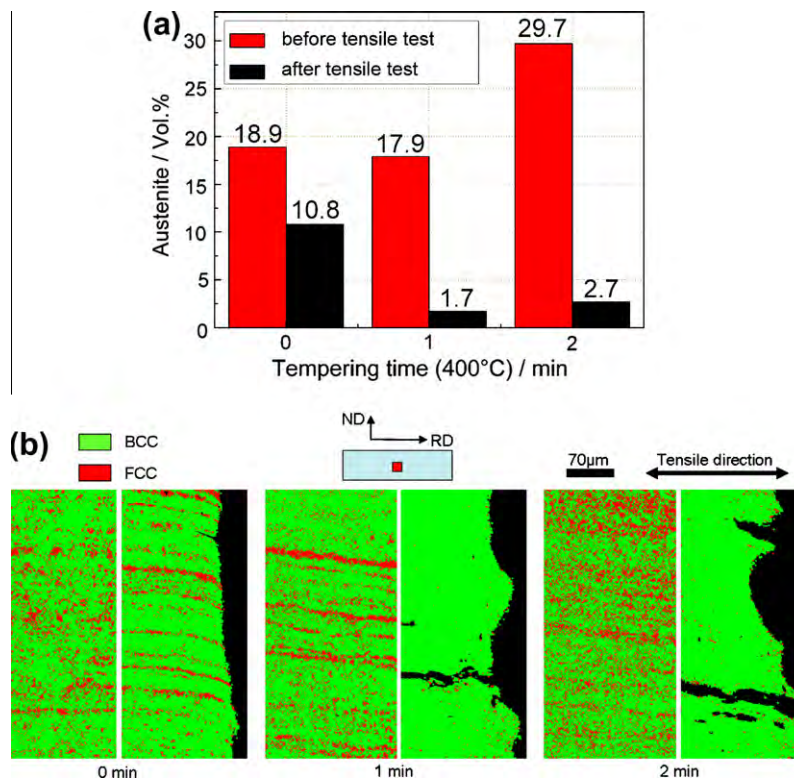

Fig. 6. (a) EBSD phase maps of samples tempered at 400 °C for 0, 1 and 2 min at 400 °C, and of the TRIP effect obtained from EBSD phase analysis. The red columns show the austenite content before and the black ones after the tensile tests. (b) Microstructure of samples before and after tensile testing subjected to different tempering conditions (left: before tensile test; right: after tensile test); bcc: martensite phase; fcc: austenite phase.

layer, Fig. 7g [38]. In line with the in situ EBSD results in Fig. 5, where we observed reverted austenite formed between martensitic grains, the austenite film observed here in TEM might be either retained or reversed austenite. In order to determine more reliably which of the two kinds is observed local atomic scale chemical analysis is conducted by using APT as outlined below. The two types of austenite can then be distinguished in terms of their carbon content: Retained austenite has at first the nominal quenched-in C content ($\sim$2 at.% in the present case) of the alloy while reverted austenite has a higher C content

(up to 9 at.%) owing to local partitioning and kinetic freezing. However, we also have to account for the possibility that the retained austenite can have a higher C content as the lath martensite mechanism is slow enough to allow for some C diffusion out of the martensite into the retained austenite during quenching.

3.4. Atom probe tomography

The local chemical compositions and their changes during 400 °C tempering of the martensite, austenite, carbides
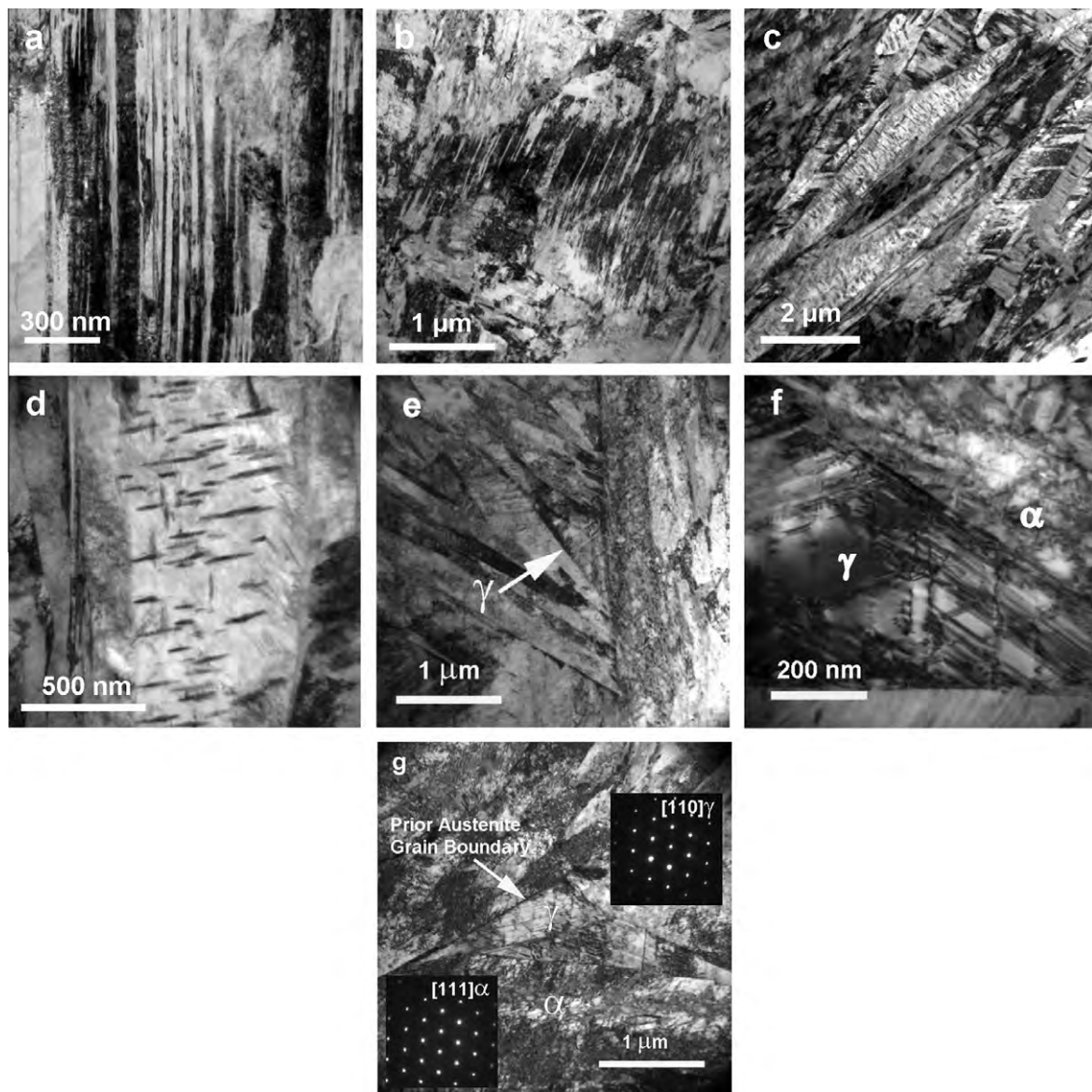
Fig. 7. TEM images of as-quenched sample (only lath martensite was found: (a and b) TEM images of samples tempered at 400 °C for 1 min; (c) overview image of the very dense array of nanoscaled carbides that is formed during tempering; (d) in-grain view of the carbides; (e) overview image of the formation of a reverted austenite grain that is located at a former martensite–martensite grain boundary; (f) close-up view of reverted austenite that is surrounded by martensite; (g) electron diffraction analysis reveals that a Kurdjumov–Sachs growth orientation relationship exists between the martensite matrix and the reverted austenite.

and interface regions were studied by atom probe tomography. Phase identification is in all cases achieved via the characteristic carbon contents of the present phases. Fig. 8 shows the 3-D atom maps after water quenching (Fig. 8a), water quenching plus tempering at 400 °C for 1 min (Fig. 8b) and water quenching plus tempering at 400 °C for 30 min (Fig. 8c). Carbon atoms are visualized as pink dots and carbon iso-concentration surfaces are in green for a value of 2 at.%. This value corresponds to the nominal carbon concentration of the alloy of 0.44 wt.%. The different phases (martensite, austenite, carbide) are marked. They were identified in terms of their characteristic carbon content and the TEM and EBSD data presented above. For more quantitative analyses, one-dimensional

compositional profiles of carbon across the martensite–martensite and martensite–austenite interfaces were plotted (along cylinders marked in yellow in the 3-D atom maps).

3.4.1. As-quenched condition

Fig. 8a reveals that in the probed volume carbon is enriched along the martensite–austenite interface. The interface region, shown as composition profile in Fig. 8a, reveals an average carbon concentration of ~1.90 at.% in the austenite with strong local variations and of ~0.98 at.% in the abutting supersaturated martensite. The carbon concentration in the austenite nearly matches the nominal carbon concentration of the alloy. Some carbon clusters occur in both phases. The carbon concentration
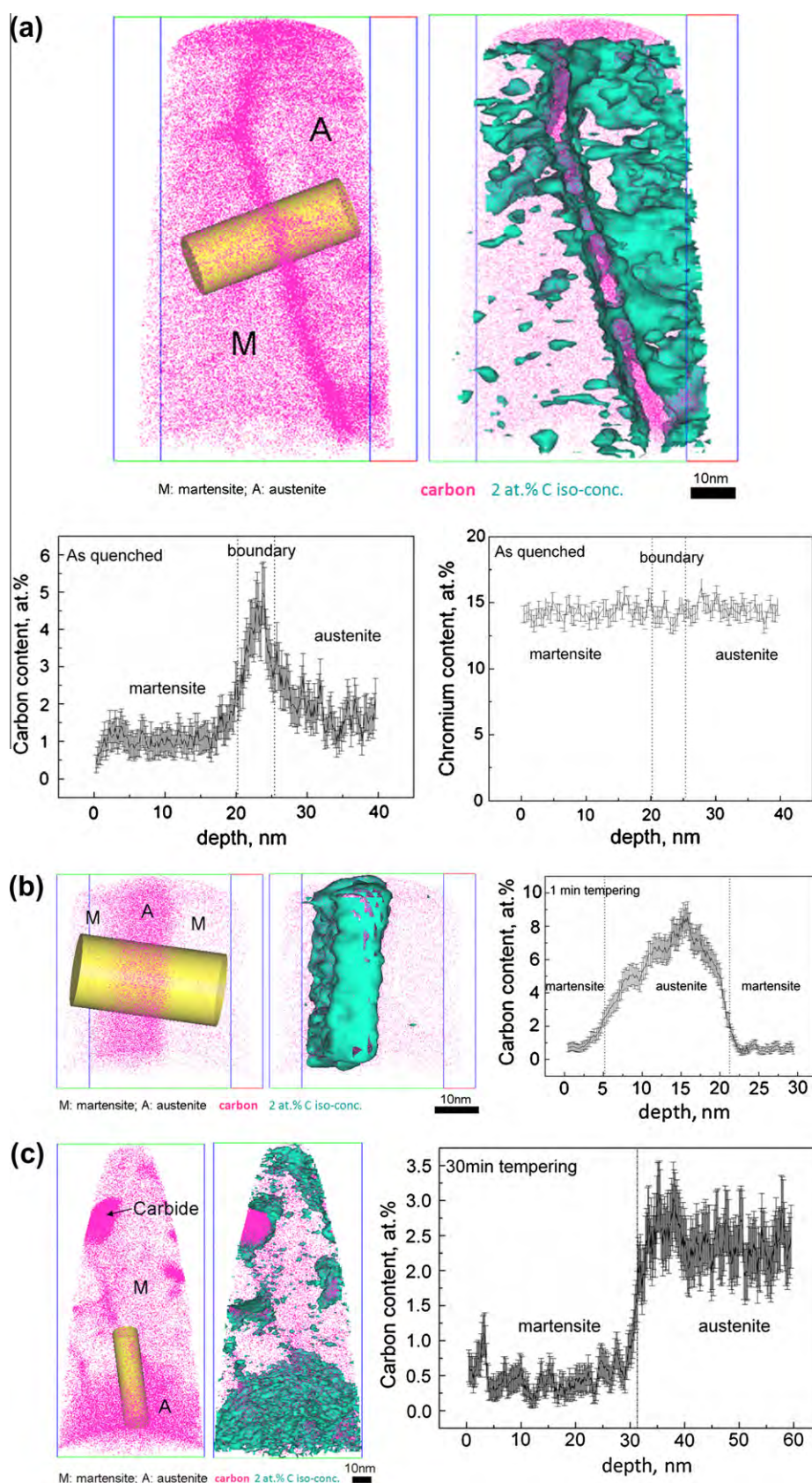
Fig. 8. (a) 3-D reconstructions (frame scale in nm) of sample after water quenching. The data clearly show that carbon redistribution already occurs during quenching. Cr redistribution does not occur. (b) Tempered at 400 °C for 1 min; (c) tempered at 400 °C for 30 min. Carbon atoms are displayed pink. The different phases are marked in the figure. Carbon iso-concentration surface (2 at.%, corresponding to 0.44 wt.%, green) and concentration profiles across the phase boundaries along the yellow cylinder) are also shown.

Table 2
Change of the carbon content observed in each phase via atom probe tomography during annealing, quenching and austenite reversion. The carbon partitioning to the different phases is quantified in terms of the enrichment factor $\varepsilon = $ (at.% C tempered)/(at.% C as-quenched), which allows us to compare the chemical composition in the phases before and after tempering.

State of samples	Retained austenite (at.%)	Martensite (at.%)	Interface (at.%)	Reverted austenite (at.%)
Nominal composition (annealing at 1150 °C)	1.97%	–	–	–
As-quenched	1.90%	0.98%	4.52%	–
Quenched plus tempering (400 °C/1 min)	–	0.82% ($\varepsilon = 0.84$)	–	6.86% ($\varepsilon = 3.61$)
Quenched plus tempering (400 °C/30 min)	2.42% ($\varepsilon = 1.27$)	0.48% ($\varepsilon = 0.49$)	–	–

in these clusters is $\sim$3 at.%, i.e. they are not carbides. In a thin interface layer of only $\sim$5 nm, the carbon content is very high and reaches a level of 4–6 at.%. In contrast to the variation in the carbon distribution, the chromium content is the same in the martensite, the interface and the austenite, Fig. 8a.

3.4.2. 400 °C tempered condition after quenching

After 1 min tempering at 400 °C, a carbon-enriched austenite layer (15–20 nm width) is observed between two abutting martensite regions (Fig. 8b). The thin austenite zone contains on average $\sim$6.86 at.% carbon while the martensite matrix contains only $\sim$0.82 at.% carbon. The identification of the phases in these diagrams follows their characteristic carbon content.

After 30 min tempering (Fig. 8c), different carbon-enriched areas appear. They correspond to individual phases. The analyzed volume can be divided into two zones. The top region with low carbon content corresponds to martensite. The bottom zone with higher carbon content corresponds to austenite. Inside the martensitic region there are areas with very high carbon content (see arrow in Fig. 8c). The carbon content is 25.1 at.% in this particle, indicating M_3C cementite stoichiometry. In the martensitic matrix surrounding the precipitate the carbon content amounts to only 0.48 at.%. Carbon partitioning to the different phases can be quantified in terms of an enrichment factor $\varepsilon = $ (at.% C tempered)/(at.% C as-quenched) to compare the compositions in the phases before and after tempering. The observed values of ε for each state are listed in Table 2. The carbon content in the martensite decreases continuously during tempering, which can be ascribed to carbon partitioning from the supersaturated martensite to the austenite and to carbide formation [39–50].

4. Discussion

4.1. Mechanisms of partitioning and austenite reversion

The microstructure observed by EBSD and TEM allows us to monitor the austenite development at the mesoscopic scale: during the initial high temperature solution annealing in the austenitic regime (1150 °C for 5 min), all carbides were dissolved (Fig. 3c). The high content of solute carbon that is present in the austenite after carbide dissolution decreases the M_s and the M_f temperatures of the austenite

below room temperature. Hence, 8–20 vol.% retained austenite exists after quenching the solution-annealed material to room temperature, Fig. 4. The differences in retained austenite are due to the individual precision of the different characterization methods. EBSD provides a direct method and hence is assumed to give a realistic value within its statistical limits.

After tempering at 400 °C for 30 min the area fraction of austenite increases to $\sim$40%. This change documents that strong austenite reversion takes place even at this low temperature. The local variations in the austenite dispersion after short tempering were larger compared to longer tempering times. We attribute this heterogeneity in the re-austenitization kinetics and topology to the mean diffusion range of the carbon and to the distribution of the carbon sources. Using the data of Speer et al. [40] for the diffusion coefficients in ferrite $D_\alpha = 2 \times 10^{-12}$ m^2 s^{-1} and in austenite $D_\gamma = 5 \times 10^{-17}$ m^2 s^{-1} we obtain a mean free path for carbon of 1.5×10^{-4} m in ferrite and 7.4×10^{-7} m in austenite at 400 °C and 30 min.

This means that austenite reversion starts at decorated defects (e.g. internal interfaces) where the local carbon concentration is high enough and the nucleation energy low enough to promote the formation of this phase. Fig. 7e confirms this assumption. The TEM analysis also suggests that austenite reversion proceeds via a Kurdjumov–Sachs orientation relationship. Shtansky et al. [38] found the same crystallographic relationship during reverse transformation in an Fe–17Cr–0.5C tempered martensite (wt.%).

An important aspect of the pronounced austenite reversion in the current case is that the competing formation of $M_{23}C_6$ carbides is suppressed at 400 °C. This means that more carbon is available to stabilize and promote austenite formation [38,45–47].

We used Thermo-Calc predictions [33,34] to estimate the driving force for austenite reversion for the current alloy and the employed tempering conditions, Fig. 9b. The results reveal that if the carbon concentration in the bulk martensite (α') exceeds 1.21 wt.% (5.45 at.%), austenite (γ) will form at 400 °C, provided that the nucleation barrier is overcome. This result confirms our suggestion made above, namely that no bulk austenitization can occur at this temperature since the average carbon content of the matrix is too low. Instead we assume that only certain lattice defects (interfaces) that experience very high elastic distortions and carbon segregation can provide the nucleation
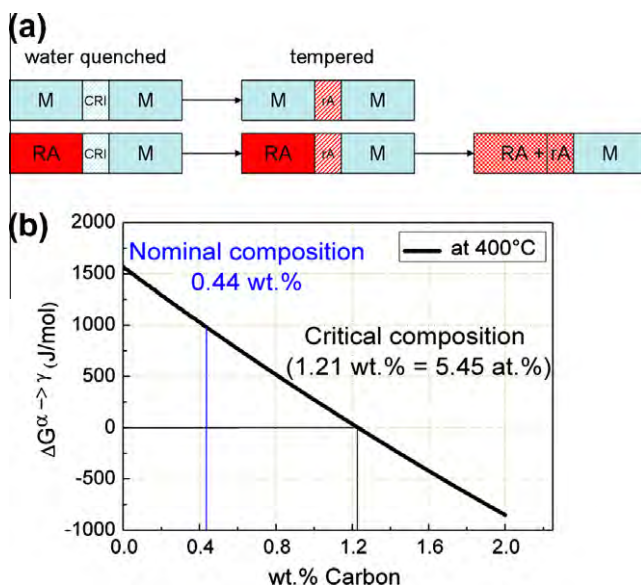
Fig. 9. (a) Schematic illustration of austenite reversion. M: martensite; CRI: carbon-rich interface; RA: retained austenite as obtained after quenching with equilibrium austenite carbon content; rA: reverted austenite formed during 300–500 °C tempering at interfaces owing to the higher local carbon content. After sufficient long diffusion time the carbon content in both types of austenite becomes similar. (b) Calculated driving force for austenite reversion at 400 °C (Thermo-Calc TCFE5).

conditions and a sufficiently high carbon concentration for local austenite formation, Figs. 7e–g and 8. This leads to an increase in the overall austenite fraction. Fig. 6a shows that a 2 min heat treatment at 400 °C leads to an increase in the austenite content from 18.9 to 29.7 vol.%.

Thermo-Calc predictions show that in the current alloy carbon provides the required driving force for this low-temperature austenite reversion. Substitutional atoms, particularly Cr, do not participate in reversion in the current alloy owing to their limited mobility at 400 °C, i.e. the driving force for transformation is here provided exclusively by the high carbon enrichment rather than by substitutional depletion of the austenite, Fig. 8a [39].

Based on these thermodynamic boundary conditions the APT results allow us now to monitor and evaluate the kinetics of carbon at different stages of tempering in more detail (Fig. 8). Fig. 8a shows the as-quenched state: during solution annealing where the material is completely austenitic the elements distribute homogeneously within that phase.

At the onset of water quenching, the majority of the austenite starts to transform into martensite without at first changing its chemical composition. However, as the solubility of carbon in the quenched-in martensite is very small, carbon starts to leave the martensite during and after the $\gamma \rightarrow \alpha'$ transformation and enriches at the γ–α' interfaces, Fig. 8a [45–50]. This process can happen extremely fast: Speer et al. [40,41] showed that carbon partitioning between martensite and austenite in a 0.19C–1.59Mn–1.63Si (wt.%) steel required at 400 °C less than 0.1 s owing to the relatively high diffusion rate of carbon in martensite. In contrast, the further distribution of the newly acquired

carbon within the austenite is nearly three orders of magnitude slower [40–50]. This means that in this case the escape rate of carbon from the newly forming lath martensite is much higher than the carbon equilibration within the austenite [48–50].

In the present quenching process, carbon segregation takes place even faster than in the study quoted above [40,41]. In the current case the carbon has already started to partition and segregate at the martensite–austenite interfaces during the early stages of water quenching immediately after the first martensite has formed [45–50]. The fast kinetics is due to the high mobility of carbon in martensite, Table 3. Such pronounced carbon segregation at the martensite–austenite interfaces is clearly observed in the as-quenched state (Fig. 8a). In the interface area the carbon content reaches up to 4–6 at.% within a narrow layer of ~5 nm. This value is clearly above the nominal composition that purely retained austenite would have [45–50]. Owing to the high escape rate of carbon from the martensite this zone is interpreted as a portion of initially retained austenite which has been enriched in carbon during quenching [45–50].

As explained above this high level of carbon segregation in the present case is a consequence of two effects: the rapid carbon escape from the newly formed martensite, and the low mobility of carbon within the retained austenite. According to Table 3 at 400 °C in 1 min carbon can diffuse 27.000 nm in the martensite and only 130 nm in the austenite [40]. Other sources suggest a 10–20% smaller mean free path of carbon in the martensite [43,44].

Hence, the carbon segregation observed after quenching (Fig. 8a) is due to a partitioning step and a kinetic freezing step (limited mobility of carbon once it arrives in the austenite). From comparing this experimentally observed frozen-in value of 4–6 at.% carbon at the martensite–austenite interface (Fig. 8a) with the value that is predicted by Thermo-Calc as a driving force required for austenite reversion at 400 °C (5.45 at.%), we conclude that austenite reversion will occur under the current conditions at this interface upon heat treatment.

After 1 min tempering at 400 °C, a carbon-enriched austenite layer is observed between two martensite regions (Fig. 8b). In principle this thin austenite layer could originate either from a very thin layer of retained austenite that was enriched with carbon due to partitioning from the

Table 3
Diffusion data for carbon in ferrite and austenite taken from Ref. [40]. For the current heat treatment case of 400 °C (673 K) the diffusion coefficient in ferrite is $D_\alpha = 2 \times 10^{-12}$ m^2 s^{-1} and in austenite $D_\gamma = 5 \times 10^{-17}$ m^2 s^{-1}. The table gives the mean free path for the different tempering stages. The diffusion of carbon on the ferrite can be regarded as a lower bound. The corresponding value for martensite is likely to be higher owing to the high defect density of the martensite.

Time (min)	Austenite (m)	Ferrite (m)
1	1.3×10^{-7}	2.7×10^{-5}
2	1.9×10^{-7}	3.8×10^{-5}
30	7.4×10^{-7}	1.5×10^{-4}

abutting lath martensite or from austenite reversion without any preceding retained austenite. If the carbon-rich zone would be retained austenite the carbon profile in the austenite region would assume a V type distribution. This type of concentration profile would be characterized by a high content at the two martensite–austenite interfaces and a low content in the center of the austenite layer (hence "V"). Also, retained austenite would have the nominal composition, i.e. in the center of the retained austenite zone the carbon content should be 2 at.% or slightly above, as in Fig. 8a. This type of carbon distribution is not observed though. Instead, Fig. 8b shows that the carbon profile assumes a Λ shape within the austenite layer with a maximum carbon concentration above 8 at.%. It is hence plausible to assume that this profile is due to carbon segregation on a former martensite–martensite grain boundary according to the Gibbs adsorption isotherm. This means that during water quenching the carbon that is segregated at the martensite grain boundary has come from both sides. Therefore, the maximum carbon concentration revealed in Fig. 8b, which highly exceeds the equilibrium concentration that it would have been in the austenite, is in the center of the enrichment layer rather than at its rims. This means that during tempering austenite reversion starts in the center of this carbon-enriched area, i.e. at the former martensite–martensite grain boundary. The resulting average carbon concentration in this reverted austenite grain is very high, namely, 6.86 at.% (with a maximum above 8 at.%). The fact that the pronounced Λ shape of the carbon is preserved (frozen in) inside the austenite is due to the low mobility of carbon in austenite, Table 3. These observations suggest that the carbon-rich zone in Fig. 8b is a newly formed austenite layer. If the carbon-enriched area had been located between a martensite and an austenite grain, such as at the positions observed in Fig. 8a and c, the carbon atoms would have arrived only from one side, namely, from the martensite side (Fig. 9). The thickness of the newly formed reverted austenite layer in Fig. 8b is ~15 nm. With increasing tempering time, more reverted austenite is formed (Figs. 4 and 9).

In summary, the behavior of carbon in the current alloy can be described as follows: during quenching, carbon segregates to martensite–martensite grain boundaries (equilibrium segregation) or to martensite-retained austenite interfaces (partitioning plus kinetic freezing). In the first case (equilibrium segregation between two lath martensite zones) during tempering, these carbon-enriched areas in the martensite revert to austenite when the driving force is high enough, owing to the favorable nucleation barrier at the interfaces. In the second case (partitioning at retained austenite) the carbon enrichment leads to austenite growth according to local equilibrium. If the so-reverted austenite is located at or in the vicinity of the austenite–martensite phase boundary, carbon can diffuse from the reverted austenite further into the retained austenite provided that the tempering time is long enough. This carbon enrichment stabilizes the retained austenite. Also, this effect makes it

generally difficult to distinguish reverted austenite from retained austenite (Fig. 9). After 1 min tempering, the reverted austenite has a high carbon content of 6.86 at.% (enrichment factor $\varepsilon = 3.61$). With increasing tempering time, the diffusion of carbon from reverted austenite into retained austenite leads to an increase in the carbon concentration of the retained austenite. After 30 min tempering, the carbon concentration in the retained austenite increases to an average value of 2.42 at.% (Fig. 8c). If the diffusion distance to the nearest phase boundary is too far, e.g. inside the bulk martensite, the high concentration of carbon leads to the formation of carbides inside the martensite.

After 30 min tempering time, the carbon content in the carbides is 25.1 at.%, as measured by APT. This value agrees with the stoichiometric content of carbon in M_3C (25 at.%). Due to the carbon partitioning to austenite, austenite reversion and the competing formation of carbides, the carbon content of the martensite continuously decreases during tempering. The amount of carbon in each phase before and after tempering is listed in Table 2 for the different stages. The other elements, for example chromium, have nearly the same content in both austenite and martensite. This means that during 400 °C tempering, medium range diffusion of carbon can be observed, but the substitutional elements only experience short distance diffusion. For all tempering conditions analyzed above we observe that not the nominal (global) but the local chemical potential of carbon directly at the martensite–austenite and martensite–martensite interfaces and the smaller nucleation energy at the interfaces determine the kinetics of austenite reversion. Similar trends were observed in maraging steels during aging [28,51,52].

In a thought experiment, assuming infinite mobility of the carbon when entering from martensite into austenite, the reversion would proceed more slowly owing to the smaller chemical driving force at the interface when carbon is distributed more homogeneously inside the austenite. In the current situations, however, carbon becomes trapped and highly enriched at the martensite–austenite interface owing to the partitioning and its low mobility within the austenite. This provides a much higher local driving force for austenite reversion. We refer to this mechanism as low temperature partitioning and kinetic freezing effect because the carbon is fast inside the martensite when leaving it but slow (and, hence, frozen) when entering the austenite. A similar effect was recently observed in Fe–Mn steels [28].

4.2. Transformation induced plasticity (TRIP) effect

During tensile testing, the volume fraction of austenite decreases not only in the quenched samples but also in the tempered samples (Fig. 6). When the brittle as-quenched sample failed at an early stage of loading (Fig. 2a, green curve), the amount of retained austenite had decreased from 18.9 to 10.8 vol.%. At failure most of the quenched-in martensite was still in the elastic regime. This means that stress-induced austenite-to-martensite

transformation prevailed since the material took nearly no plastic strain until fracture. After 400 °C austenite-reversion tempering, the ductility of the material improves drastically (Fig. 2). The EBSD results reveal that nearly all of the austenite transformed into martensite during tensile testing, especially in the near-fracture zones (Fig. 6a and b). This observation suggests that strain-induced austenite-to-martensite transformation (rather than stress-induced transformation) prevails in the tempered samples containing reverted nano-sized austenite.

The difference in the displacive deformation behavior between the as-quenched and tempered samples is due to the fact that directly after water quenching, the retained austenite is unstable due to its relatively low carbon content. In the as-quenched state (i.e. without tempering) the carbon content of the retained austenite is equal to the nominal composition after solution treatment. A relatively weak load is, hence, required to transform this retained and rather unstable austenite into martensite at the onset of the tensile test. Transforming a large amount of austenite at the same time, namely, at the beginning of deformation, promotes crack formation and premature failure. In contrast to this as-quenched and rather unstable austenite, subsequent tempering enriches the retained austenite with carbon due to partitioning. The higher carbon content stabilizes the retained and the reverted austenite so that austenite portions with different carbon content undergo the TRIP effect at different stages of deformation. These differences in carbon content of different austenite portions in the same sample are due to the fact that only the local chemical potential of the carbon at the hetero-interfaces determines the partitioning and reversing rates and, hence, also the exact carbon content of the abutting austenite. This means that retained and reverted austenite zones that are carbon-enriched through partitioning have a kinetically determined composition which is subject to local variations in the chemical potential (of carbon). This context explains the more continuous displacive transformation sequence in the tempered material and hence the observed ductility improvement.

Another aspect of the TRIP effect in this material is that austenite reversion, obtained from tempering, does not only stabilize the austenite via a higher carbon content but also increases its overall volume fraction at least after sufficient tempering time. Fig. 6a reveals that the austenite fraction increases from 18.9 vol.% after quenching to 29.7 vol.% after 2 min at 400 °C. Interestingly, after 1 min at 400 °C the austenite fraction did not change much. This means that for the short-annealing case (1 min) the austenite stability and its more sequential transformation as outlined above are more important for the ductilization than its mere volume fraction.

4.3. Precipitation development

The TEM and APT observations confirm that the carbides formed during tempering have are of M_3C type (instead of $M_{23}C_6$). The formation of M_3C is associated with a smaller loss of chromium from the matrix (into carbides) compared to $M_{23}C_6$-type carbides, which can have a high chromium content. Some authors found a sequence of carbide formation in Fe–Cr–C systems during tempering according to $MC \rightarrow M_3C \rightarrow M_7C_3 + M_{23}C_6 + M_6C$ [53]. In our study M_3C carbides prevailed up to 30 min annealing time. Samples taken from the as-quenched state show the highest hardness due to carbon in solid solution. The hardness decrease observed during tempering is related to carbide formation because carbon has a higher strengthening effect in solid solution than in the form of carbides. However, the small carbides (Fig. 8c) also contribute to the strength as observed with TEM (see Fig. 7b). The strain hardening rate decreases with increasing tempering time. This might be due to the coarsening of the carbides and due to the increase in the average carbide spacing (from ∼40 nm after 1 min to ∼80 nm after 30 min tempering at 400 °C). Further, we observe that the yield stress increases during tempering. This might be due to the change in the internal stress state of the martensite matrix. After water quenching, high elastic stresses prevail in the martensite. These lead to early microplastic yielding of the material prior to percolative bulk plastic yielding. During tempering, the internal stress state of the martensite is relaxed due to the escape of carbon. This leads to a delay in the yielding of the tempered samples.

4.4. Relationship between nanostructure and stress–strain behavior

In the preceding sections we presented experimental evidence of grain boundary segregation, hetero-interface partitioning, kinetic freezing, carbide precipitation, retained austenite formation and stabilization, austenite reversion, and the TRIP effect.

In this part we discuss the joint influence of these phenomena on the excellent strength–ductility profile of this steel (Fig. 2a and d).

We differentiate between mechanisms that provide higher strength and those promoting ductility: the most relevant phase responsible for the high strength of the steel after heat treatment is the relaxed martensite. The quenched-in martensite with an extrapolated tensile strength of more than 2300 MPa (approximated from hardness data) is very brittle. Already a very modest heat treatment of 1 min at 400 °C though (Fig. 2a) provides sufficient carbon mobility. This leads to carbon redistribution (carbide formation, grain boundary segregation, dislocation decoration, martensite–austenite interface segregation, austenite solution) and thus to a reduction in the internal stresses of the martensite. The reduced carbon content renders the martensite into a phase that can be plastically deformed without immediate fracture. The second contribution to the increase in strength are the nanoscaled carbides which provide Orowan strengthening, Figs. 7 (TEM) and Fig. 8c (APT). Their average spacing increases
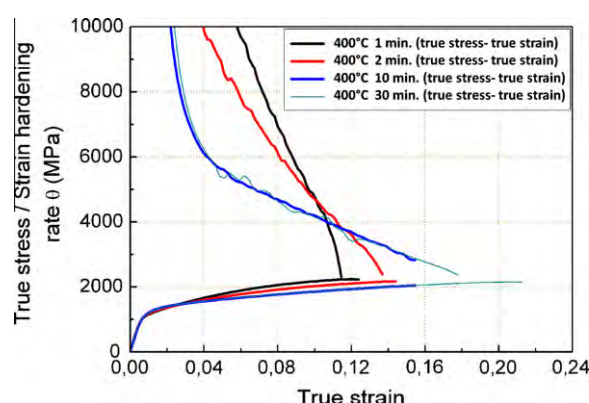
Fig. 10. True stress–true strain curves and corresponding strain hardening curves for the steel after 400 °C heat treatment at different times. The data reveal that the tempering, associated with the increase in the austenite content via austenite reversion, yields higher strain hardening reserves at the later stages of deformation due to the TRIP effect.

from ~50 nm (1 min at 400 °C) to ~80 nm (30 min at 400 °C), Fig. 8b. These two effects, i.e. conventional martensite strength (via high dislocation density, high internal interface density, internal stresses, solid solution strengthening) and Orowan strengthening explain the high strength of the material, but they do not explain its high ductility.

In this context the TRIP effect, i.e. the displacive transformation of retained and reverted austenite, becomes relevant: Fig. 6a reveals a drop in the austenite content from 29.7 to ~2.7 vol.% during deformation for the sample heat treated at 400 °C for 2 min. Fig. 10 shows the true stress–true strain curves and their corresponding derivatives (strain hardening) after 400 °C heat treatment at different times. The data reveal that the tempering, which increases the austenite content via reversion, leads indeed to higher strain hardening reserves at the later stages of deformation due to the TRIP effect, Fig. 6b. Since longer heat treatments lead to higher volume fractions of reverted austenite the TRIP-related strain hardening assumes a higher level for these samples (Fig. 10).

Another important effect that might promote ductility in this context is the wide distribution of the austenite dispersion and stability (carbon content) which are both characteristic for this material. As revealed in Fig. 8 we can differentiate three types of austenite, Fig. 9a. The first type is the as-quenched retained austenite with the nominal carbon content and relatively low stability. The second one is retained austenite, which assumes an increased carbon content due to partitioning during quenching and particularly during heat treatment and has thus higher stability against
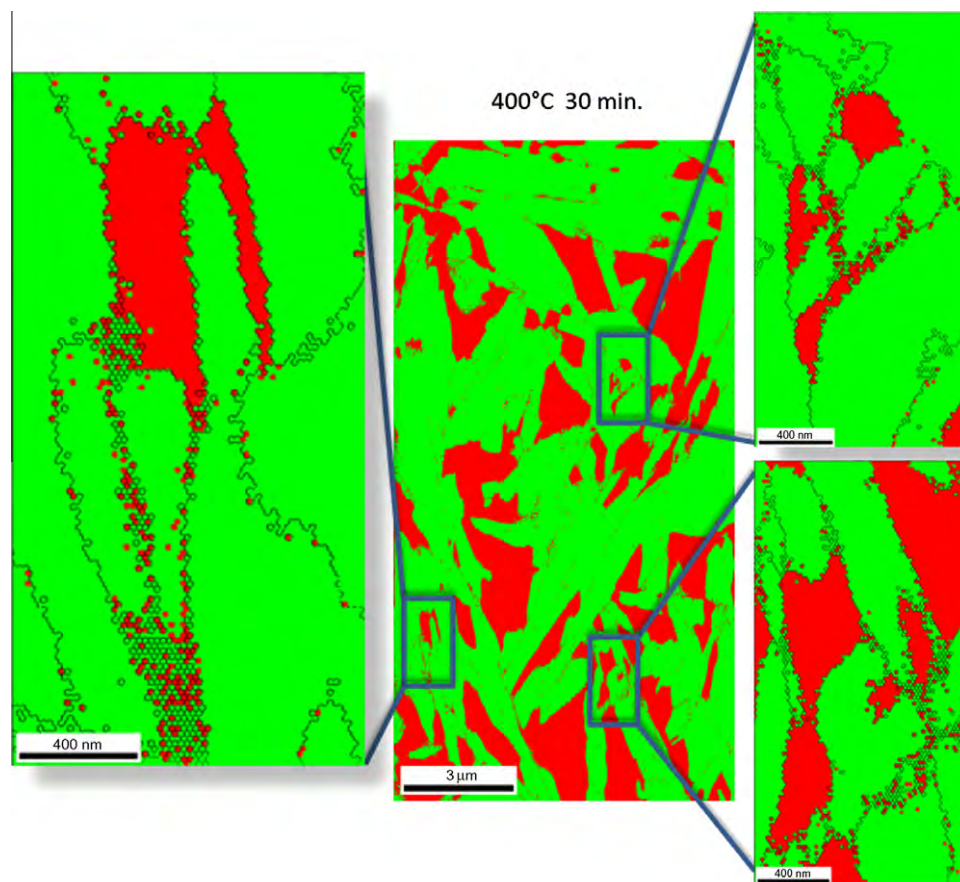

Fig. 11. High-resolution EBSD map (20 nm step size) of the sample tempered at 400 °C for 30 min. The map shows that on some martensite grain boundaries a very thin reverted austenite layer exists. This thin austenite seam can act as a compliance or respectively repair layer against damage percolation entering from the martensite grain. Austenite: red; martensite: green.

displacive transformation. The third type of austenite is the reverted one. These three types of austenite have different carbon concentration, volume fraction and size. Both carbon content and size affect austenite stability. This means that the displacive transformation during tensile testing and the associated accommodation plasticity occur more gradually upon loading compared to a TRIP effect that affects a more homogeneous austenite. We refer to this mechanism as a heterogeneous TRIP effect.

Another important aspect is the composite-like architecture of the reverted austenite, which is located at the martensite–martensite and at the martensite–austenite interfaces in the form of nanoscaled seams (see Figs. 8 and 11). Such a topology might act as a soft barrier against incoming cracks or stress–strain localizations from the martensite. We hence speculate that the austenite seam is a compliance or respectively repair layer that can immobilize defects through its high formability and prevent cracks from percolating from one martensite grain into another (Fig. 11). In this context it is important to note that conventional martensite–martensite interfaces often have a small-angle grain boundary between them which facilitates crack penetration from one lath to another. Here, a compliant austenite seam between the laths might hence be very efficient in stopping cracks.

We emphasize this point since the increase in macroscopic ductility can generally be promoted by both an increase in strain hardening at the later stages of deformation and mechanisms that prevent premature damage initiation.

5. Conclusions

We studied carbon partitioning, retained austenite, austenite stabilization, nanoscale austenite reversion, carbide formation and kinetic freezing of carbon during heat treatment of a martensitic stainless steel Fe–13.6Cr–0.44C (wt.%). The main results are as follows:

1. Austenite formation in carbon-enriched martensite–austenite interface areas is confirmed by XRD, EBSD, TEM and APT. Both the formation of retained austenite and austenite reversion during low-temperature partitioning is discussed. The enrichment of carbon at martensite–martensite grain boundaries and martensite-retained austenite phase boundaries provides the driving force for austenite reversion. The reverted austenite zones have nanoscopic size ($\sim$15–20 nm). The driving forces for austenite reversion are determined by local and not by global chemical equilibrium.
2. Martensite-to-austenite reversion proceeds fast. This applies to both the formation of reversed austenite at retained austenite layers and austenite reversion among martensite laths. The volume fraction of austenite has nearly doubled after 2 min at 400 °C.

3. The carbides formed during tempering have M_3C structure. With increasing tempering time the dispersion of the carbides decreases due to the Gibbs–Thomson effect.
4. During tempering between 300 °C and 500 °C carbon redistributes in three different ways. During quenching, in the vicinity of martensite–austenite interfaces, carbon segregates from the supersaturated martensite to both the hetero-interfaces and homophase grain boundaries. During tempering, carbon continuously partitions to martensite–austenite interfaces, driving the carbon-enriched areas towards austenite reversion (irrespective of whether the nucleation zones were initially retained or reversed austenite). Carbon inside martensite, far away from any interfaces, tends to form M_3C carbides. This means that carbon segregates to martensite grain boundaries, to martensite–austenite interfaces, and forms carbides.
5. We differentiate between three different types of austenite, namely, first, as-quenched retained austenite with nominal carbon content and low stability; second, retained austenite with increased carbon content and higher stability due to partitioning according to the local chemical potential of carbon; and third, reverted austenite.
6. The nanoscale structural changes lead to drastic improvements in the mechanical properties. A sample after 1 min tempering at 400 °C has 2 GPa tensile strength with 14% total elongation. The strength increase is attributed to the high carbon content of the martensite and the interaction between dislocations and nano-sized carbides. The TRIP effect of the austenite during deformation, including the reverted nanoscale austenite, contributes to a strain-hardening capacity and, hence, promotes the ductility. Also, the topology of the reverted austenite is important: we suggest that the nanoscaled seam topology of the austenite surrounding the martensite acts as a soft barrier which has compliance and repair function. This might immobilize defects and prevent cracks from growth and inter-grain percolation.
7. We attribute the fast nanoscale austenite reversion to an effect that we refer to as kinetic freezing of carbon. This means that the carbon is fast inside the martensite when leaving it but slow (and hence frozen) when entering the austenite. This means that carbon becomes trapped and highly enriched at the martensite–austenite interfaces owing to its low mobility within the austenite during low-temperature partitioning. This provides a much higher local driving force for austenite reversion. This means that the formation of nanoscaled reverted austenite depends mainly on the local but not on the global chemical potential of carbon at internal interfaces.

References

[1] Zou D, Han Y, Zhang W, Fang X. J Iron Steel Res Int 2010;17(8):50.

[2] Rodrigues CAD, Lorenzo PLD, Sokolowski A, Barbosa CA, Rollo JMDA. Mater Sci Eng A 2007;460–461:149.

[3] Karlsen M, Grong O, Soefferud M, Hjelen J, Roervik G, Chiron R. Metall Mater Trans 2009;40A:310.

[4] Pieta G, Leite R, Kwietniewski C, Clarke T, Strohaecker T. J Mater Eng Perform 2010;19(9):1318.

[5] Kurdjumov GV. Twelfth Hatfield Memorial Lecture; 1959.

[6] Clarke AJ, Speer JG, Miller MK, Hackenberg RE, Edmonds DV, Matlock DK, et al. Acta Mater 2008;56:16.

[7] Malakondaiah G, Srinivas M, Rao PR. Prog Mater Sci 1997;42:209.

[8] Speer JG, Matlock DK, Cooman BCD, Schroth JG. Acta Mater 2003;51:2611.

[9] Edmonds DV, Hea K, Rizzo FC, Cooman BCD, Matlock DK, Speer JG. Mater Sci Eng A 2006;438–440:25.

[10] Tomimura K, Takaki S, Tanimoto S, Tokunaga Y. ISIJ Int 1991;31:721.

[11] Tomimura K, Takaki S, Tokunaga Y. ISIJ Int 1991;31:1431.

[12] Takaki S, Tomimura K, Ueda S. ISIJ Int 1994;34:522.

[13] Nakada N, Tsuchiyama T, Takaki S, Hashizume S. ISIJ Int 2007;47:1527.

[14] Furuhara T, Kikumoto K, Saito H, Sekine T, Ogawa T, Morito S, et al. ISIJ Int 2008;48:1038.

[15] Nakada N, Tsuchiyama T, Takaki S, Miyano N. ISIJ Int 2011;51:299.

[16] Nayak SS, Anumolu R, Misra RDK, Kim KH, Lee DL. Mater Sci Eng 2008;A498:442.

[17] Cerezo A, Godfrey TJ, Smith GDW. Rev Sci Instrum 1988;59:862.

[18] Blavette D, Deconihout B, Bostel A, Sarrau JM, Bouet M, Menand A. Rev Sci Instrum 1993;64:2911.

[19] Miller MK, Cerezo A, Hetherington MG, Smith GDW. Atom probe field ion microscopy. Oxford: Oxford University Press; 1996.

[20] Thuvander M, Miller MK, Stiller K. Mater Sci Eng 1999;A270:38.

[21] Miller MK. Atom probe tomography analysis at the atomic scale. New York: Kluwer Academic/Plenum; 2000.

[22] Kelly TF, Miller MK. Rev Sci Instrum 2007;78:031101.

[23] Seidman D. Annu Rev Mater Sci 2007;37:127.

[24] Miller MK, Forbes RG. Mater Charact 2009;60:461.

[25] Marquis EA, Miller MK, Blavette D, Ringer SP, Sudbrack CK, Smith GDW. MRS Bull 2009;34:725.

[26] Pereloma EV, Stohr RA, Miller MK, Ringer SP. Metall Mater Trans 2009;40A:3069.

[27] Sauvage X, Lefebvre W, Genevois C, Ohsaki S, Hono K. Scripta Mater 2009;60:1056.

[28] Dmitrieva O, Ponge D, Inden G, Millán J, Choi P, Sietsma J, et al. Acta Mater 2011;59:364.

[29] Gerezo A, Godfrey TJ, Smith GDW. Rev Sci Instrum 1988;59: 862.

[30] Raabe D, Choi PP, Li YJ, Kostka A, Sauvage X, Lecouturier F, et al. MRS Bull 2010;35:982.

[31] Ohsaki S, Raabe D, Hono K. Acta Mater 2009;57:5254.

[32] Choi P, da Silva M, Klement U, Al-Kassab T, Kirchheim R. Acta Mater 2005;53:4473.

[33] Thermo-Calc User's Guide, Version R. Stockholm: Thermo-Calc software AB and foundation of computational thermodynamics; 1995–2006.

[34] Thermodynamic database TCFE5-TCS steels/Fe-alloys database, version 5, Thermo-Calc software. <http://www.Thermocalc.com>.

[35] Sato H, Zaefferer S. Acta Mater 2009;57:1931.

[36] Jiménez JA, Carsí M, Frommeyer G, Knippscher S, Wittig J, Ruano OA. Intermetallics 2005;13:1021.

[37] Rühle M. Metallography and microstructures. In: Transmission electron microscopy. ASM Handbook, vol. 9. Materials Park (OH): ASM International; 1995.

[38] Shtansky DV, Nakai K, Ohmori Y. Acta Mater 2000;48:1679.

[39] Miyamoto G, Usuki H, Li ZD, Furuhara T. Acta Mater 2010;58:4492.

[40] Speer JG, Edmonds DV, Rizzo FC, Matlock DK. Curr Opin Solid State Mater Sci 2004;8:219.

[41] Streicher AM, Speer JG, Matlock DK, De Cooman BC. In: Proceedings of the international conference on advanced high strength sheet steels for automotive applications, vol. 51; 2004.

[42] Zhong N, Wang XD, Wang L, Rong YH. Mater Sci Eng 2009;A506:111.

[43] MCLellan RB, Wasz ML. J Phys Chem Solids 1993;54:583.

[44] Haasen P. Physikalische Metallkunde. Berlin: Springer-Verlag; 1974. p. 173.

[45] Zhu C, Xiong XY, Cerezo A, Hardwicke R, Krauss G, Smith GDW. Ultramicroscopy: IFES 2006, proceedings of the 50th international field emission symposium/19th IVNC 107; 2007. p. 808–12.

[46] Sarikaya M, Thomas G, Steeds JW, Barnard SJ, Smith GDW. Proc solid–solid phase transformations conf. Pittsburgh (PA), Warrendale (PA): The Metallurgical Society of the AIME; 1981.

[47] Barnard SJ, Smith GDW, Sarikaya M, Thomas G. Scripta Metall 1981;15:387.

[48] Bhadeshia HKDH. Met Sci 1983;17:151.

[49] Bhadeshia HKDH. Met Sci 1981;15:175.

[50] Thomas G, Sarikaya M, Smith GDW, Barnard SJ. Advances in the physical metallurgy and applications of steels. London: The Metals Society; 1983. p. 259–65

[51] Höring S, Abou-Ras D, Wanderka N, Leitner H, Clemens H, Banhart J. Steel Res Int 2009;80:84.

[52] Schnitzer R, Radis R, Nöhrer M, Schober M, Hochfellner R, Zinner S, et al. Mater Chem Phys 2010;122:138.

[53] Yan F, Shi H, Fan J, Xu Z. Mater Charact 2008;59:883.